

OFFICE OF CIVILIAN RADIOACTIVE WASTE MANAGEMENT ANALYSIS/MODEL COVER SHEET <i>Complete Only Applicable Items</i>				1. QA: <u>QA</u> Page: <u>1</u> of <u>86</u>									
2. <input type="checkbox"/> Analysis Check all that apply <table border="1" style="width: 100%; border-collapse: collapse; margin-top: 5px;"> <tr> <td style="width: 30%; padding: 5px;">Type of Analysis</td> <td style="padding: 5px;"> <input type="checkbox"/> Engineering <input type="checkbox"/> Performance Assessment <input type="checkbox"/> Scientific </td> </tr> <tr> <td style="padding: 5px;">Intended Use of Analysis</td> <td style="padding: 5px;"> <input type="checkbox"/> Input to Calculation <input type="checkbox"/> Input to another Analysis or Model <input type="checkbox"/> Input to Technical Document <input type="checkbox"/> Input to other Technical Products </td> </tr> <tr> <td colspan="2" style="padding: 5px;">Describe use:</td> </tr> </table>	Type of Analysis	<input type="checkbox"/> Engineering <input type="checkbox"/> Performance Assessment <input type="checkbox"/> Scientific	Intended Use of Analysis	<input type="checkbox"/> Input to Calculation <input type="checkbox"/> Input to another Analysis or Model <input type="checkbox"/> Input to Technical Document <input type="checkbox"/> Input to other Technical Products	Describe use:		3. <input checked="" type="checkbox"/> Model Check all that apply <table border="1" style="width: 100%; border-collapse: collapse; margin-top: 5px;"> <tr> <td style="width: 30%; padding: 5px;">Type of Model</td> <td style="padding: 5px;"> <input checked="" type="checkbox"/> Conceptual Model <input type="checkbox"/> Abstraction Model <input type="checkbox"/> Mathematical Model <input type="checkbox"/> System Model <input type="checkbox"/> Process Model </td> </tr> <tr> <td style="padding: 5px;">Intended Use of Model</td> <td style="padding: 5px;"> <input type="checkbox"/> Input to Calculation <input checked="" type="checkbox"/> Input to another Model or Analysis <input checked="" type="checkbox"/> Input to Technical Document <input type="checkbox"/> Input to other Technical Products </td> </tr> <tr> <td colspan="2" style="padding: 5px;">Describe use: Predict rate of unclipping for fuel rods exposed to a moist/wet environment in a repository</td> </tr> </table>	Type of Model	<input checked="" type="checkbox"/> Conceptual Model <input type="checkbox"/> Abstraction Model <input type="checkbox"/> Mathematical Model <input type="checkbox"/> System Model <input type="checkbox"/> Process Model	Intended Use of Model	<input type="checkbox"/> Input to Calculation <input checked="" type="checkbox"/> Input to another Model or Analysis <input checked="" type="checkbox"/> Input to Technical Document <input type="checkbox"/> Input to other Technical Products	Describe use: Predict rate of unclipping for fuel rods exposed to a moist/wet environment in a repository	
Type of Analysis	<input type="checkbox"/> Engineering <input type="checkbox"/> Performance Assessment <input type="checkbox"/> Scientific												
Intended Use of Analysis	<input type="checkbox"/> Input to Calculation <input type="checkbox"/> Input to another Analysis or Model <input type="checkbox"/> Input to Technical Document <input type="checkbox"/> Input to other Technical Products												
Describe use:													
Type of Model	<input checked="" type="checkbox"/> Conceptual Model <input type="checkbox"/> Abstraction Model <input type="checkbox"/> Mathematical Model <input type="checkbox"/> System Model <input type="checkbox"/> Process Model												
Intended Use of Model	<input type="checkbox"/> Input to Calculation <input checked="" type="checkbox"/> Input to another Model or Analysis <input checked="" type="checkbox"/> Input to Technical Document <input type="checkbox"/> Input to other Technical Products												
Describe use: Predict rate of unclipping for fuel rods exposed to a moist/wet environment in a repository													
4. Title: Clad Degradation-Wet Unzipping													
5. Document Identifier (including Rev. No. and Change No., if applicable): ANL-EBS-MD-000014 REV 00													
6. Total Attachments: 3		7. Attachment Numbers - No. of Pages in Each: I-10 pages, II-9 pages, III-1 CD-ROM											
	Printed Name	Signature	Date										
8. Originator	William O'Connell	<i>William O'Connell</i>	4/13/2000										
9. Checker	Jan Bechtelman	<i>Jan Bechtelman</i>	4/13/2000										
10. Lead/Supervisor	Christine Stockman	<i>Christine Stockman</i>	4/13/2000										
11. Responsible Manager	David Stahl	<i>David Stahl</i>	4/13/00										
12. Remarks:													

**OFFICE OF CIVILIAN RADIOACTIVE WASTE MANAGEMENT
ANALYSIS/MODEL REVISION RECORD**

Complete Only Applicable Items

1. Page: 2 of 86

2. Analysis or Model Title:

Clad Degradation-Wet Unzipping

3. Document Identifier (including Rev. No. and Change No., if applicable):

ANL-EBS-MD-000014 REV 00

4. Revision/Change No.

5. Description of Revision/Change

00

Issued approved.

CONTENTS

	Page
ACRONYMS AND ABBREVIATIONS	8
1. PURPOSE	9
2. QUALITY ASSURANCE	11
3. COMPUTER SOFTWARE AND MODEL USAGE.....	11
4. INPUTS	11
4.1 DATA AND PARAMETERS.....	11
4.1.1 Fuel Rod Properties	13
4.1.2 Irradiated Zircaloy Properties.....	14
4.1.2.1 Young's Modulus for Unirradiated Zircaloy.....	15
4.1.2.2 Data on Young's Modulus for Irradiated Zircaloy.....	16
4.1.2.3 Poisson's Ratio	16
4.1.2.4 Yield Stress for Irradiated Zircaloy	17
4.1.2.5 Yield Stress Correlation	20
4.1.2.6 Data Evaluation for the Yield Stress Correlation	21
4.1.2.7 Uniform and Total Strain	22
4.1.3 Fracture Toughness of Irradiated Zircaloy	22
4.1.4 Breach Sizes Under Anticipated Repository Conditions	22
4.1.5 Spent Fuel Reaction Products.....	23
4.1.5.1 For Humid Air Contact.....	29
4.1.5.2 Contact with Groundwater	29
4.1.5.3 Free Energy of Reaction.....	30
4.1.6 Crystallization Pressures Versus Supersaturation	31
4.1.7 Spent Fuel Alteration Rate	31
4.2 CRITERIA.....	32
4.3 CODES AND STANDARDS	32
5. ASSUMPTIONS	32
6. ANALYSIS/MODEL	37
6.1 REACTION AND DIFFUSION IN A GAP	37
6.2 SPENT FUEL REACTION PRODUCTS.....	38
6.3 WHAT IS THE VOLUME CHANGE ASSOCIATED WITH THE EXPECTED REACTIONS?.....	38
6.4 IS THE AVAILABLE CHEMICAL REACTION FREE ENERGY SUFFICIENT TO CAUSE EXPANSION OF THE ZIRCALOY TUBE?	40
6.5 GIVEN THAT THE AVAILABLE FREE ENERGY IS SUFFICIENT TO CAUSE CLADDING EXPANSION, WILL THIS OCCUR IN THE REPOSITORY?	43
6.6 FUEL MASS REACTED AND TIME UNTIL FILLING OF THE FUEL-CLADDING GAP	46

CONTENTS (Continued)

	Page
6.7 FURTHER REACTION NEAR THE BREACH POTENTIALLY LEADING TO ROD SPLITTING	49
6.7.1 Bounding Model for Unzipping Velocity v_2	52
6.7.2 Alternate Method for Estimating v_2	63
6.7.3 Summary of Unzipping Velocity Model	68
6.7.4 Variations on Some Concepts in the Models	68
6.7.5 Degree of Confidence in the Model	71
6.8 EXPOSED SPENT FUEL AREA AS A FUNCTION OF TIME	72
6.9 MODEL VALIDATION	76
6.9.1 Quantity of Fuel Reacted Before Unzipping Begins and Gap-Filling Time	76
6.9.2 Unzipping Velocity	77
6.9.3 Reacting Spent Fuel Surface Area	78
7. CONCLUSIONS	79
8. INPUTS AND REFERENCES	83
8.1 DOCUMENTS CITED	83
8.2 CODES, STANDARDS, REGULATIONS, AND PROCEDURES	86
8.3 SOURCE DATA	86

FIGURES

	Page
Figure 1. Yield Stress, Average for Irradiated Data	18
Figure 2. Yield Stress Versus Neutron Fluence for $T = 32^{\circ}\text{C}$	18
Figure 3. Yield Stress Versus Temperature	20
Figure 4. Yield Stress Versus Strain Rate for Irradiated and Unirradiated Zircaloy Cladding at $T = 371^{\circ}\text{C}$	24
Figure 5. Yield Stress Versus Strain Rate for Unirradiated Zircaloy Cladding.....	24
Figure 6. Uniform Strain Versus Temperature in Uniaxial Tests for Irradiated Zircaloy Cladding	25
Figure 7. Total Strain Versus Temperature in Uniaxial Tests for Irradiated Zircaloy Cladding	25
Figure 8. Young's Modulus for Unirradiated Zircaloy and Average of a Data Set for Irradiated Zircaloy	26
Figure 9. Data for Fracture Toughness K_{IC} for Irradiated Zircaloy, Both Hydrided and Non-hydrided, Compared to Curves for Unirradiated Zircaloy	27
Figure 10. Backscatter Electron Image for a Polished Cross Section of ATM-103 Spent Fuel after 4.1 Years of a Vapor Exposure Test	28
Figure 11. Backscatter Electron Image Taken at (200 \times magnification) for a Polished Cross Section of the Interface Region of Unirradiated UO_2 Pellets after Eight Years of Reaction in an Unsaturated Drip Test.....	28
Figure 12. Spent Fuel Dissolution Rate in Units of $\mu\text{m}/\text{year}$ at the Pellet or Fragment Surface.....	32
Figure 13. An Extending Breach Driven by Dry Oxidation at Elevated Temperature.....	51
Figure 14. Gap Extension Due to Tube Section Flexure	52
Figure 15. Angular Dependence of the Stress-Squared Quantity near the Crack Tip and in the Elastic Zone, for a Constant Radial Distance r from the Crack Tip, for Plane Strain.....	56
Figure 16. Angular Dependence of the Stress-Squared Quantity near the Crack Tip and in the Elastic Zone, for a Constant Distance r from the Crack Tip, for Plane Stress	57
Figure 17. Angular Dependence, for a Constant Distance r from the Crack Tip and in the Elastic Zone, of the Partial Derivatives of the Displacement Components u_2 and u_3 , for Plane Strain.....	58
Figure 18. Angular Dependence, for a Constant Distance r from the Crack Tip and in the Elastic Zone, of the Partial Derivatives of the Displacement Components u_2 and u_3 , for Plane Stress.....	59
Figure 19. Spent Fuel Rod Showing the Crack Process Zone where the Crack Propagation is Driven by Alteration and Expansion of the Spent Fuel Solid	60
Figure 20. A Close-Up of the Crack Process Zone and the Crack Tip.....	60
Figure 21. Rotational View about the Axial Centerline of a Spent Fuel Rod with a Breach and Circumferential Expansion of the Crack Opening.....	64
Figure 22. Linearized and More Exact Outer Radius of Initial Solid plus Solid Product as a Function of Distance x from the Advancing Crack Tip	70

FIGURES (Continued)

	Page
Figure 23. Ratio of Increases in the Outer Radius as a Function of Distance from the Advancing Crack Tip for the More Exact and the Linearized Models of the Outer Radius.....	71
Figure 24. Location of Active Spent Fuel Reaction Surface as a Function of Unzipping Length, which is a Function of Time.	74

TABLES

	Page
Table 1. Fuel Dimensions for Selected PWR and BWR Fuel Designs	14
Table 2. Mechanical Properties for Unirradiated Zircaloy-2	16
Table 3. Neutron Fluence Values of Measured Spent Fuel Rod Samples.....	19
Table 4. Molar Volumes for Uranium Compounds of Interest for Wet Unzipping	30
Table 5. Standard Gibbs Free Energies of Formation for Uranium Compounds and Reactants of Interest for Wet Unzipping	30
Table 6. Calculated Volume Changes for Reactions 1, 2 and 3 on the Basis of each Mole of UO_2 Reacted under “Limited Water” and “Unlimited Water” Conditions.....	39
Table 7. Estimated Standard Gibbs Free Energy for the Reactions that Form Dehydrated Schoepite, Metaschoepite and Sodium Boltwoodite in the Corrosion of UO_2 Fuel	40
Table 8. Calculated Crystallization Pressures for Dehydrated Schoepite, Metaschoepite and Sodium Boltwoodite for Selected Supersaturation Ratios at 25°C	45
Table 9. The Ratio of Gap Cross-Sectional Area to Fuel Area in Fresh Fuel, for Several Fuel Designs	48
Table 10. The Ratio of Cross-Sectional Area of Fuel Reacted to Total Fuel Area, for Fresh Fuel, for a Gap/Fuel Area Ratio Averaged over Several Fuel Designs, for Several Possible Product Solids of the Fuel Reaction.....	48
Table 11. The Time for Closure of the Gap, Using an Averaged Gap Width in Fresh Fuel as a Bound for the Gap Width in Spent Fuel, for Several Possible Reaction Product Solids and Reaction Rates.....	49
Table 12. Unzipping Velocity as a Function of Solid Product Type and Spent Fuel Alteration Rate	62
Table 13. Unzipping Time Duration as a Function of Solid Product Type and Spent Fuel Alteration Rate	63
Table 14. Unzipping Velocity as a Function of Solid Product Type and Spent Fuel Alteration Rate	67
Table 15. Unzipping Time Duration as a Function of Solid Product Type and Spent Fuel Alteration Rate	67

ACRONYMS AND ABBREVIATIONS

AMR	Analysis and Model Report
ASTM	American Society for Testing and Materials
ATM	approved testing material
BWR	boiling water reactor
DOE	U.S. Department of Energy
DTN	Data Tracking Number
HBR	H. B. Robinson nuclear power plant
LEFM	Linear elastic fracture mechanics
NIST	National Institute of Standards and Technology
OD	outside diameter
PMR	Process Model Report
PWR	pressurized water reactor
QA	quality assurance
SS	stainless steel
TBV	to be verified
WFCR	Waste Form Characteristics Report
WP	waste package
YMP	Yucca Mountain Project

1. PURPOSE

The purpose of this Analysis and Model Report (AMR) is to (1) develop the appropriate modeling concepts and algorithms for the following scope of post-closure process: the rate of breach extension (“unzipping” of a breached spent fuel rod) over the long time frame for cases where the cladding has been breached and water is present and the extent of spent fuel surface exposure or radionuclide release following the unzipping process. A further purpose is (2) to make recommendations for simplified/bounding models suitable for inclusion in the Yucca Mountain Project (YMP) total system performance assessments. Section 7 provides specific recommendations on how various aspects of the model should be used.

The type of modeling within the report scope is the development and support of a conceptual model, which is summarized in verbal description and algebraic equations. The intended use of the model is to be abstracted into a system model, which addresses (1) cladding degradation from multiple modes of degradation, and (2) the consequent exposure of the contained spent-fuel pellets to water-based chemical alteration.

The model applies to unzipping of commercial spent nuclear fuel when the temperature at the spent fuel rod is below 100°C, and water and/or moist air are present, and there is a breach in the fuel rod’s cladding. If these conditions are not present, then the model is not applicable. Restrictions on the range of applicability are necessary because a breach in the cladding is a necessary precondition for water or moist air to contact the spent-fuel pellets, and chemical reactions are quite different in regimes with water versus without water, and in regimes below versus above the boiling point of water. The temperature and water conditions specified will occur at some times in the repository history, as addressed at the beginning of Section 4.1.2.

The model developed in this document is of importance to the post-closure performance of the repository system because the cladding is one of the barriers preventing or limiting the access of water to the radionuclide-containing spent-fuel pellets. A long slow process for the degradation of the cladding will provide a long, low-rate release of long-lived radionuclides, after such time as the outer barriers may have been degraded to the extent of being breached. In so doing, this cladding process will provide a long additional effective containment time for a large mass fraction of these radionuclides.

The levels of appropriateness of the model and of confidence in the model, for the intended use and importance of the model, are the following. The model development examines the principal phenomena involved in the scope of the process and uses directly applicable types of YMP or literature data; hence, by this means the model is appropriate to its intended use. The appropriate level of confidence in the model for its intended use is that (1) there is a scientific basis for the assertion that the bounding model is bounding, and (2) the key parameters of the best-estimate model are given with uncertainty values, and the stated uncertainties either are statistically based on data or there is a scientific rationale that the stated uncertainties are likely to be greater than, or bounds to, the true uncertainties of the parameters.

The model development takes account of the deposition of uranium reaction products in the fuel-cladding gap and in fuel pellet cracks. The model development examines whether filling the gaps slows down or stops the reaction deep inside the breached fuel rod. The model

development further examines interaction of spent fuel alteration/products formation with the cladding's stress and rupture condition, i.e., whether buildup of solid reaction products in and near the breach can cause "unzipping" of the breached cladding. The model development then develops an upper bound on the unzipping rate.

In the long term scenario starting from the occurrence of a breach and the presence of water, the fuel-cladding gap will initially be present and radionuclides released by spent fuel alteration can be transported outward by diffusion in water. The gap will gradually be filled with spent fuel alteration products. Then the release will nearly or completely stop. Hypothetically, the cladding may later be damaged by the expansion of the spent fuel's volume into a volume of solid reaction products, or by further cladding corrosion or external damage. The model described in this document addresses the first time phase, with a gap, very briefly and simply because this period is relatively short. The radionuclide release over this entire period may therefore be represented by a pulse release quantity. The model then addresses the potential for further solid volume increase, the exclusion of the possibility of bulk failure of the cladding tube, the inclusion of the possibility of crack propagation along the cladding, and a bound on the rate of crack propagation by this further fuel reaction.

This document identifies the parameters needed for the model, finds values seen in YMP experiments or other reported experiments, and estimates the mean and uncertainty, or in some cases a range or bound, on the parameters most likely to be important. Some parameters, such as the surface alteration rate of spent fuel, are variable inputs and are the subjects of other YMP calculations, AMRs, or Process Model Reports (PMRs). Some parameters may prove to be unimportant to the present models after sensitivity studies on the models are carried out.

This report was developed in accordance with the *Development Plan for Waste Package Materials Department Analysis and Modeling Reports Supporting the Waste Form PMR* (CRWMS M&O 2000a). It specifically addresses, "Clad Degradation-Wet Unzipping" of the product development plan and is in compliance with procedure AP-3.10Q. Additional guidance is provided by the Lawrence Livermore National Laboratory YMP Activity Plan *Unsaturated Dissolution Tests of Spent Fuel and UO₂* (Stout 1998).

2. QUALITY ASSURANCE

The Quality Assurance (QA) program applies to this analysis. All types of waste packages (WPs) were classified (per QAP-2-3) as Quality Level-1. The model applies to all of the waste package types; reference CRWMS M&O (1999a) *Classification of the MGR Uncanistered Spent Nuclear Fuel Disposal Container System* is cited as an example. The development of this model is conducted under activity evaluation 1101213FM3 *Waste Form Analyses & Models - PMR* (CRWMS M&O 1999b), which was prepared per QAP-2-0. The results of that evaluation were that the activity is subject to the *Quality Assurance Requirements and Description* (DOE 2000) requirements.

3. COMPUTER SOFTWARE AND MODEL USAGE

Microsoft Excel-97 was used with the Microsoft Windows NT v. 4.0 operating system. Excel and Windows NT are commercially available software. No other calculational software is used.

The Excel-97 Workbooks developed are verifiable by inspection and hand calculation. The workbooks constitute a software routine, Wetunzip V 1.0, which is found in Attachment III (in the form of a read-only CD). The routine documents its own inputs, results, equations, and algorithms. Verification of the routine, and the purposes of the various parts of the routine, are discussed in [Attachment II](#). The routine is a set of one-time calculations for the purposes documented in this AMR, and has been verified to give correct results for the input values stated in the spreadsheets. The routine may be expected to give correct results for other physically reasonable inputs:

- As-manufactured dimensions of actual fuel assemblies
- Zircaloy material properties of Young's modulus and strength varying by up to $\pm 50\%$ from the values used
- Zircaloy material property of Poisson's ratio varying by up to $\pm 20\%$ from the values used, remaining < 0.5
- Positive change in volume upon oxidation for UO_2
- Angles about the crack tip of $< 0^\circ$, specifically $-180^\circ < \text{angle} < 0^\circ$. This represents the other side of the crack tip, in a situation of mirror symmetry.

4. INPUTS

4.1 DATA AND PARAMETERS

Below is an outline of the rationale to be presented in Section 6 and the associated parameter types.

Step 1: Show that the fuel-cladding gap and existing cracks fill in with solid reaction products. (The solid logically may be either porous or impervious at this stage of the argument.)

Parameters:

- The secondary solid minerals that are formed (Section 4.1.5)
- Their molar volumes, and the molar volume of UO_2 and other reactants (Section 4.1.5)

Step 2: Estimate the time to fill the fuel-cladding gap.

Parameters:

- Those from Step 1
- Fuel-cladding gap size before irradiation (Section 4.1.1)
- Spent fuel forward alteration rate (Section 4.1.7)

Step 3: Show that the expansion caused by the reaction of the spent fuel matrix and the precipitation of corresponding secondary products will not rupture the intact cladding away from the breach.

Parameters:

- Gibbs free energies of formation of the products from the reactants (Section 4.1.5 and 6.4)
- Young's modulus of irradiated Zircaloy cladding (Section 4.1.2)
- Amount of supersaturation required, versus restraining pressure, for deposition under pressure (Sections 4.1.6 and 6.5)

Step 4: Show that the fuel-cladding gap and any cracks are likely to be sealed by the secondary reaction products.

Parameters:

- Same as for Step 3

Step 5: An existing breach may unzip.

Parameters:

- Same parameters from above steps

Step 6: Evaluate unzipping speed.

Parameters:

- Spent fuel forward alteration rate (see Step 2)
- Young's modulus of irradiated Zircaloy cladding (see Step 3)

- Poisson ratio for Zircaloy cladding (Section 4.1.2)
- Yield stress of irradiated Zircaloy cladding (Section 4.1.2)

Step 7: Spent fuel surface exposed, versus time.

Parameters:

- Distribution of initial crack lengths (Section 4.1.4)
- Inner radius of the cladding (Section 4.1.1)
- Inner radius of the spent fuel pellets (post-irradiation, before aqueous reaction) (Section 4.1.1)
- Length of unzipping at a given time (time integral of the result from Step 6)
- Lengths of rod present on both sides of an initial breach (this is for a stopping rule). (Locations of breaches are outside this model. The full active length of a fuel rod is found in Section 4.1.1.).

The appropriateness of the data to the process and the model is discussed in the following subsections along with the description and development of the data.

4.1.1 Fuel Rod Properties

Fuel rod characteristics as manufactured are taken from the Waste Form Characteristics Report (WFCR) (Stout and Leider 1998, Section 2.1.2.2 and 2.1.2.3). The post-irradiation fuel-cladding gap size and typical breach sizes utilize experimental measurements from Wilson (1985) or Einziger and Strain (1986) (see below).

Fuel cross-sectional dimensions and fueled length are listed in [Table 1](#) (Stout and Leider 1998, Section 2.1.2.2 and 2.1.2.3).

The fuel-cladding gap is the average radial gap or one-half the diametral gap.

During irradiation in a nuclear reactor, the fuel matrix swells due to lattice dislocations, fission products, and activation products, including transuranics. Cracks also develop during irradiation. One spatial result is that the fuel-cladding gap becomes smaller and the surface area open to reaction becomes larger. To account for adequate total void volume and, hence, UO_2 reaction volume needed to fill the void volume, the fuel-cladding gap size before irradiation is used. This volume is sufficient to cover both the remaining gap and the cracks.

Examination of the gap size after irradiation verifies that it has decreased. For later application (Section 6.6) it is only necessary to establish that the gap size is less than or equal to the initial gap size, but not its full distribution. Wilson (1985, 1990) ran batch tests of spent fuel dissolution using bare spent fuel fragments and fuel rod sections with capped ends and machined defects. For the present work, only some fuel sample dimensions are of interest. The fuel-cladding gap is not tabulated, but is shown in photomicrographs. The initial fuel-cladding

diametral gap for Westinghouse 15×15 fuel as manufactured is $0.0095 \text{ cm} = 95 \text{ }\mu\text{m}$ (Table 1, W 15×15 std column, after conversion to radial gap and to cm). In the laser-drilled pinhole samples, the fuel-cladding gap measured by scaling the photomicrographs is $10 \pm 2 \text{ }\mu\text{m}$ (Wilson 1985, p. 22, Figure 4B) and $20 \text{ to } 35 \pm 7 \text{ }\mu\text{m}$ (variable, and with $\pm 7 \text{ }\mu\text{m}$ scaling measurement error) (Wilson 1990, p. 2.6). It is generally to be expected that the final fuel-cladding gap is smaller than the as-manufactured gap, due to fuel swelling and cracking during reactor operation. In the machined slit sample, the fuel-cladding gap is $90 \text{ to } 104 \pm 4 \text{ }\mu\text{m}$ (Wilson 1985, p. 23). The two pinhole samples are from the same rod. The slit sample is from another rod in the same fuel assembly. The $90 \text{ to } 104 \text{ }\mu\text{m}$ value in the slit sample is nearly the same as the as-manufactured gap.

Table 1. Fuel Dimensions for Selected PWR and BWR Fuel Designs

	W 14x14std	W 15x15std	W 17x17std	CE 14x14R	CE 16x16
For reactor type	PWR	PWR	PWR	PWR	PWR
Fueled length (in.)	144	144	144	136.7	150
Rod outside diameter (OD) (in.)	0.422	0.422	0.374	0.44	0.382
Clad thickness (in.)	0.0243	0.0243	0.0225	0.028	0.025
Diametral gap (in.)	0.0075	0.0075	0.0065	0.0075	0.007
Fuel Pellet OD (in.)	0.3659	0.3659	0.3225	0.3765	0.325
WFCR Source Table	2.1.2.2-3	2.1.2.2-3	2.1.2.2-3	2.1.2.2-4	2.1.2.2-4
	BW 15 x 15	BW 17 x 17	GE 7 x 7	GE 8 x 8	Exn 8 x 8-4,5
For reactor type	PWR	PWR	BWR	BWR	BWR
Fueled length (in.)	141.8	143	144	146	144
Rod OD (in.)	0.43	0.379	0.563	0.493	0.5015
Clad thick (in.)	0.0265	0.024	0.032	0.034	0.036
Diametral gap (in.)	0.0084	0.0078	0.012	0.009	0.01
Fuel Pellet OD (in.)	0.3686	0.3232	0.487	0.416	0.4195
WFCR Source Table	2.1.2.2-6	2.1.2.2-6	2.1.2.3-3	2.1.2.3-3	2.1.2.3-3

NOTE: For conservative purposes, a conservative lower-bound value of 3.2 m of rod fueled length is used in Section 6.7
Stout and Leider (1998)

Thus, after irradiation, the fuel-cladding gap is usually much less than, but in all cases examined is less than or equal to, the as-manufactured gap. This conclusion applies to spent fuel, which has not been subject to extensive dry storage near the upper temperature limit for dry storage. In the latter case, cladding creep may reverse some of the gap reduction. It is expected that with such creep the gap size will usually remain less than the as-manufactured gap size.

Breach sizes in perforated cladding are discussed in Section 4.1.4.

4.1.2 Irradiated Zircaloy Properties

The Young's modulus E , Poisson's ratio ν , and yield stress σ_{yield} will be needed directly. The total strain in a tension test will be needed to evaluate the applicability of higher temperature crack propagation data to a lower temperature range.

The temperature range of interest is bounded below by 18°C, the lowest ambient temperature at the repository level under a range of infiltration parameters (DOE 1998, v. 3, p. 3-38, Figure 3-25), and above by 100°C, slightly above the boiling point. Only below the boiling point are aqueous processes applicable. The relative humidity is near 100% for the time period after waste packages might be breached, exposing spent fuel rods to the repository atmosphere and aqueous contact parameters (DOE 1998, v. 3, p. 3-37, Figure 3-23).

It is assumed that the Young's modulus and Poisson's ratio are the same for the Zircaloy-2 and Zircaloy-4 alloys. The Metals Handbook (Webster 1990, p. 666) gives the properties of the two alloys together in the same column. The American Society for Testing and Materials (ASTM) standard B 811-90 (ASTM B811-90 1991, Table 4) for zirconium alloy fuel-cladding tubes gives the yield and ultimate tensile strength minimum requirements together for the two alloys.

It is assumed that the Young's modulus and Poisson's ratio for irradiated Zircaloy-2 and -4 are the same as for the unirradiated alloys. These properties are rarely tabulated for the irradiated alloys; hence, changes in these parameters due to irradiation are apparently not seen as a substantial issue in most papers on irradiated Zircaloy. One set of Young's modulus measurements for irradiated Zircaloy tubing is readily available, and while not exactly equal the results are close to the values for unirradiated Zircaloy (see below for details).

Values are given for the Young's modulus and Poisson's ratio independent of direction in the material. This is an approximation since the fabricated Zircaloy is not isotropic. Standard deviations of the values are given including allowance of variations in the direction of the applied load relative to the material property orientation.

4.1.2.1 Young's Modulus for Unirradiated Zircaloy

Various references report slightly different Young's modulus values for unirradiated Zircaloy at room temperature. The Metals Handbook (Webster 1990, Table 6, p. 666) reports 99.3 GPa for Zircaloy-2 and -4. (Temperature is specified two lines later in the Table for an associated parameter, Poisson's ratio, as being ambient temperature. Temperature is specified for several other parameters earlier in the Table as being 20°C.)

The compilation by ASM International (1967) reports 96.5 GPa for Zircaloy-2 at 70°F (21°C) (ASM International 1967, p. 1).

Glasstone and Sesonske (1981, Table A-6) report several values at different temperatures (see [Table 2](#)). When the data is extrapolated linearly from 27 to 20°C the Young's modulus value is 95.2 GPa. The authors specify that the values are average values for preliminary calculations only and not to be used for design purposes.

Table 2. Mechanical Properties for Unirradiated Zircaloy-2

T (K)	T (°C)	Young's Mod. E (GPa)	Poisson's Ratio
300	27	95	0.43
500	227	90	0.38
600	327	78	(not reported)

NOTE: Glasstone and Sesonske (1981). This data set is the basis for the variation with temperature. Several other data sources are used to establish the mean value at 60°C (see text).

The published E values for unirradiated Zircaloy at 20°C range from 95.2 to 99.3 GPa. These values indicate a distribution with a central value of 97.2 GPa and standard deviation of ± 2.0 GPa. The standard deviation is increased to an upper-bound value of ± 10 GPa to account for an additional data set (Section 4.1.2.2) and possible material anisotropy. The references are authoritative summary sources. The variation with temperature is taken as a linear variation based on the first two lines of Table 2, but in the final recommended distribution the correlation with temperature is not used. This source for the variation parameter is a textbook, Glasstone and Sesonske (1981). Average values are adequate for the variation of Young's modulus with temperature in the present uses and range.

The final recommended distribution uses the value at 60°C (1.0 GPa less than at 20°C). The distribution is therefore 96.2 GPa ± 10 GPa. This distribution is used to include effects of temperature variation within the range 18° to 100°C.

4.1.2.2 Data on Young's Modulus for Irradiated Zircaloy

A set of data on the Young's modulus for irradiated Zircaloy is available in Pettersson et al. (1979, Tables 2, 3) from a series of measurements at a temperature between 290-300°C and at a strain rate of 0.01/hour (0.00017/min). The average value of neutron fluence is 0.5×10^{25} neutrons/m², which is about one-seventh of the value for commercial spent fuel data (Lowry et al. 1981), (see Table 3). The average value is 75.3 GPa, and the standard deviation representing sample-to-sample variation is 10.3 GPa. The standard deviation of the sample average, based on the 40 data points, is 1.6 GPa. This data point is plotted in Figure 8 together with the Young's modulus for unirradiated Zircaloy (Glasstone and Sesonske 1981). An error of ± 10 GPa is assigned to the unirradiated values, primarily due to orientation variability (see discussion of Young's modulus above).

The average-value point for the irradiated samples (Figure 8), 75.3 ± 1.6 GPa, is lower than a linearly interpolated value on the unirradiated Young's modulus curve, which is 86.8 ± 10 GPa at 295°C, but within the uncertainty range. Hence, it is recommended to retain the unirradiated values for use with irradiated Zircaloy.

4.1.2.3 Poisson's Ratio

Various references report different Poisson's ratio values at room temperature.

The Metals Handbook (Webster 1990, Table 6, p. 666) reported 0.37 for Zircaloy-2 and -4. The temperature is specified as being ambient temperature. Temperature is specified for several other parameters earlier in the Table as being 20°C.

ASM International (1967, p. 1) reports 0.31 for Zircaloy-2 at 70°F (21°C).

Glasstone and Sesonske (1981) report values at two temperatures (see Table 2). When the data is extrapolated linearly from 27 to 20°C the Poisson value is 0.43.

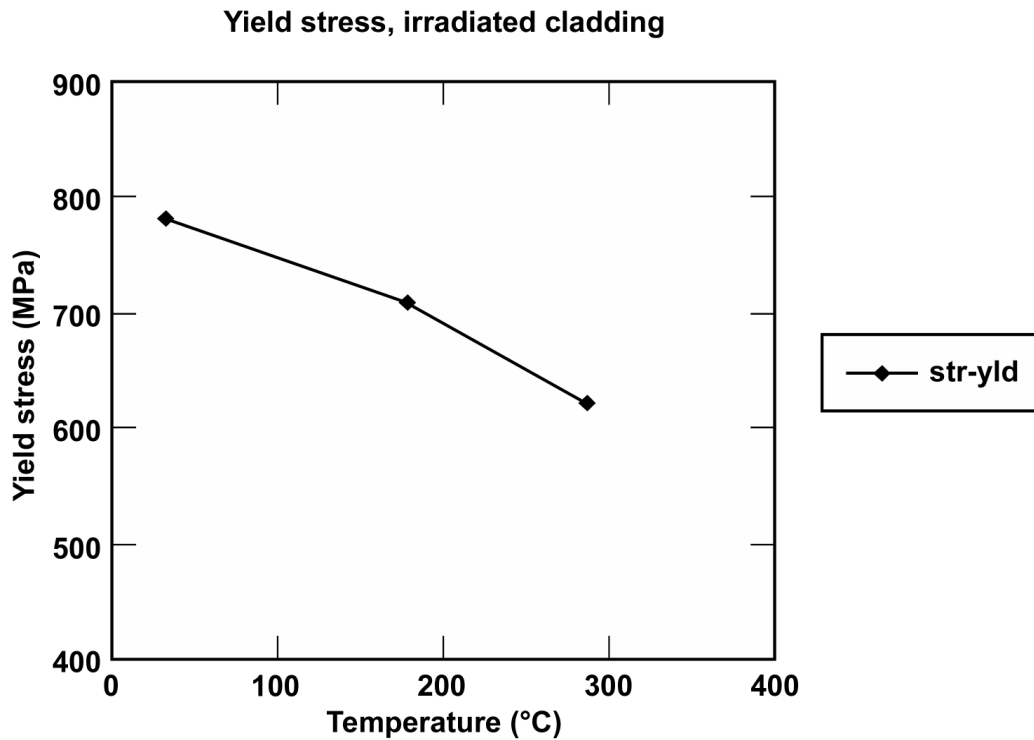
The central value at 20°C is 0.37 ± 0.06 . This range is judged to be enough to account for anisotropy. The sources are authoritative summaries. The variation with temperature is taken as a linear variation based on the data from Table 2, but in the final recommended distribution the correlation with temperature is not used. This source for the variation parameter is a widely used textbook. Average values are adequate for the variation of Poisson's ratio with temperature in the present uses and range.

The final recommended distribution uses the value at 60°C (0.010 less than at 20°C). The distribution, therefore, is 0.36 ± 0.06 . This distribution is sufficient to include effects of temperature variation within the range 18° to 100°C.

4.1.2.4 Yield Stress for Irradiated Zircaloy

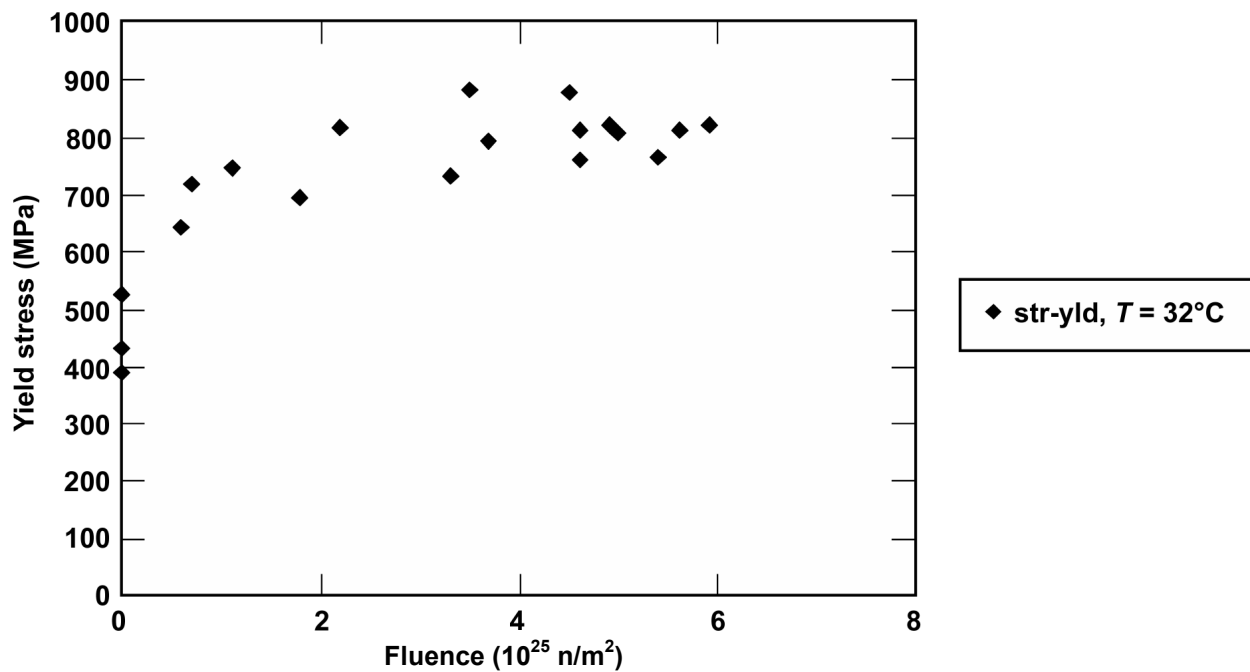
A set of measured stress and strain values was developed by Huang for irradiated Zircaloy-2 (Huang 1995, Table 9-1). The samples were from N-reactor pressure tubes (Huang 1995, p. 155). Since N-reactor and commercial reactors are both thermal reactors, the neutron spectra and therefore the irradiation effects should be similar for a given neutron fluence. The yield stresses whose averages are shown below were measured at a strain rate of 0.005/min; some others were measured at higher strain rates. The 0.2%-yield stress is shown in Figure 1 as a function of temperature; the points are the averages for the data values for neutron fluences above 0.5×10^{25} neutrons/m² for the strain rate of 0.005/min. The 0.2%-yield stress is shown in Figure 2 as a function of neutron fluence at 32°C. For data above a neutron fluence of 2×10^{25} neutrons/m², the yield-stress dependence on fluence is flat, and the variation is the sample-to-sample variation. The yield stress at zero fluence is lower. For intermediate fluences, there seems to be a smooth transition.

The average yield stress value for samples with fluence $> 1 \times 10^{25}$ neutrons/m² is 796 MPa and the standard deviation is 53 MPa. The average yield stress value for samples with fluence $> 0.5 \times 10^{25}$ neutrons/m² (i.e., all the Huang data for irradiated samples) is 782 MPa and the standard deviation is 64 MPa. The fluence values for commercial spent fuel range up to 6×10^{25} neutrons/m² (Lowry et al. 1981, p. 24 and 28). For applications to commercial spent fuel performance assessment, it is recommended that a simple average of the data for all fluences except zero fluence be used, i.e., no dependence on fluence is used except for zero versus non-zero fluence.



NOTE: Huang (1995)

Figure 1. Yield Stress, Average for Irradiated Data



NOTE: Huang (1995)

Figure 2. Yield Stress Versus Neutron Fluence for $T = 32^\circ\text{C}$

A set of measured stress and strain values was developed by Lowry et al. (1981, Tables 16-24) for irradiated Zircaloy-4 from commercial power reactors (Lowry et al. 1981, Tables 16-24). The 0.2%-yield stress is shown in [Figure 3](#) as a function of temperature. The Huang (1995) data are included as well as the Lowry et al. (1981) data at strain rates of 0.05/min and lower. Most data are at a strain rate of 0.025/min.

The neutron fluences for the irradiated data sets of Lowry et al. (1981) (in units of $\times 10^{25}$ neutrons/m²) were measured for several samples. The values from low to high value for each reactor sample series are given in [Table 3](#).

Table 3. Neutron Fluence Values of Measured Spent Fuel Rod Samples

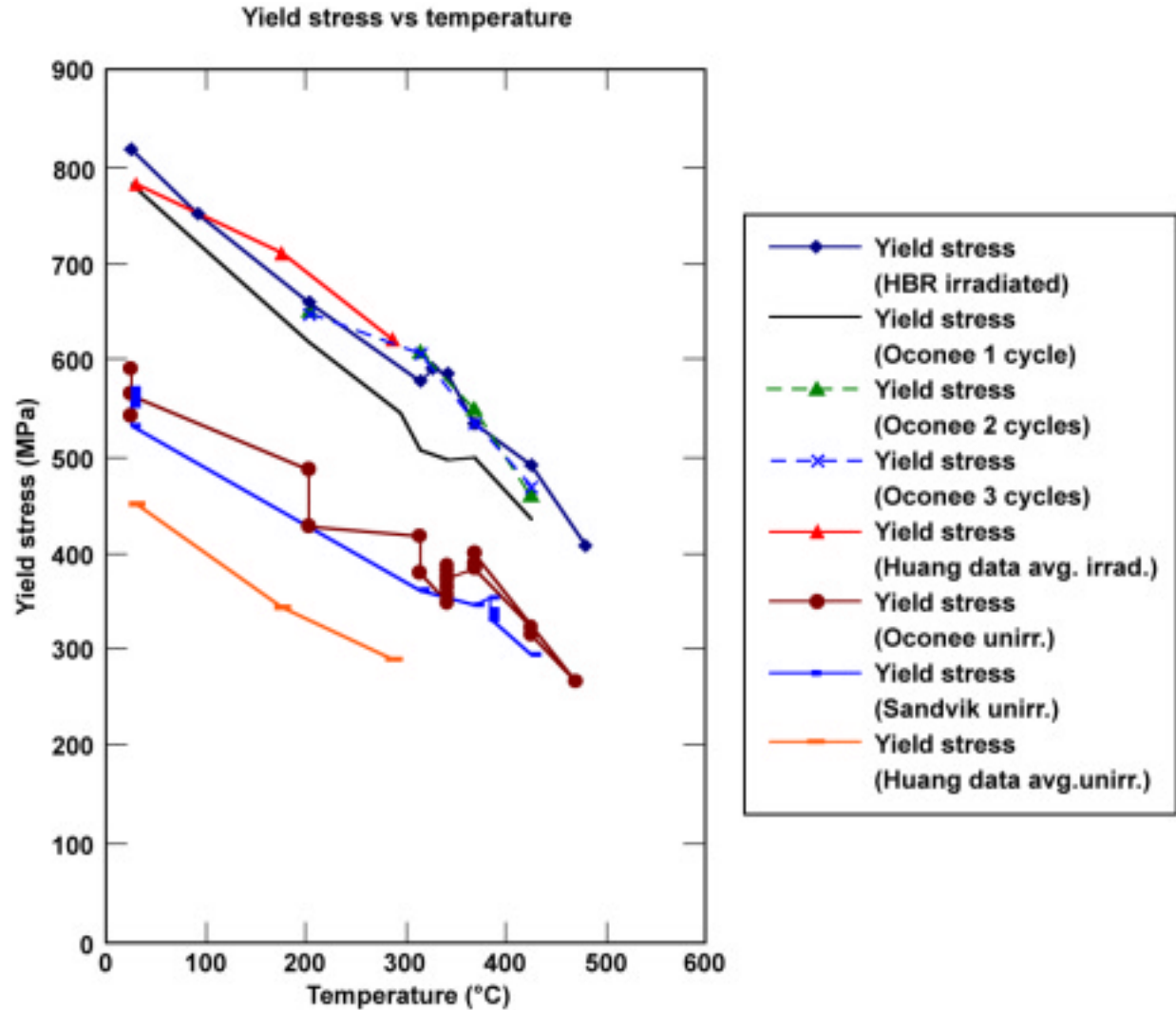
Reactor and Irradiation Period	Burnup (MWd/kgU) ^a	Fluence Values ($\times 10^{25}$ neutrons/m ²) ^b		
H. B. Robinson (HBR)	24.6-30.9	3.8	4.3	4.4
Oconee one-cycle	NA	1.6	1.6	1.8
Oconee two-cycle	NA	3.8	4.0	4.1
Oconee three-cycle	NA	3.9	4.5	5.0

NOTE: ^a Lowry et al. (1981, p. 24)

^b Lowry et al. (1981, p. 28)

The yield stress data curves for the unirradiated Zircaloy-2 (Huang 1995) and Zircaloy-4 (Lowry et al. 1981) cladding are significantly below the values for the irradiated cladding. These curves are for actual materials. The measured yield stresses at 28 or 32°C are well above the minimum specification value of 35 ksi (241 MPa) at room temperature for these alloys (ASTM B 811-90 1991, Table 4).

Lowry et al. (1981) also investigated the dependence of the yield stress on strain rate. The yield stress versus strain rate is shown in [Figure 4](#) for $T = 371^\circ\text{C}$, and in [Figure 5](#) for unirradiated cladding at three temperatures. The dependence is a small positive dependence, although two of the data pairs for unirradiated cladding give indications counter to this trend. For the present analysis of yield stress versus temperature or fluence, data for all strain rate values at 0.025/min and lower are used and data at higher strain rates are omitted.



NOTE: The Huang curves are averages of the data from Huang (1995). The other curves are from Lowry et al. (1981). Data for strain rates of 0.05/min and lower are included.

Figure 3. Yield Stress Versus Temperature

4.1.2.5 Yield Stress Correlation

For a combined-data averaged correlation (see Section 4.1.2.6 for evaluation details) for the temperature range 18–100°C, using data closest to that range (see Figure 3), using a weight of 50% for the Huang (1995) and a weight of 50% for the (Lowry et al. 1981) data, the yield stress σ_{yield} for irradiated Zircaloy fuel rods is given by:

$$\sigma_{\text{yield}} = (767 - 0.72 \times (T - 60)) \pm \sigma, \quad (\text{Eq. 1})$$

where

T is in °C; applicable in the range $18 < T < 100^\circ\text{C}$, σ (standard deviation) is estimated to be 40 MPa to account for uncertainty in the average value, and 75 MPa to account for uncertainty and

sample-to-sample variations. The 40 MPa uncertainty in average value should be used in application to a collection of many fuel rods.

The correlation equation form uses a reference temperature within the range of applicability (in this instance 60°C was chosen). This is used to minimize the apparent effect of the slope term compared to the constant term. A different reference temperature could be used, but would then require a corresponding adjustment in the constant term (here 767 MPa). The ± 29 MPa variation arising from a $\pm 40^\circ\text{C}$ temperature variation about 60°C is smaller than the standard deviation in the average value (40 to 75 MPa).

The correlation equation applies to both Zircaloy-2 and Zircaloy-4 spent fuel rods. There was no significant difference found in the yield stress values for the two data sets for irradiated Zircaloy-2 and Zircaloy-4 respectively, even though there was a moderate but significant difference in the yield stress values for the unirradiated Zircaloy-2 and Zircaloy-4 data sets.

The correlation applies to spent fuel rods, which have had no annealing after irradiation.

4.1.2.6 Data Evaluation for the Yield Stress Correlation

The goal is to find a correlation of yield stress with temperature, applicable within the range $18 < T < 100^\circ\text{C}$. The evaluation is approximate and in part graphical. The 27°C and 100°C points are chosen as evaluation points. There are data points near 27°C. The upper end of 100°C is the maximum needed, and there are data on both sides of 100°C. The resulting correlation equation provides an interpolation for temperature points between 27°C and 100°C and an extrapolation for temperature points between 27°C and 18°C. The data points within or near the range of interest are shown in [Figure 3](#). The evaluation method is a simple one, as follows:

1. Extrapolate the Huang curve from 32°C to 27°C, using a straight-line extrapolation.
2. Interpolate the Huang, HBR, and Oconee one-cycle curves to 100°C.
3. Take averages at 27°C and 100°C, giving 50% weight to the Huang data since it is an average of several measurements, and 25% to each of the data sets from Lowry et al. (1981), since the Huang and Lowry et al. data sets have comparable numbers of data points for irradiated Zircaloy.
4. Use a straight-line interpolation between these two averaged points.
5. The reactor-to-reactor and Zircaloy-2 to -4 variability is taken from the range of the curves at 200°C. The variability at 200°C is larger than at 27°C, but is similar to the variability seen in the range 200-400°C; therefore, that range is selected for use. Assigning a value of ± 1 standard deviation to the range actually seen at 200°C gives a standard deviation of 40 MPa.
6. The correlation equation together with this variability give a distribution, which encompasses the variability of the data set within $27 < T < 100^\circ\text{C}$. No separate estimate of the uncertainty in the slope is needed for this purpose. The slope as found for this correlation equation, when used with the stated uncertainty (see next step), is

intended to be suitable for the range $18 < T < 100^{\circ}\text{C}$ but not for a broader range of temperatures.

7. The sample-to-sample variation within one series of measurements is taken from the Huang irradiated data at 32°C (see above), which is 64 MPa as a standard deviation. The two types of variability, when combined by taking the square root of the sum of the squares, give a total variability with a standard deviation of 75 MPa.

4.1.2.7 Uniform and Total Strain

In Section 6.7, some data on cladding crack growth at 360°C will be applied in the temperature range $30\text{--}100^{\circ}\text{C}$. Hence, it is of interest to examine how the uniform strain and total strain vary with temperature, as an indication of some of the ductility factors that may have an effect on crack shape during crack growth. For the present purpose it is sufficient to establish approximately the factor of change in the strain values between 360 and 30°C .

Figure 6 shows the uniform strain values, and Figure 7 shows the total strain values in uniaxial tensile tests, for irradiated Zircaloy. The uniform strain is roughly constant between 30 and 360°C , and the total strain varies by about a factor of two between 30 and 360°C .

4.1.3 Fracture Toughness of Irradiated Zircaloy

Walker and Kass (1974) measured the fracture toughness K_{IC} of irradiated and unirradiated samples of Zircaloy-4 from rolled and annealed plates. They found that the fracture toughness depends on irradiation, temperature, hydride content and on the orientation of the crack relative to the orientation of the manufacturing processes on the Zircaloy. Figure 9, from Walker and Kass (1974, Figures 3 and 4), shows data for irradiated Zircaloy, in two orientations with relatively lower K_{IC} , compared to curves for unirradiated Zircaloy. The K_{IC} values are lower for hydrided Zircaloy. Since ex-reactor Zircaloy tubing usually has considerable hydride content, it is recommended that the hydrided experimental values be used for application to spent fuel. The K_{IC} values for hydrided irradiated Zircaloy in the range $60\text{--}212^{\circ}\text{F}$ ($18\text{--}100^{\circ}\text{C}$) are roughly a factor of two lower than at the high end of the data range, 600°F (315°C).

4.1.4 Breach Sizes Under Anticipated Repository Conditions

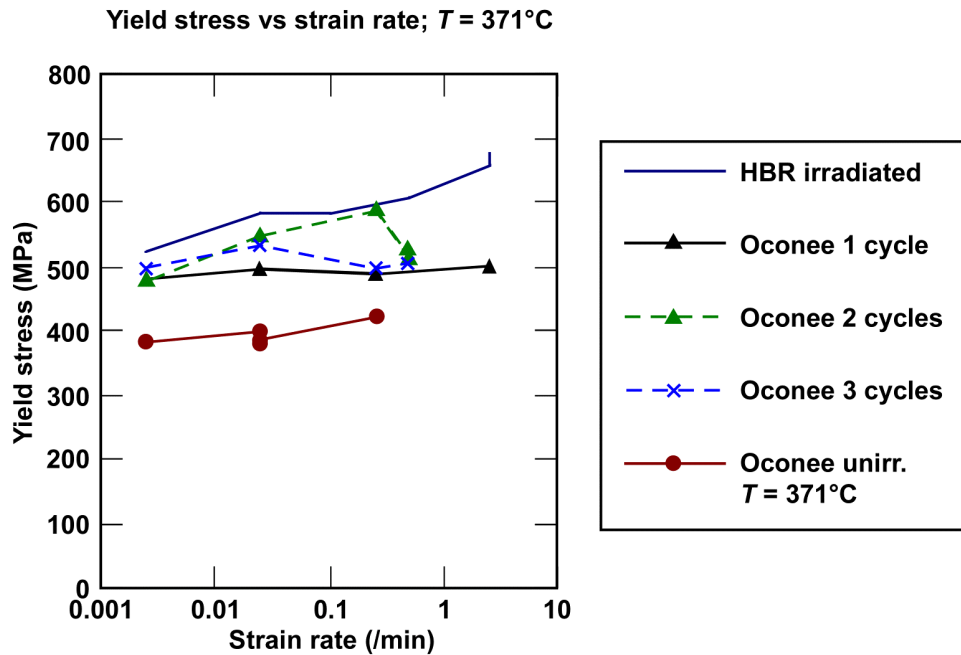
Einzigler and Strain (1986, pp. 83–84) induced breaches in spent fuel rod at 325°C and ~ 15 MPa internal pressure, with stress up to ~ 248 MPa and with iodine added on the internal side to enhance iodine-assisted stress corrosion cracking. Breaches under the internal pressure occurred as early as 1.5 hours and as late as 260 hours. The experimental temperatures are similar and pressure is more severe than will be found in spent fuel storage or disposal containers during the early period when decay heat is greatest. Hence, the experimental breach sizes are suitable for application to potential Yucca Mountain disposal conditions. The breaches ranged from 8 to 52 μm effective circular diameter, as measured by leak rate of air under a known pressure. Einzigler and Strain (1986) determined that the breaches were usually axial cracks with pinhole protuberances through the outer cladding surface, which suggests that the pinhole might be modeled as an ellipse, with a major-to-minor diameter ratio in the range of about 3 to 10. Even with a ratio of 10, the largest value of the major axis is $\sqrt{10} \times 52 \mu\text{m} = 164 \mu\text{m}$ (the area of an

ellipse is πab where a and b are the major and minor radii). This is smaller than the through-wall thickness (clad thickness in Table 1). Hence a larger value, the average clad thickness, will be used as the breach size.

4.1.5 Spent Fuel Reaction Products

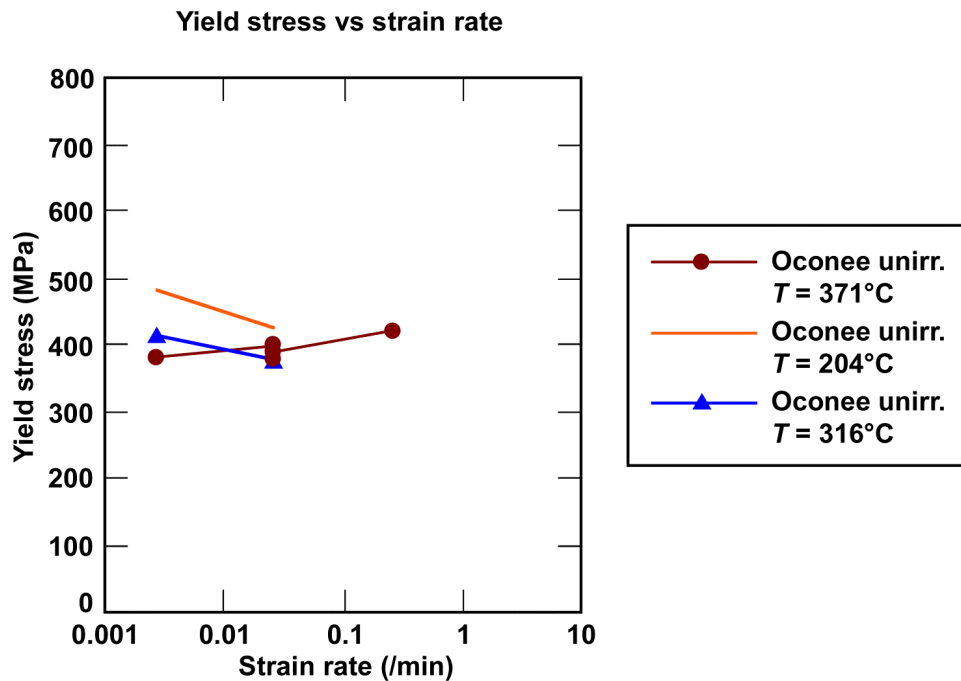
As the spent fuel alters, a layer of reaction products forms on the reacted surface. The present model needs some information on the products formed and their volume. These products are seen in the Argonne National Laboratory unsaturated drip tests. See Stout and Leider (1998), Section 3.4.2.5 for a brief description of the tests, and Tables 3.4.1.3-3 and 3.4.2-4 for identification of the reaction products.

The reaction chemistry is dominated by uranium species and the predominant reaction solid products, as seen in experiments under the relevant conditions, are uranium compounds. Spent fuel is greater than 90% UO_2 , depending on burnup. The remaining 10% is actinides and fission products. Wilson (1985, Table 2) gives the calculated elemental composition of a spent fuel. In Wilson (1985) the 84.8 wt% uranium, plus 11.4 wt% oxygen (total oxygen shown is 11.9%) equals 96.2 wt% UO_2 for a given 27.7 MWd/kgU burnup. Higher burnup leaves less uranium and, hence, less UO_2 with the decrease approximately in proportion to burnup.



NOTE: Lowry et al. (1981)

Figure 4. Yield Stress Versus Strain Rate for Irradiated and Unirradiated Zircaloy Cladding at $T = 371^{\circ}\text{C}$



NOTE: Lowry et al. (1981)

Figure 5. Yield Stress Versus Strain Rate for Unirradiated Zircaloy Cladding

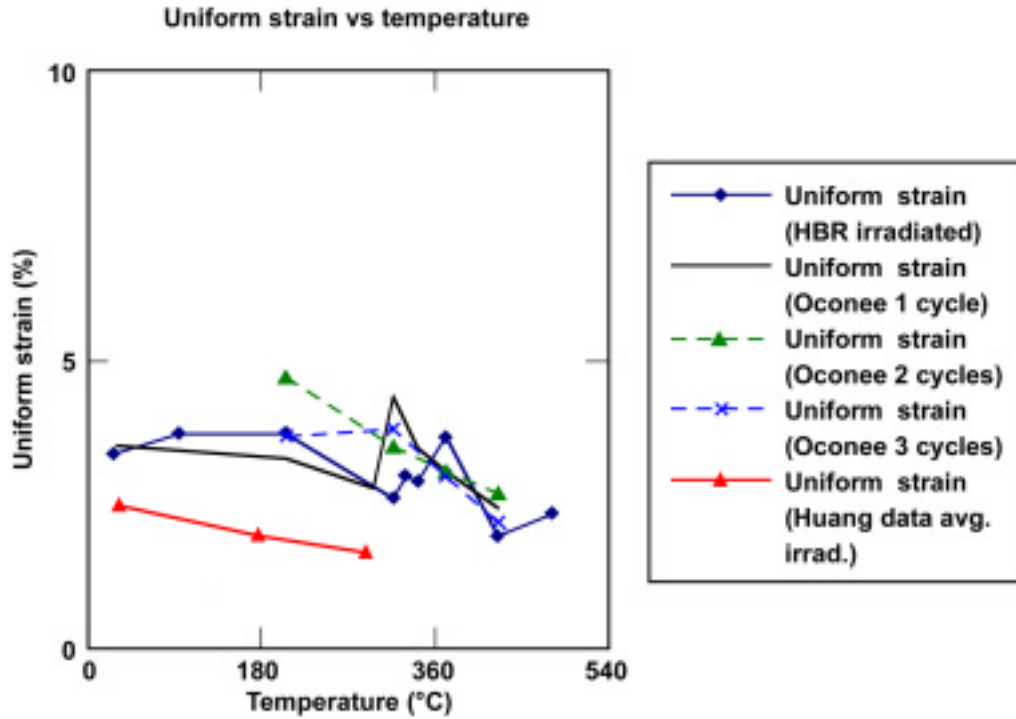


Figure 6. Uniform Strain Versus Temperature in Uniaxial Tests for Irradiated Zircaloy Cladding

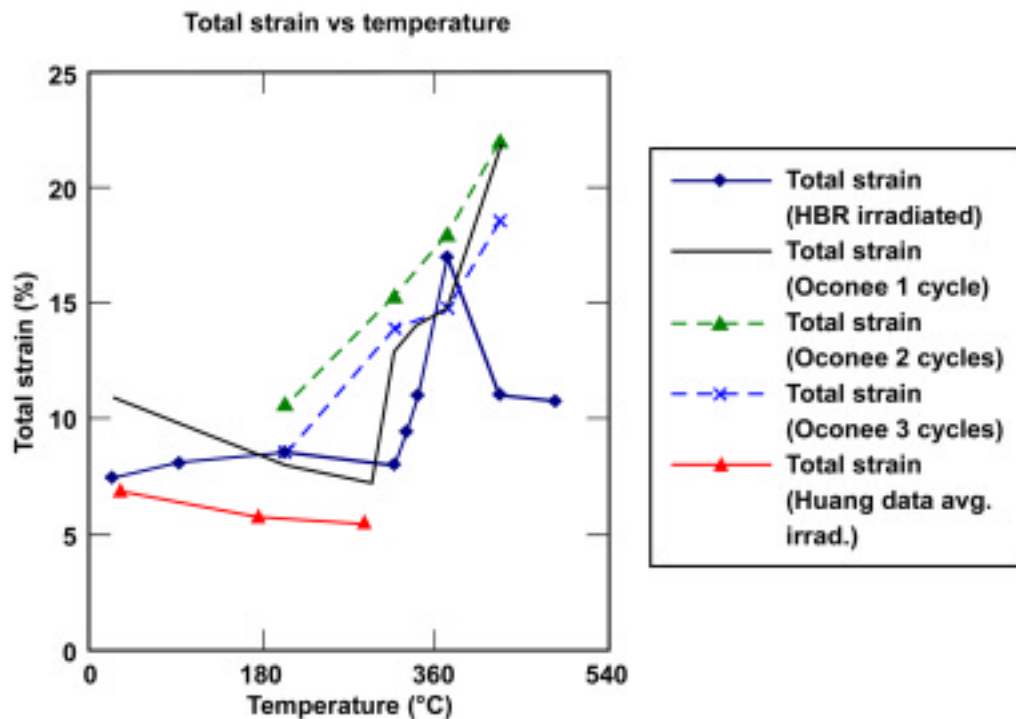
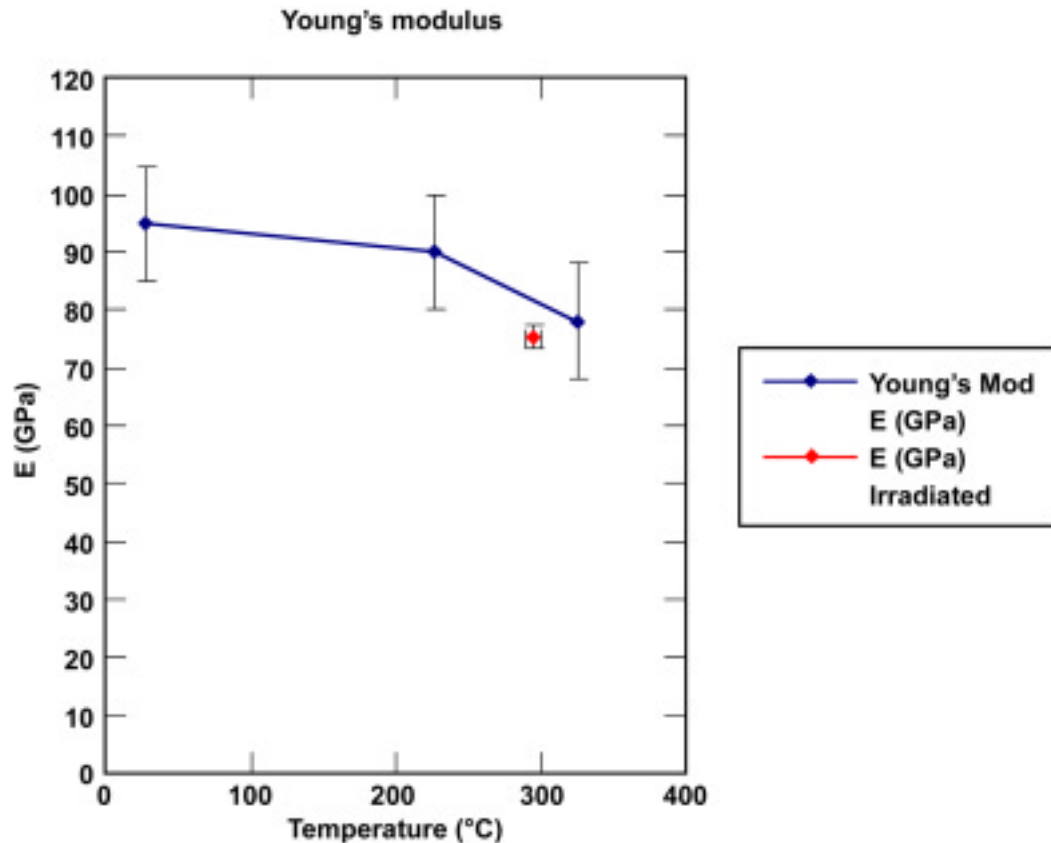


Figure 7. Total Strain Versus Temperature in Uniaxial Tests for Irradiated Zircaloy Cladding

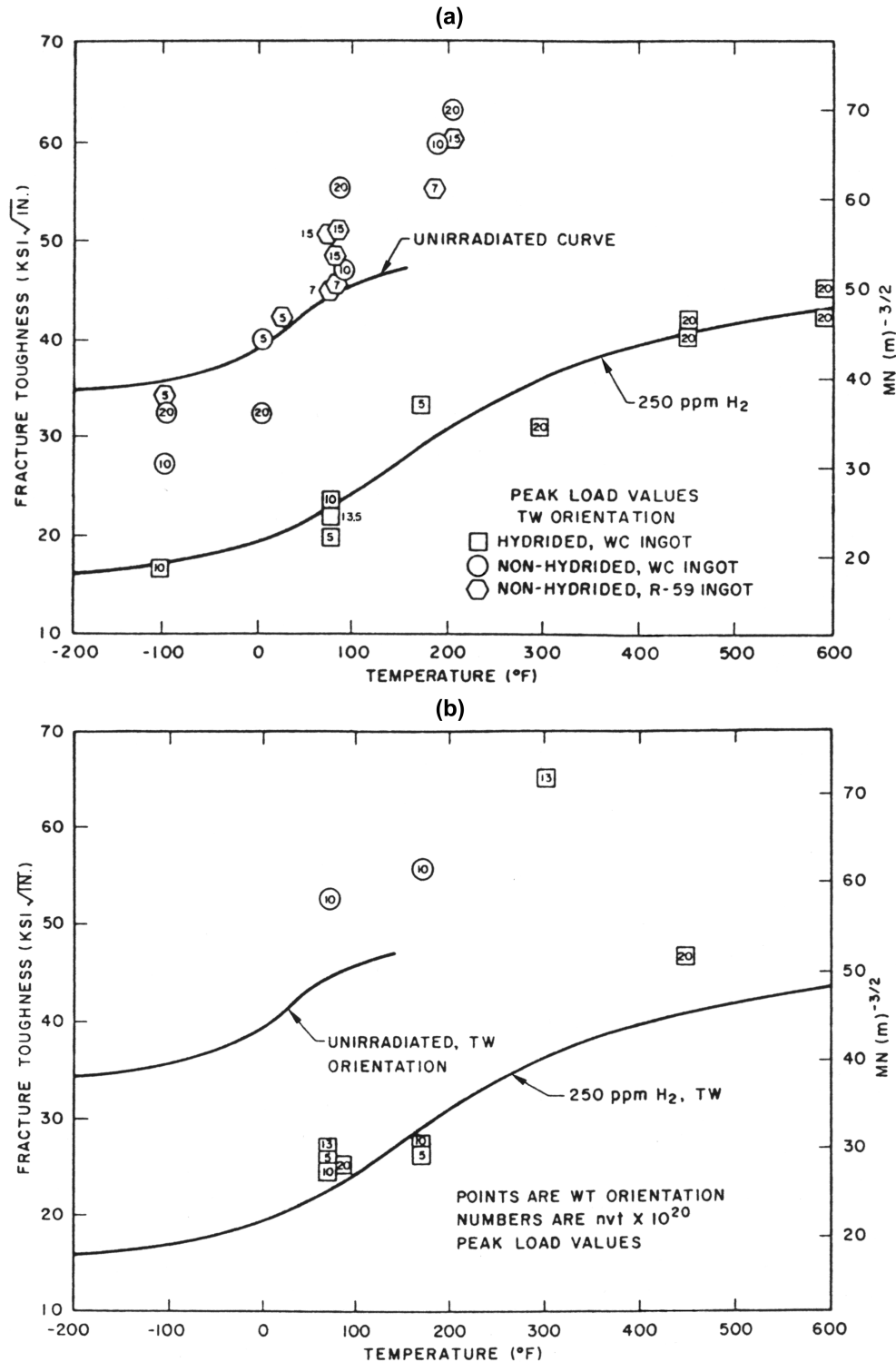


NOTE: The error bars for the unirradiated values include variability in direction relative to the material anisotropy. The smaller error bars for the irradiated values are for the average of a set of measurements in a single orientation.
 Glasstone and Sesonske (1981)
 Pettersson et al. (1979)

Figure 8. Young's Modulus for Unirradiated Zircaloy and Average of a Data Set for Irradiated Zircaloy

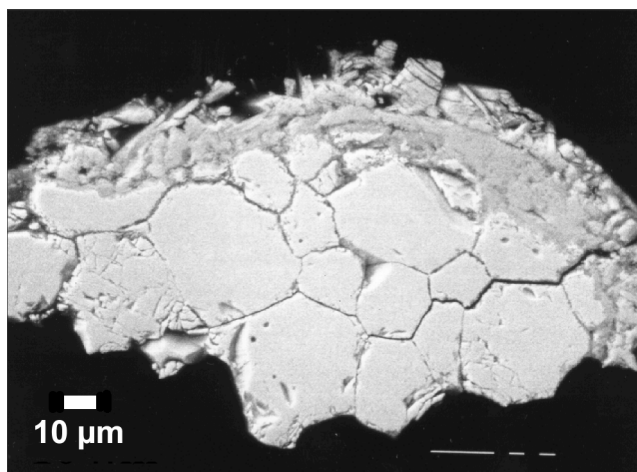
The environment of the spent fuel pellets, after the waste packages and the fuel cladding are eventually breached in the repository, is expected to be humid air and/or groundwater contact, with temperatures below the boiling point of water. See Section 4.1.2 for the full temperature range within the scope of this model. The following data are drawn from experiments to address the fuel alteration reactions if breached rods are exposed to either humid air or groundwater contact.

As the spent fuel alters, a layer of reaction products forms on the reacted surface (Finch et al. 1999, Figures 1a-1d). This is also seen in the Argonne unsaturated drip tests. Figure 10, from Finch et al. (1999, Figure 1d), shows a fuel fragment from a vapor exposure test after four years. The figure shows the typical development of a surface coating of reaction products. The uncoated surface in the figure is an interior zone exposed by breakage during preparation of the sample for imaging. See Stout and Leider (1998, Section 3.4.2.5, Tables 3.4.1.3-3, 3.4.2-4) for identification of reaction products.



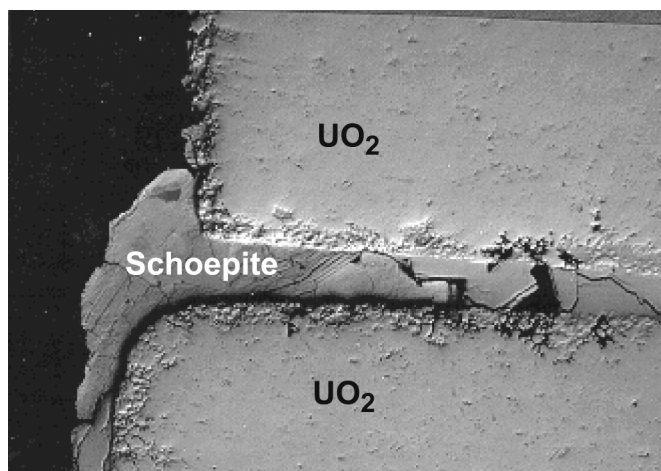
NOTE: (a) Data for the TW orientation; (b) data for the WT orientation of the Zircaloy. In TW and WT, the first letter denotes the normal to the crack plane and the second is the crack propagation direction. T is for thickness and W is for width.

Figure 9. Data for Fracture Toughness K_{IC} for Irradiated Zircaloy, Both Hydrided and Non-hydrided, Compared to Curves for Unirradiated Zircaloy



NOTE: Finch et al. (1999, Figure 1d)

Figure 10. Backscatter Electron Image for a Polished Cross Section of ATM-103 Spent Fuel after 4.1 Years of a Vapor Exposure Test



NOTE: Finch (1997, #PMP8U-2, SN 1171, p. 46, 10/28/96)

Figure 11. Backscatter Electron Image Taken at (200× magnification) for a Polished Cross Section of the Interface Region of Unirradiated UO_2 Pellets after Eight Years of Reaction in an Unsaturated Drip Test

Figure 11, from Finch (1997, p. 46), at lower magnification, shows the configuration of a schoepite alteration phase after eight years, formed between stacked UO_2 pellets in an unsaturated drip test. The intermittent drip flow likely did not cover all the pellet wall surfaces. Water is believed to have been retained in the gap between the pellets. Significant features of the schoepite formed under these conditions are the following: (1) it appears to be a very fine-grained precipitate that has filled the available void space between the pellets, and (2) some of the precipitate seems to have formed as a result of diffusion to, and precipitation at, the outer edge of the pellet–pellet interface. This outer precipitate indicates that the aqueous diffusion of solutes has gone on even when the crack or gap is full or nearly full with precipitates.

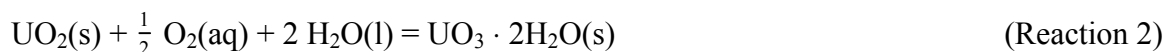
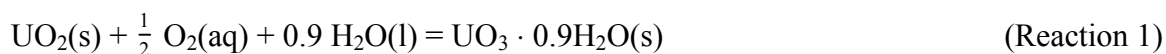
The ongoing experimental tests that address these issues, conducted at Argonne National Laboratory for the YMP, are summarized in [Attachment I](#).

The fuel reactions that may be important for groundwater and/or humid air contact under the temperature and high-humidity conditions identified above are believed to involve oxidative dissolution of the fuel and precipitation of uranyl alteration phases (Shoesmith 1999). The uranyl alteration phases that are formed in experimental tests conducted under the relevant conditions have been identified (Finch et al. 1999). The predominant uranyl alteration products formed upon contact with humid air are dehydrated schoepite (Note: Dehydrated schoepite exhibits a compositional range from $\text{UO}_3 \cdot 0.75\text{H}_2\text{O}$ to $\text{UO}_3 \cdot \text{H}_2\text{O}$ represented by the general formula $(\text{UO}_2)\text{O}_{0.25-x}(\text{OH})_{1.5+2x}$ where $(0 \leq x \leq 0.25)$ (Finch et al. 1998). For ease of reference we will use the formula $\text{UO}_3 \cdot 0.9\text{H}_2\text{O}$) and metaschoepite ($\text{UO}_3 \cdot 2\text{H}_2\text{O}$), whereas sodium boltwoodite $[\text{Na}(\text{UO}_2)(\text{SiO}_3\text{OH})(\text{H}_2\text{O})_{1.5}]$ is the predominant (~80% by volume) phase formed upon contact with groundwater dripping at a high rate (Finch et al. 1999). Although other less abundant phases are observed under the test conditions it is assumed here that the principal effects of alteration phase formation on the cladding can be assessed by considering the effects of the predominant alteration phases.

The overall fuel oxidative dissolution and alteration phase precipitation reactions that are expected under the humid air and groundwater contact conditions outlined above are as follows:

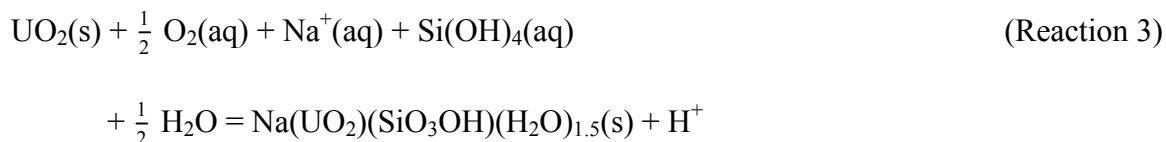
4.1.5.1 For Humid Air Contact

Upon contact with humid air, the fuel is expected to undergo reaction 1 to form dehydrated schoepite and reaction 2 to form metaschoepite (Finch et al. 1999, Sunder and Miller 1996).



4.1.5.2 Contact with Groundwater

Upon contact with groundwater (e.g. J-13 well water) the fuel is expected to also undergo reaction 3 to form sodium boltwoodite (Finch et al. 1999).



These reaction products have greater molar volumes than that of the UO_2 from which they are formed, as shown in [Table 4](#). It is this increase in molar volume of the reaction products formed through oxidative dissolution of the fuel and precipitation of alteration phases that has lead to a hypothesis of possible unzipping of the cladding in breached fuel rods.

Table 4 cites DTN: LL990908751021.088, as do Tables 6, 7, and 8. These data, which are Qualified-Verification Level 2, are not directly used in producing a technical product that provides estimates for any of the principal factors or potentially disruptive events or processes.

For water, the molar volume is 18 cm³/mol.

Table 4. Molar Volumes for Uranium Compounds of Interest for Wet Unzipping

Compound	Molar Volume (cm ³ mol ⁻¹)
Uranium Dioxide	24.6 ^a
Dehydrated Schoepite	44.8 ^b
Metaschoepite	64.5 ^b
Na-boltwoodite	96.6 ^c

DTN: LL990908751021.088

^a Calculated from density in Lide (1995, p. 4-146)

^b Calculated from unit cell volumes in Finch et al. (1992), Cunnane (2000, p. 141)

^c Calculated from unit cell volume in Burns (1998), Cunnane (2000, p. 142)

4.1.5.3 Free Energy of Reaction

The free energy of formation of the reactants and the observed secondary minerals are tabulated in Table 5 and are used in Section 6.4.

Table 5. Standard Gibbs Free Energies of Formation for Uranium Compounds and Reactants of Interest for Wet Unzipping

Compound	$\Delta_f G^\circ$ (kJmol ⁻¹)
Uranium Dioxide	-1031.83 ^a
Dehydrated Schoepite	-1374.56 ^a
Metaschoepite	-1636.5 ^a
Na-boltwoodite	-2844.8 ^b
O ₂	0 ^c
H ⁺	0 ^d
H ₂ O(l)	-237.14 ^e
Na ⁺ (aq)	-261.95 ^f
Si(OH) ₄ (aq)	-1307.73 ^g

^a From Grenthe et al. (1992, Table III.1)

^b From Chen et al. (1999, Appendix I, p 664)

^c From Grenthe et al. (1992, Table IV.1, p 64)

^d From Grenthe et al. (1992, Table IV.1, p 65)

^e From Grenthe et al. (1992, Table IV.1, p 64)

^f From Grenthe et al. (1992, p 78)

^g From Grenthe et al. (1992, p 72)

4.1.6 Crystallization Pressures Versus Supersaturation

The equation for crystallization pressures achievable versus degree of supersaturation is given in Section 6.5. The only new parameter required here is the universal gas constant:

$$R = 8.314510 \pm 0.000070 \text{ J/mol}\cdot\text{K} \text{ (Lide 1995, page 1-3).}$$

4.1.7 Spent Fuel Alteration Rate

The forward rate of spent fuel alteration is given by a model as a function of the controlling environmental chemical parameters (Stout and Leider 1998, Equation 3.4.2.3-2, p. 3-130). The data on which the model is based are listed in (Stout and Leider 1998, Tables 2.1.3.5-4 and 2.1.3.5-4a). This model is being updated in a separate AMR (CRWMS M&O 2000b), based on additional data. This model's result is an input to the present model.

The spent fuel alteration rate is utilized in this report for example calculations. The experimental data for burnups above 25 MWd/kgU from Stout and Leider (1998, Tables 2.1.3.5-4 and 2.1.3.5-4a) are based on an experimental design. The approximately 10th and 90th percentile result values from that data set (see [Figure 12](#)) are used as values for example calculations or sensitivity calculations.

There are 27 data points in the set. Assigning a cumulative frequency value of $i/(n + 1)$ to each point in order of increasing values, from $i = 1$ to $i = n = 27$, the 3rd point has a frequency value of 10.7% and the 25th (3rd from the highest) has a frequency value of 89.3%. Thus, these two data points can serve as approximately 10th and 90th percentile values. This procedure assumes that the input data set is sampled from a population which is representative of the range to be encountered in the repository environment.

The two representative data points are then:

The approximate 10th percentile point equals $0.69 \text{ mg/m}^2\cdot\text{d} = 0.024 \text{ }\mu\text{m/year}$

The approximate 90th percentile point equals $8.6 \text{ mg/m}^2\cdot\text{d} = 0.303 \text{ }\mu\text{m/year}$.

These values are to be used only in scoping or sensitivity calculations; hence, the values and assumptions are not critical to the final model. The dissolution rate values are initially usually expressed in units of $\text{mg/m}^2\cdot\text{d}$. To convert to units of $\text{g/cm}^2\cdot\text{yr}$, multiply by the constant:

$$(1 \times 10^{-3} \text{ g/mg}) \times (365.24 \text{ days/yr}) \times (1 \times 10^{-4} \text{ m}^2/\text{cm}^2)$$

To convert to a rate in units of cm/yr , divide by density of UO_2 in g/cm^3 and then multiply by the fraction of theoretical density. The theoretical density of UO_2 is 10.97 g/cm^3 (Lide 1995, p. 4-146). For sintered pellets, the fraction of theoretical density as manufactured is 95% for most fuels (Stout and Leider 1998, Table 2.1.2.2-2). Thus, the factor is:

$$\div [(10.97/\text{cm}^3) \times 0.95]$$

To convert to a rate S in units of $\mu\text{m/yr}$, multiply by $(\mu\text{m/cm})$:

$$\times (1 \times 10^4) (\mu\text{m}/\text{cm}).$$

Thus, the combined factor is:

$$\times (3.50 \times 10^{-2}) (\mu\text{m}/\text{yr})/(\text{mg}/\text{m}^2 \cdot \text{d}).$$

4.2 CRITERIA

There are no performance criteria for the cladding with respect to whether a breach will get larger over time. For performance on waste isolation, there is no specific subsystem performance requirement for the cladding in this respect.

4.3 CODES AND STANDARDS

There are no Codes or Standards used in the model. The ASTM standard B 811-90 (1991) for zirconium alloy fuel-cladding tubes is referenced in Section 4.1.2 for some information content, but compliance with the standard is not a part of the model.

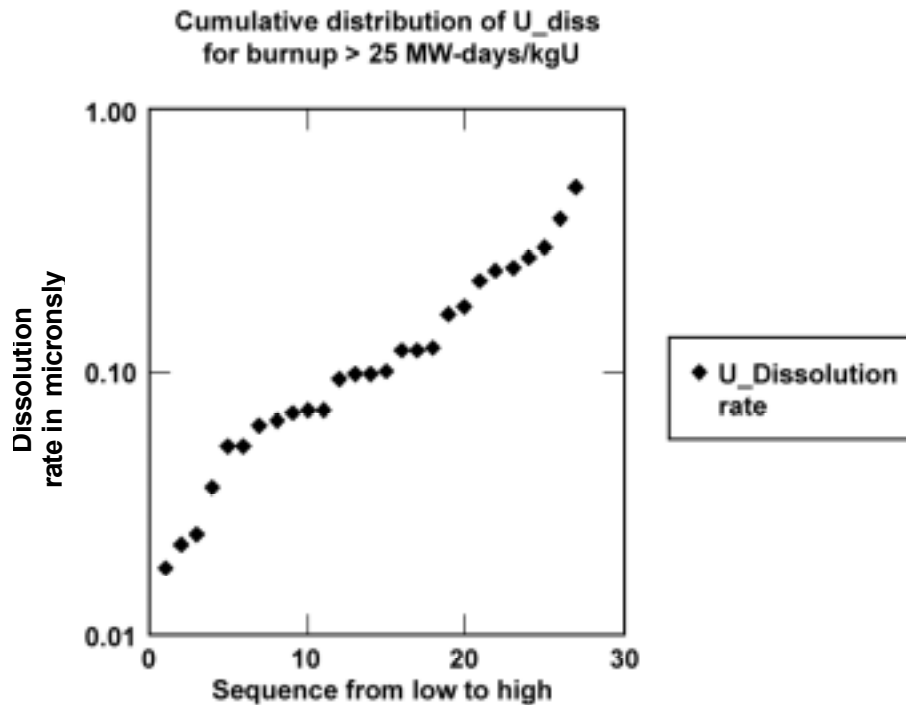


Figure 12. Spent Fuel Dissolution Rate in Units of $\mu\text{m}/\text{year}$ at the Pellet or Fragment Surface

5. ASSUMPTIONS

1. The unzipping velocity from a breach may be treated as dependent only on processes involving that one breach, independent of whether there may be another breach in the same fuel rod. The rationale is that in the early stage of unzipping only a single breach is likely, and at a later stage, after the fuel-cladding gap is filled in with secondary solid products, a breach is hydrologically isolated from any second breach. The likely

mechanisms for a breach involve internal pressure, for example creep or yielding under hydrogen embrittlement and pressure. After one breach, then the internal pressure is relieved. Later, after the fuel-cladding gap is essentially filled in, as analyzed in Section 6.6, then advective flow inside the fuel rod is excluded even if a second breach has developed, so any second breach may be treated in isolation. Hence, this assumption is an acceptable working framework for the model, and does not need verification. This assumption is used throughout.

2. For the total unzipping time, it is assumed that there is only one breach and it is located at the axial center of the rod. This assumption is used only for this one topic, in Section 6.7, to explore whether the unzipping process can extend over long time durations if there is only one breach. The rationale is that this assumption gives a standardized geometry for converting the unzipping velocity to a measure of the time duration involved. The time duration is used only to indicate whether the unzipping process may be of some importance to the repository performance. Note that it is beyond the defined scope of this model and this report to examine other modes of cladding degradation or environmental loading which might cause an additional breach. The principal output of the model is the unzipping velocity from a breach. Because the assumption does not have a bearing on the principal output, it does not require verification.
3. It is assumed that water seeps into all the void spaces of the spent fuel rod, contacting all the spent fuel surfaces. This full contact may actually only partially happen due to limited amounts of water, resistance to wetting some surfaces, or air bubbles inside the small breach and narrow fuel-cladding gap. For the spent fuel reaction rate, the rate in water is used for a water film contact as well. The rationale is that wetting of spent fuel in the narrow flow path of the fuel-cladding gap is not well understood; therefore, it is necessary to use a bounding assumption. This assumption bounds the reaction rate, because the reaction rates in air or under a water film formed from moist-air condensation are generally slower than the rate in groundwater. This assumption is used throughout. Since the assumption is bounding, it does not require verification.
4. It is assumed that the Young's modulus and Poisson's ratio are the same for the Zircaloy-2 as for the Zircaloy-4 alloys, and that the Young's modulus and Poisson's ratio for irradiated Zircaloy-2 and -4 are the same as for the unirradiated alloys. The rationale for these assumptions is presented in Section 4.1.2. In summary, any possible difference has not been a concern in the literature record on the subject, and one data set available for Young's modulus for irradiated Zircaloy confirms that the values are close to those for the unirradiated Zircaloy. The uncertainty in Zircaloy properties is small compared to the total uncertainty in unzipping velocity, presented in Section 6.7.3. Hence this assumption does not require verification. The property values resulting from this assumption are used throughout.
5. If an interior water-filled void in a fuel rod is isolated from the exterior by a filled and sealed gap zone, then it is assumed that the oxygen necessary for the oxidative dissolution of the fuel is provided by water radiolysis. This assumption is used in Sections 6.3 and 6.5. The rationale is that this assumption is logical and feasible: water radiolysis is known experimentally in radiation fields. This assumption is of limited

importance in the model development and of no importance in the final model; hence it does not require verification.

6. For developing appropriate input values of the spent fuel alteration rate for sensitivity studies, it is assumed that the experimental input data set used as a reference data set is sampled from a population which is representative of the range to be encountered in the repository environment. The rationale is that this assumption is reasonable; the data set was established to cover the range expected to be encountered in the repository environment. This assumption is introduced in Section 4.1.7 and is used only in sensitivity studies in Sections 6 and 7 which determine whether a process is of some importance or not. This assumption is not used in the model. Hence this assumption does not need to be verified.
7. It is assumed that the principal effects of uranium alteration phase formation on the cladding can be assessed by considering the effects of the predominant alteration phases. This is described in Section 4.1.5. This assumption is first introduced in Section 4.1.5 and is used throughout. The rationale is that the averages of molar volume changes and Gibbs free energy of formation are dominated by the most abundant species contributing to the averages. A small fractional constituent will make only a small fractional change in the averages. The inequalities established in Sections 6.3-6.5 are not affected by a small change in the numerical values. The results in Sections 6.6-6.8 would only have a small change if the volume increase has a small change; the result change would be small compared to the total uncertainty. Because of this limited sensitivity to a small fractional constituent, this assumption does not need verification.
8. When an incremental volume of spent fuel is altered and a corresponding incremental volume of reaction product is formed by precipitation, it is assumed that the volume expands outward radially and there is neither axial expansion of the volume, nor axial transport of the uranium compounds before precipitation. The rationale is that this assumption is reasonably accurate or conservative, depending on the locations of the masses undergoing alteration. Inside the cladding tube, this assumption is reasonably accurate because other elements of the mass axially constrain the expansion of a mass element. Near the breach, this assumption is conservative because, (a) some expansion or transport in the breach opening direction is conceivable, and (b) an assumption of purely radial expansion gives a higher value for the crack-tip stress and hence for the unzipping velocity. Because of the conservatism, this assumption does not need to be verified. This assumption is used throughout.
9. When the breach's crack tip advances, it is assumed that all of the waste-form outer surface around the circumference under the open crack is exposed to contact with water. The rationale is that much of this circumference may well be exposed to such water contact, as discussed in the early part of Section 6.7; see [Figure 14](#). This assumption is conservative compared to the alternative of only part of the circumference being exposed to water, because the assumption leads to a larger mass undergoing reaction and hence a larger stress on the cladding crack tip and a more rapid crack advance; see Section 6.7.4. Hence this assumption does not require verification. This assumption is used in Sections 6.4, 6.7, 6.8, and 7.

10. In the model for the crack advance, a linearized geometry is assumed based on small reaction depth in the radial direction, in the region of most interest, i.e., near the crack tip. The rationale is that this assumption is accurate to a good approximation for the most frequent cases where the rate of crack advance is much larger than the intrinsic rate of spent fuel dissolution, i.e., about 20 times as large or larger; see Section 6.7.4. As discussed there, the region generating the force at the crack tip is predominantly the region of axial distances within a few times the radius, and there the reaction depth is still small. A variation from this assumption to a more detailed and realistic geometry is shown in Section 6.7.4 to make only a modest change and in a conservative direction, i.e., leading to somewhat slower unzipping velocity. Hence, this assumption does not need to be verified. This assumption is used in Sections 6.7, 6.8, and 7.
11. In estimating the strain energy in the cladding at 2% strain, the simplifying assumption is made that Hooke's law, i.e., a straight-line relation of strain to stress, applies for hoop strains up to 2%. The rationale is that this assumption bounds the actual strain energy: the actual strain versus stress is somewhat curved, falling below this straight line. This assumption is used in Section 6.4. Since the assumption is bounding, it does not require verification.
12. It is assumed that the total void volume inside the spent fuel rod's active length (fueled length), at the start of breach and exposure, remains the same as in fresh fuel. This assumption is used in Section 6.6 to evaluate the amount of fuel matrix that can react before the gaps are filled up. The rationale is that this assumption is bounding because the actual void volume may be somewhat smaller than that in fresh fuel, because of volume expansion of the spent fuel matrix due to fission products and crystal dislocations. Since the assumption is bounding, it does not require verification.
13. The model in Section 6.6 assumes that the end surfaces of the cylindrical fuel pellets do not contribute much additional reaction volume, and that any larger gap widths at the ends due to dishing of the fuel pellets do not contribute proportional to that local gap width. The rationale for the first part of this assumption is that it is an approximation which may affect the results only by a factor considerably less than two, because the end surfaces are smaller than the cylindrical surfaces. The rationale for the second part is that it is reasonable and accurate, because the reaction process stops when the axial fuel-cladding gap and the cracks have become filled and blocked with solid products. The assumption on the whole is an approximation, but it applies to the release quantity during the gap-filling period, and this is a relatively small part of the overall release. Hence the assumption does not require verification.
14. It is assumed that if spent fuel rod unzipping might proceed, then it does proceed. The analysis in Sections 6.2 through 6.5 shows that unzipping is energetically possible, but a mechanism for unzipping to proceed cannot be demonstrated nor ruled out based on the available evidence. The rationale for the assumption of unzipping is that it is the conservative alternative to the other logical possibility, which is that the unzipping process does not start. This assumption is used in Sections 6.7, 6.8, and 7. Since the assumption is conservative, it does not require verification.

15. The initial breach length is assumed to be the same as the cladding wall thickness. The rationale is that this assumption is conservative, the breach size is not used in the model of unzipping rate, and it is unimportant in the secondary result of total time duration of unzipping. This assumed size is larger than a size indicated by measurements of the breaches (see Section 4.1.3), hence, this assumption is conservative. The breach size is small compared to the total length available for breach growth, hence this assumption is relatively unimportant to the unzipping time, and does not need to be verified. This assumption is used in Section 4.1.4 and Section 6.8.
16. The use of the linear elastic fracture mechanics (LEFM) approach in Section 6.7 is based on the assumption that the stress field is within the elastic range except in a small region near the crack tip, and that the inelasticity near the crack tip does not greatly change the elastic stress field from that given by Equation 21. The rationale is that this pair of assumptions is generally acceptable for metals which have crack tip zones with only a small-scale zone of plastic yielding under stress before additional separation of the crack tip (Kanninen and Popelar 1985, pp. 138-139 and 146-147). The more complex approach of elastic-plastic fracture mechanics is only necessary when there is a need to include the influence of significant plastic deformation accompanying crack initiation and stable growth (Kanninen and Popelar 1985, p. 281). The limit of a small plastic zone in a crack-tip geometry is met by metals of only moderate ductility. Zircaloy falls into this category, as indicated by the experimental upper limits of uniform strain being less than 5% strain (see Section 4.1.2). Hence, this assumption does not need to be verified. This assumption is used in Sections 6.7, 6.8, and 7.

6. ANALYSIS/MODEL

When the waste package and the fuel cladding are eventually breached in the repository, the fuel inside the cladding is expected to be exposed to humid air and/or groundwater contact. The conditions of interest for wet unzipping involve fuel temperatures less than $\sim 100^{\circ}\text{C}$ and a relative humidity of $\sim 100\%$ (see Section 4.1.2). Most of the WPs and fuel cladding are expected to remain intact for many thousands of years after emplacement; hence, the below-boiling, high relative humidity conditions are likely to be established before spent fuel rods are exposed to the repository environment. If a fuel rod is in a breached condition, the groundwater may seep into the zone near the breach only, or may seep by wicking or gravity further into the spent fuel rod. In the long-term scenario, the initial fuel-cladding gap will gradually be filled with spent fuel alteration products. The release will then nearly or completely stop. Hypothetically, the cladding may later be damaged by the expansion of the spent fuel's volume into a volume of solid reaction products, or by further cladding corrosion or external damage. Of particular concern is an extension of the initial breach or unzipping, caused by the expansion of the solid volume in the breach region.

Because wet unzipping has not been observed experimentally, its occurrence, and, if it occurs, its rate will be examined by decomposing the process into subprocess alternatives and examining the available technical evidence. An ongoing testing program in the YMP provides some of the current information and will provide further information as the experiments continue ([Attachment I](#)).

Section 6.6 addresses the time duration of the initial period (when a fuel-cladding gap still exists) and the quantity of spent fuel involved in the reaction. Section 6.4 addresses solid reaction-product emplacement, which might isolate the interior of the breached fuel rod from further reaction. Another process can be hypothesized: further growth of the reaction-product solid volume might develop some pressure on the breached cladding, which might promote cladding crack propagation, which would then gradually expose the spent fuel mass once again to reaction. Section 6.7 evaluates a bound on the rate of crack propagation by this hypothesized further fuel dissolution/redeposition/breach-extension process.

6.1 REACTION AND DIFFUSION IN A GAP

When a breach and water contact are established, water can seep into the exposed spent fuel-cladding gap and into spent fuel cracks by wicking, i.e., surface wetting of hydrophilic surfaces. Initially, the transport and release of dissolved radionuclides to the outside of the fuel rod proceeds by diffusion in water. The water-filled fuel-cladding gap provides a pathway for diffusion to the breach. Unclosed cracks in the spent fuel pellets may provide additional pathways to the breach. With only one breach, there is no advection along the interior toward the breach.

The release rates of radionuclides during this period have been measured experimentally (Wilson 1985, 1990). Some radionuclides such as cesium are released at approximately the same rate as from bare spent fuel, while other radionuclides such as uranium and plutonium are released at a

greatly reduced rate compared to bare spent fuel. During this initial period, solid reaction products are forming and the gap is closing gradually. The amount of the spent fuel that reacts before the gap is fully filled depends on the initial gap width and on the relative volumes of the initial spent fuel and the reaction products. The time of this diffusive-release and gap-filling process depends on these parameters and on the spent fuel reaction rate.

The evidence on the reaction products is examined in Sections 6.2 to 6.5 below. An evaluation of the amount of spent fuel that reacts and the time needed to fill the gap is contained in Section 6.6.

6.2 SPENT FUEL REACTION PRODUCTS

The environment of the spent fuel pellets, after the WPs and the fuel cladding are eventually breached in the repository, is expected to be humid air and/or groundwater contact. The following analysis addresses the fuel alteration reactions if breached rods are exposed to either humid air or groundwater contact.

The spent fuel is greater than 90% UO_2 , depending on burnup; the remainder is actinides and fission products (see Section 4.1.5). Hence, the predominant reaction solid products, as seen in experiments under the relevant conditions, are uranium compounds. The principal products are given in Section 4.1.5.

6.3 WHAT IS THE VOLUME CHANGE ASSOCIATED WITH THE EXPECTED REACTIONS?

It is instructive to consider this question for the two situations that bound the range of possibilities for mass transport of the reactants to reaction locations within a fuel rod with breached cladding. The two bounding situations considered here are a “limited water” condition and “an unlimited water” condition.

In a “limited water” condition, the water supply is limited (i.e., the reactions occur in a closed volume to which the water supply can not be replenished). This situation represents a condition that could develop if the reactions were “self-sealing.” An “unlimited water” condition is where the water supply is continuously replenished at the reaction sites within the rod (i.e., no significant mass transport limitations exist for the water-borne reactants). This situation represents a condition in which advective or diffusive transport could supply both the water and solutes at a sufficient rate to the reaction locations that mass transport limitations on the reaction progress are negligible. (Note: Silicon mass transport limitations may be significant for limiting the formation of sodium boltwoodite.)

Table 6 shows the volume change, per mole of UO_2 reacted, in three trials (numbered 1 through 3) for each of the bounding situations defined above. These volume changes were calculated based on the specific volume of the reactants and products (Section 4.1.5). The oxygen for these reactions was assumed to be supplied by radiolysis of the water. The volume change for the “limited water” condition was calculated by subtracting the volume of the reactants consumed (both water and solid) per mole of UO_2 reacted (based on the reaction stoichiometry) from the volume of the products. (Note: the radiolytic hydrogen was assumed to escape and not contribute to the volume of confined reaction products.) In the “limited water” case, solid and

liquid reactants and products are assumed to be confined. In the “unlimited water” case only solids are confined. For the “unlimited water” case the molar volume of the reacting water is not included in the estimated volume of the reactants consumed because it is assumed to be continuously replenished.

Table 6. Calculated Volume Changes for Reactions 1, 2 and 3 on the Basis of each Mole of UO_2 Reacted under “Limited Water” and “Unlimited Water” Conditions.

Reaction	Limited Water ($\text{cm}^3/\text{mol UO}_2$ Reacted)	Unlimited Water ($\text{cm}^3/\text{mol UO}_2$ Reacted)
1	-14.0	20.2
2	-14.1	39.9
3	$\sim -13.2^a$	72.0

DTN: LL990908751021.088

NOTE: From Cunnane (2000), p. 143, modified per Reaction 1

A negative change indicates a volume decrease and a positive change indicates a volume increase.

^a The formation of sodium boltwoodite is limited by the available Si in J-13 well water.

An important observation for estimating the volume change associated with reaction 3 (see Section 4.1.5) is that, in the “water limited” situation the reaction will form only a negligible amount of Na-boltwoodite before the available Si is depleted; the predominant products that will be formed are either dehydrated schoepite or metaschoepite (Note: consideration of the stoichiometry of reaction 3 and the concentration of silicon in J-13 well water shows that the availability of silicon will limit the formation of Na-boltwoodite). The conclusion is that the “limited water” situation will always lead to a volume decrease even though the solid alteration products have a greater specific volume than the starting UO_2 . The “unlimited water” condition, however, will lead to a volume increase for all three reactions.

Hence, in the early phase while water has access through the gap, the reaction products have a larger volume than the initial UO_2 , and the gap fills in. If the gap is water-saturated during this phase, and the oxygen for the reaction comes from hydrolysis, then the net volume change of the water plus UO_2 is slightly negative, and more water is drawn in. If the oxygen enters via diffusion from the breach to the reaction zone, then the volume change may be slightly positive, and some excess water volume is pushed out of the gap zone. In any case, the gap fills in at atmospheric pressure.

Next, the condition of the filled-in gap logically may be porous or sealed. In the interior away from the breach, manufactured indentations in the ends of the fuel pellets (dishing and chamfering) provide a small amount of additional void volume. If the filled-in gap is *sealed*, then reaction products will form a slightly smaller volume than the original water plus UO_2 , causing a slight underpressure. Alternatively, if the filled-in gap is *porous*, then oxygen may diffuse in, and any imbalance of volume is adjusted by water being pulled in or outward as reaction progresses.

For the logical alternative case of a *sealed* gap, the reaction then ceases in the interior. The possible consequences of further reactions in the volume near the open breach are explored in Section 6.7.

For the logical alternative case of a *porous* gap, water and air could then move inward to continue reactions. Uranium solutes logically could either (1) diffuse to the outside, (2) precipitate on favored faces of the product mineral crystals, against a confining load, thus pushing the cladding outward, or (3) precipitate on all faces of the crystals or start of new crystal centers, filling all the remaining porosity and sealing the gap precipitates. The question of whether the chemical free energy of reaction is sufficient to strain the cladding is addressed in Section 6.4, and the question of whether a mechanism exists for utilizing the available chemical energy to do the needed work on the cladding is addressed in Section 6.5. The evidence and arguments presented in Section 6.5 suggest that, in a breached rod in the presence of water, the reactions are likely to be self-sealing.

The question of which of these alternatives is more likely, based on physical mechanisms, is addressed at the end of Section 6.5.

6.4 IS THE AVAILABLE CHEMICAL REACTION FREE ENERGY SUFFICIENT TO CAUSE EXPANSION OF THE ZIRCALOY TUBE?

This section addresses the question of whether the chemical energy is sufficient to cause uniform strain of the Zircaloy cladding away from the breach region, against its strain energy. Section 6.7 addresses the breach region and its crack tip region.

The estimated Gibbs free energy is calculated from the reaction formulas for reactions 1–3 (Section 4.1.5) and the Gibbs free energies of the reactants (Table 5). The results are shown in Table 7.

Table 7. Estimated Standard Gibbs Free Energy for the Reactions that Form Dehydrated Schoepite, Metaschoepite and Sodium Boltwoodite in the Corrosion of UO_2 Fuel

Reaction	ΔG (kJ·mol ⁻¹) ^a
Formation of Dehydrated Schoepite (1)	-129.3
Formation of Metaschoepite (2)	-130.4
Formation of Na-boltwoodite (3)	-124.7

DTN: LL990908751021.088

NOTE: ^a Calculated in Cunnane (2000), pp. 139 and 142

Although these reactions result in expansive alteration phases (Table 6) with some free energy available (Table 7), the overall reaction mechanisms are very different from those of the fuel “dry oxidation” reactions that are experimentally known to cause splitting of the cladding, at least at higher temperatures (see for example Einziger and Strain 1986). An important distinction between the reactions that lead to dry unzipping and those identified above for wet unzipping is that the dry oxidation reactions occur through solid-state diffusion and chemical reaction mechanisms, whereas the postulated wet unzipping would occur through solution-mediated processes of oxidative dissolution and precipitation (McEachern and Taylor 1997, Taylor et al. 1993). The oxidative dissolution reactions 1, 2, and 3 can be considered to proceed through initial formation of a very thin surface oxide layer of $\text{UO}_{2.33}$, which undergoes oxidative dissolution to form dissolved uranyl species, which, in turn, lead to precipitation of the product phases identified above (Shoesmith 1999). The $\text{UO}_{2.33}$ surface layer is negligible from the

perspective of wet unzipping because it has a lower specific volume than UO_2 and because it is formed only as a very thin surface layer. What is important are the reactions that result in aqueous precipitation of metaschoepite, dehydrated schoepite, and Na-boltwoodite.

This question of whether their free energy is sufficient to expand the Zircaloy tube can be addressed by comparing the free energy for the fuel reactions (Table 7) to the work needed to cause cladding expansion. This first step is only to check the energy balance; it does not yet ask whether the energy can be brought to bear in expanding the cladding (see next Section). An energy is expended or transferred to elastic strain when a material is strained over a finite strain by an external force (or stress, stress being a force per unit cross sectional area). As the net volume of the spent fuel and its solid reaction products expands beyond the initial inner radius of the cladding, the cladding must expand and, thus, strain to accommodate the volume change. The cladding expansion takes the form of a hoop expansion, i.e., its dimension around the circumference becomes longer.

For a small increase ΔR from the cladding's initial inner radius R_i , the volume change of the solid, over a length L , is to first order in ΔR

$$\Delta V_s = 2\pi R_i \times \Delta R \times L = 2\pi R_i^2 \times L \times \epsilon \quad (\text{Eq. 2})$$

where

R_i = cladding's initial inner radius

L = length

ϵ = Hoop strain in the cladding

using the geometric approximation that the hoop strain ϵ in the cladding is approximately equal to the relative radial change $\Delta R/R_i$.

The volume reacted in the spent fuel pellet is $(1/D) \Delta V_s$. The reaction energy generated by this volume of reaction is

$$E_{\text{reaction}} = (1/D) \Delta V_s \times E_{\text{molar}}/V_{\text{molarUO}_2} \quad (\text{Eq. 3})$$

where

D = the fractional change in specific volume for the reaction (see Section 6.6)

E_{molar} = the energy per mole

V_{molarUO_2} = the molar volume of the reactant UO_2

D and E_{molar} depend on which reaction product is produced by reaction of groundwater with the UO_2 of the spent fuel.

The circumferential or hoop strain energy expended per unit volume of cladding strained is given by:

$$\frac{W}{V} = \int_0^{\epsilon} \sigma d\epsilon \quad (\text{Eq. 4})$$

where

W = the energy expended for a strained volume V

σ = the hoop stress in the cladding

ϵ = the hoop strain

In a completely elastic strain, the energy expended is stored in the volume, and W/V is called the strain energy density.

In uniaxial testing in the temperature range 20-100°C, uniform strains of 2 to 4% are seen (Figure 6). Thereafter, the specimens exhibit necking, wherein the volume of material involved in nonuniform strain is much smaller. Hence, a uniform strain of 2 to 4% can be used as a measure of the threshold for cladding rupture, and the strain energy in the of 2 to 4% can be used as an approximate measure of the energy required to reach rupture.

For low strains, σ (ϵ) is linear, i.e., Hooke's law applies. For larger strains, ϵ becomes lower than the linear extrapolation of the low-strain line. The assumption that Hooke's law applies for larger strains overestimates the stress and, hence, overestimates the energy density in Equation 4. Using this assumption over the range of interest, up to 4% strain, Equation 4 can be integrated to give:

$$W/V = E\epsilon^2/2 \quad (\text{Eq. 5})$$

where

E = the Young's modulus for irradiated cladding (see Section 4.1.2)

Over a length L of cladding, the cladding volume is approximately:

$$V_{\text{clad}} = 2\pi R_{\text{mid}} \times T \times L \quad (\text{Eq. 6})$$

where

R_{mid} = the radius at the mid-thickness of the cladding, $R_i + 0.5T$

T = the thickness of the cladding

Then the strain energy in this length of cladding, which has been strained to a hoop strain $\epsilon = \Delta R/R_i$ to accommodate an expansion of the contained inner solid from a radius R to $R + \Delta R$, is:

$$E_{\text{strain}} = V_{\text{clad}} \left(\frac{W}{V} \right) \\ = \pi R_{\text{mid}} T L E \epsilon^2 \quad (\text{Eq. 7})$$

To compare E_{reaction} (Equation 3) with E_{strain} (Equation 7) for strain values up to 4%, which is approximately the upper end of the range where the irradiated Zircaloy cladding transitions to nonuniform strain and then rupture, the following ratio of energies is evaluated:

$$\frac{E_{\text{strain}}}{E_{\text{reaction}}} = 0.5 \frac{V_{\text{molar}}(\text{UO}_2) D}{E_{\text{molar}}} \cdot \frac{R_{\text{mid}} T}{R_i^2} \cdot E \epsilon \quad (\text{Eq. 8})$$

Thus, the ratio increases linearly with strain. Parameter values taken from Section 4.1 or derived from those in Section 4.1 are used. R_i and T are taken from Section 4.1.1. E_{molar} is taken from Table 7. $V_{\text{molar}}\text{UO}_2$ is taken from Table 4, Section 4.1.5, and D is calculated from the values in that table. Young's modulus E is taken from Section 4.1.2.

The species-dependent term D/E_{molar} is smallest for dehydrated schoepite and largest for Na-boltwoodite, with a factor of difference 3.7 between them, based on Tables 4 and 7. The largest value, for Na-boltwoodite, is used for conservatism, i.e., for maximizing the ratio of energies. The fuel-type-dependent term $R_{\text{mid}} T/R_i^2$ ranges from 0.136 to 0.182 for the fuels whose dimensions are tabulated in Section 4.1.1. A mid-range design, which for this parameter combination is the B&W 15×15 design, is used. The other values are within $\pm 13\%$ of this value. Then at the largest strain value of 0.04, the value of the ratio of energies is 0.174. That is, the available chemical energy is $1/0.174 = 5.8$ times the needed energy to strain the cladding to rupture. Thus, the energy is large enough and is not the constraint on the further rupture of cladding when the reaction of spent fuel inside is possible.

The next question is whether a mechanism is present to use that energy to expand the precipitated net volume against a confining force.

6.5 GIVEN THAT THE AVAILABLE FREE ENERGY IS SUFFICIENT TO CAUSE CLADDING EXPANSION, WILL THIS OCCUR IN THE REPOSITORY?

This question may be addressed by (1) assessing the empirical evidence for analog systems and by identifying and assessing the processes that may convert the available free energy into the needed work for cladding tube expansion (material hoop strain), and/or (2) by conducting appropriate experimental tests.

The literature has been examined for analogous systems (e.g., formation of expansive phases in cements, formation of expansive phases in the natural weathering of minerals, and the formation of expansive phases in the corrosion of metals, which have caused the denting phenomenon in pressurized water reactor steam generators) in an effort to gain insight into the conditions and

processes that can lead to the conversion of chemical energy into mechanical work. Because the chemical reactions of interest here are aqueous precipitation reactions, the focus of this analysis is on systems in which the mechanisms through which aqueous precipitation (or crystallization) reactions can do mechanical work have been studied. Because of its commercial importance, the precipitation of expansive phases in cements has been studied extensively (Ping and Beaudoin 1992). Specifically pertinent to cladding strain as well as to wet unzipping via a crack tip are studies of the crystallization pressure associated with the precipitation of expansive phases in cement pores.

The fact that crystal growth as a result of aqueous precipitation reactions can exert a crystallization pressure when the crystal growth occurs in a confined volume is well known. The relationship between the crystallization pressure and the extent of supersaturation driving the precipitation reactions has been established for some time (Correns 1949). More recently, thermodynamic principles have been used to derive the following general relationship between the crystallization pressure (P_c) and the extent of solution supersaturation with respect to the precipitating or crystallizing phase (Ping and Beaudoin 1992):

$$P_c = \frac{RT}{V_s} \ln \Omega \quad (\text{Eq. 9})$$

where

V_s = molar volume of the precipitating phase (cm^3/mole)

Ω = “solubility product ratio,” which is defined as K_{sp}/K_{osp} where K_{osp} is the solubility product at one atmosphere and K_{sp} is the solubility product at the crystallization pressure

R = gas constant ($\text{J/mol}\cdot\text{K}$)

T = absolute temperature (K)

Then P_c is in MPa.

Using the molar volume data in Table 4, the gas constant (Section 4.1.6), and a temperature of 25°C, Equation 9 can be used to calculate crystallization pressures as a function of the supersaturation ratios (i.e., solubility product ratios) for dehydrated schoepite, metaschoepite, and sodium boltwoodite; see Table 8. This indicates, conversely, the supersaturation ratios needed to achieve crystallization pressures that are significant from the perspective of driving cladding strain.

Table 8. Calculated Crystallization Pressures for Dehydrated Schoepite, Metaschoepite and Sodium Boltwoodite for Selected Supersaturation Ratios at 25°C

Ω	P_c (MPa) Dehydrated Schoepite	P_c (MPa) Metaschoepite	P_c (MPa) Sodium Boltwoodite
1.05	2.7	1.9	1.3
1.5	22.4	15.6	10.6
2.0	38.3	26.6	17.8
5.0	89.0	61.8	41.3
10.0	127.3	88.5	59.0

DTN: LL990908751021.088

NOTE: From Cunnane (2000), p. 144

The results in Table 8 show that even for very highly supersaturated solutions (e.g., those for which the supersaturation ratio $[\Omega]$ is ten) the crystallization pressures are modest compared to the internal pressures needed to induce a significant (~0.2%) inelastic hoop strain in the cladding. The latter pressure (P) can be estimated as follows:

$$P = \frac{\sigma_1 2t}{d} \cong \frac{2E\varepsilon t}{d} \quad (\text{Eq. 10})$$

where

σ_1 = hoop stress

E = Young's modulus for the cladding

ε = cladding strain

t = cladding wall thickness

d = cladding inner diameter

Use of this expression indicates that an internal pressure of about 115 MPa is needed to produce an 0.2% cladding inelastic strain. This evaluation uses the 0.2% yield stress at 30°C of 789 MPa (Section 4.1.2.5), and a t/d ratio of 0.074, which is the mid-range of the values for the fuel designs tabulated in Section 4.1.1. For all the fuel designs tabulated, the ratio t/d is $0.074 \pm 14\%$. The supersaturation ratios needed to achieve these crystallization pressures appear unlikely to occur within a corroding fuel rod; a supersaturation ratio in excess of 8 is needed to generate crystallization pressures approaching 115 MPa using Equation 9. As pointed out in Correns (1949), the supersaturation at the load-bearing surfaces of a confined crystal would be removed by diffusion to, and crystallization on, the non-load-bearing surfaces of the crystal. The load-bearing surfaces would dissolve and the non-load bearing surfaces would grow until the available void (i.e., water-filled) volume is filled with the precipitating crystals, if the rate of mass transport in the aqueous phase is sufficient to equalize the aqueous concentrations around the growing crystal. Maintenance of significant concentration gradients around a growing crystal would therefore require that the rate of mass transport by diffusion be small compared to

the rate at which the solutes are generated by dissolution. Because the oxidative dissolution reactions of spent fuel are slow it appears unlikely that the solute concentration gradients needed to sustain significant crystallization pressures could develop, at least until the inter-crystal void volumes are filled. Further, a source of new water is needed to keep the expansive reactions going. A source of new water from outside implies that a pathway for uranium solutes to diffuse outward is available, and implies a pressure of zero on the non-load-bearing sides of the crystal.

The arguments outlined above are tantamount to saying that the fuel oxidative dissolution reactions are likely to be self-sealing in a fuel rod with perforated cladding. The statement that there is evidence that the reactions are self-limiting has been made (Shoesmith 1999), but the experimental evidence was not presented. After the void volumes are filled, it is unlikely that the supersaturation ratios needed to generate significant crystallization pressures (i.e., crystallization pressures that could cause one or two percent hoop strain in the cladding) can develop. However, only limited experimental evidence and no quantitative mass transport calculations are available to support this point.

Figure 11 shows the configuration of a schoepite alteration phase formed between stacked UO_2 pellets in an unsaturated drip test. Significant features of the schoepite formed under these conditions are the following: (1) it appears to be a very fine-grained precipitate that has filled the available void space between the pellets; and (2) some of the precipitate seems to have formed as a result of diffusion to, and precipitation at, the outer edge of the pellet–pellet interface indicating that, even under the modest load imposed by the weight of the overlying pellets, the aqueous diffusion of solutes may have minimized the supersaturation that would otherwise have generated crystallization pressures sufficient to lift the overlying pellets. The imputed diffusion through the precipitate indicates that it is still in an early state compared to the fuller precipitation discussed above, which would occur under a confining pressure. The experimental stack of pellets is not under confining pressure.

Ongoing experimental tests that address these issues, conducted at Argonne National Laboratory for the YMP, are summarized in [Attachment I](#).

6.6 FUEL MASS REACTED AND TIME UNTIL FILLING OF THE FUEL-CLADDING GAP

Before the fuel-cladding gap is filled with solid products, the fuel surface can react, soluble radionuclides released from the matrix may be able to diffuse out, and uranium products can gradually fill the gap and other void space. A spent fuel pellet typically has a smaller gap than a fresh fuel pellet (see Section 4.1.1) and also has a network of cracks developed during reactor operation. The cracks as well as the gap can have access for water ingress and radionuclide diffusion out of the breach. The net void volume, including the cracks, is likely to be somewhat smaller after reactor operation than before, because the fuel solid contains diverse fission products and actinides. As a likely conservative approach for the amount of volume available for reaction products during this time phase, it is assumed that the total void volume remains the same as in fresh fuel. The total amount of fuel mass reacted during this phase depends on this void volume and on the change in specific volume for the uranium reaction products compared to the UO_2 . The time duration for this phase depends on the spent fuel reaction rate and on the

gap size and the cracks' opening sizes, but an upper-bound time duration is provided by using the initial gap size for this purpose.

The model assumes that the end surfaces of the cylindrical fuel pellets do not contribute much additional reaction volume, and that any larger gap widths at the ends due to dishing of the fuel pellets do not contribute proportional to its width, because the reaction process stops when the fuel-cladding gap and the cracks have become filled with solid products.

The initial void volume of the gap for fresh fuel varies with fuel design. The ratio of the gap void volume to the fuel volume is the same as the ratio of the cross-sectional areas:

$$Ratio_{Void} = (r_i^2 - r_f^2) / r_f^2 \quad (\text{Eq. 11})$$

where

r_f = the radius of the fuel pellet

r_i = the inner radius of the cladding

When the exposed spent fuel surfaces have a reaction rate S ($\mu\text{m/yr}$), the net solid surface is expanding outward into the available void space at a rate equal to $D \times S$:

$$D = (\text{product volume} - \text{initial volume}) / (\text{initial volume}) \quad (\text{Eq. 12})$$

where

D = the fractional increase in specific volume

Then to fill a void volume V above a surface, a volume $(1/D)V$ of spent fuel matrix below the original surface must be reacted. (As an example, assuming dehydrated schoepite as the product, D is 0.82.)

Then the ratio of the reacted fuel volume to the total fuel volume, to fill the gap void space, is the same as the ratio of the cross-sectional areas of fuel reacted and total fuel:

$$Ratio_{Altered} = (1/D)Ratio_{Void} \quad (\text{Eq. 13})$$

For a set of fuel designs the value of the $Ratio_{Void}$ is given in [Table 9](#); see Section 4.1.1 for fuel design data.

Table 9. The Ratio of Gap Cross-Sectional Area to Fuel Area in Fresh Fuel, for Several Fuel Designs

Fuel Design	Rod OD (in.)	Clad thickness (in.)	Diametral gap (in.)	Fuel OD (in.)	GapArea/FuelArea
W 14x14std	0.422	0.0243	0.0075	0.3659	0.041
W 15x15std	0.422	0.0243	0.0075	0.3659	0.041
W 17x17std	0.374	0.0225	0.0065	0.3225	0.041
CE 14x14R	0.44	0.028	0.0075	0.3765	0.040
CE 16x16	0.382	0.025	0.007	0.325	0.044
BW 15x15	0.43	0.0265	0.0084	0.3686	0.046
BW 17x17	0.379	0.024	0.0078	0.3232	0.049
GE 7x7	0.563	0.032	0.012	0.487	0.050
GE 8x8	0.493	0.034	0.009	0.416	0.044
Exn 8x8-4,5	0.5015	0.036	0.01	0.4195	0.048

Using a central value and a variation, this series of values of Ratio_{Void} can be represented by a distribution $0.045 \pm 10\%$.

For three possible products of the UO₂ reaction (see Section 4.1.5.2, Table 4) and the central value of Ratio_{Void}, the values of Ratio_{Altered} are given in Table 10.

Table 10. The Ratio of Cross-Sectional Area of Fuel Reacted to Total Fuel Area, for Fresh Fuel, for a Gap/Fuel Area Ratio Averaged over Several Fuel Designs, for Several Possible Product Solids of the Fuel Reaction

Product Solid	D ^a	Ratio _{Altered}
Dehydrated schoepite	0.82	0.055
Metaschoepite	1.62	0.028
Na-boltwoodite	2.93	0.015

NOTE: ^a D = the fractional increase in specific volume

For a larger-scope performance-assessment model, the reaction product should be dehydrated schoepite, which would be favored to form at high temperatures, e.g., near 100°C. Dehydrated schoepite gives the largest fraction of altered fuel.

In vapor or low water drip rate experiments at 90°C, a mixture of dehydrated schoepite and metaschoepite were formed (Finch et al. 1999, Fig. 1d). Metaschoepite is the expected precipitate for lower temperatures, in the vicinity of 50°C (Finch et al. 1998, p. 833). Metaschoepite is known to dehydrate to dehydrated schoepite in water at temperatures near 100°C (Finch et al. 1998, p. 832). Na-boltwoodite is likely to be infrequent because it requires silica, which is limited in the groundwater (see Section 4.1.5). The temperature declines after an early peak value during the repository post-closure period, eventually approaching 18-30°C depending on the climate/water influx scenario (DOE 1998, v. 3, p. 3-38, Figure 3-25). Hence metaschoepite is likely to be the most frequent reaction product. Dehydrated schoepite is likely to be the second most frequent product, for the time period and temperature range expected after a waste package may have been breached. The recommended distribution of the values of the fraction of the spent fuel matrix solid which is altered by reaction during this period, is a triangular distribution extending between the values of 0.028 and 0.055 (dimensionless

fractions), with a maximum probability density at the value 0.028, and decreasing linearly to zero probability density at the upper end of the range, 0.055.

The time, in years, for closure of the gap, assuming conservatively that the gap width G in the spent fuel is the same size as in the fresh fuel (see discussion above), and assuming a small ratio G/r_f so that a linearized equation can apply, is

$$t = \frac{\left(\left(\frac{1}{D} \right) G \right)}{S} \quad (\text{Eq. 14})$$

if the gap width G is given in μm . The surface reaction rate of the spent fuel is S $\mu\text{m/yr}$; see Section 4.1.7 for the 10th and 90th percentile values used in the following table. A value for the gap width is taken as the average for the fuels in Table 9, $G=105.7$ μm . The time to closure of the gap for the example inputs is then given in Table 11.

Table 11. The Time for Closure of the Gap, Using an Averaged Gap Width in Fresh Fuel as a Bound for the Gap Width in Spent Fuel, for Several Possible Reaction Product Solids and Reaction Rates

Product Solid	Fractional Increase in Specific Volume D	Reaction Rate S ($\mu\text{m/yr}$)	
		0.024	0.303
		Gap Closure Time (yr)	
Dehydrated schoepite	0.82	5370	425
Metaschoepite	1.62	2720	215
Na-boltwoodite	2.93	1500	120

A time in the range from about 120 years to 5400 years is still short compared to other time scales in waste isolation processes. These times may be overestimates since the as-manufactured gap size was used. Hence, for modeling purposes, the time is taken to be zero. It is conservative to take this time as zero.

Note that among fuel designs there is a wider percentage range in the gap widths than in the ratio of gap area/ fuel area. The range in gap widths contributes to the range in times to closure of the gap, but the relatively large range in these times remains unimportant because even the larger times in the range are still short compared to other time scales in waste isolation processes.

6.7 FURTHER REACTION NEAR THE BREACH POTENTIALLY LEADING TO ROD SPLITTING

The arguments of Section 6.5 have not completely ruled out further reaction of water with the spent fuel near the breach, leading to pressure inside the cladding, further breach opening, and crack extension. Because of the stress amplification near a crack tip, a modest pressure against the walls of a breach can lead to a significant stress at the crack tip. This section addresses the possibility of crack extension from reactions in this region.

Figure 13 shows a crack propagation driven by dry oxidation reactions in the presence of air and elevated temperatures (Einziger and Strain 1986, Figure 10). Expansion of the solid in the spent fuel pellet near the crack tip leads to a pressure on the inside of the cladding and, hence, to a

hoop stress in the cladding. Further back from the crack tip, near the center of the breach region, a modest pressure on the sides of the breached cladding tube leads to a widening of the breach sides and, hence, to a tension across the crack tip. The geometry of the breach extension provides an analog for wet unzipping.

The modest buildup of precipitation-driven force near the open breach region consequent to aqueous reactions cannot be completely ruled out, where the lack of major confinement pressure by the cladding enables reactant access. Hence, the conservative assumption is that this force, and an amplified stress at the crack tip, can happen. The buildup of reaction products with larger volume would cause the crack in the cladding to extend, leading to exposure of additional fuel surface, thus leading to cladding unzipping.

In [Figure 13](#) at a distance of one to four cladding-tube radii back from the crack tip, the opening angle seems to be larger than at the crack tip. This region is taken to be the controlling region for the expansion. For the aqueous case, with prior gaps and cracks in the fuel pellets filled in, the reactions are expected to be limited to the surface of the pellets. As a region under the cladding but near the breach reacts, and expanded solid is hypothesized to push the clad from within (see [Figure 14](#)). This push will expand the cladding elastically at first, opening a new gap almost all around the circumference (see [Figure 14](#)). Hence, it is conservatively assumed that the fuel surface all around the fuel pellet is reacting and contributing to the expanding volume. (The effect of an alternative assumption, with a smaller fraction of the circumference participating in reaction, will be considered later.)

The associated forces are transmitted to the crack tip, extending the crack tip, and opening a smaller gap under the cladding near the crack tip. Thus, near the crack tip, a smaller fraction of the fuel pellet circumference is exposed to reaction than is the case further back.

As the breach widens and the cladding opens up, the force from the solid expansion load is reduced. Zircaloy has a degree of ductility; hence, the crack extension for a given expansion load is limited.

Thus, the feedback process of spent fuel exposure, spent fuel reaction, crack extension, and further spent fuel exposure is the most plausible sequence for the process. The precipitation-driven force near the open breach region is hypothesized (see above in this Section); the gradual crack extension follows from the stress amplification at the crack tip and the feedback process.

The next question is how fast the unzipping can proceed; this speed will be addressed and bounded. The first, bounding, analysis is based on fracture mechanics and the yield stress and elastic shear modulus of the cladding material, and the exposure and reaction rate of the spent fuel. It does not use the ductility properties of the cladding material. The second analysis, a more realistic approach, is based on an experimental measurement of cladding response at a higher temperature to a similar but not exactly the same spent-fuel reaction process.

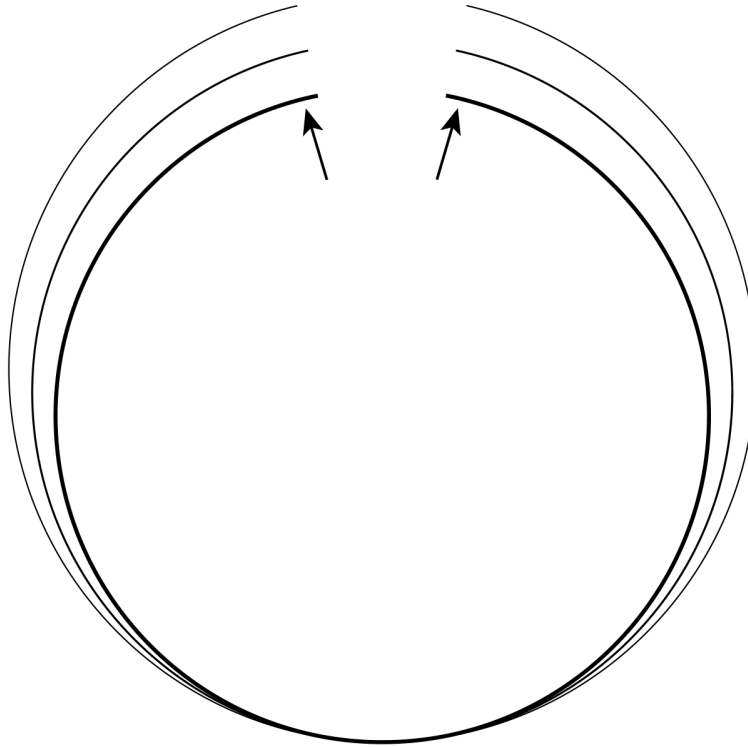


**(a) AXIAL
360°C
51.5 h**

A5B

NOTE: Einziger and Strain 1986

Figure 13. An Extending Breach Driven by Dry Oxidation at Elevated Temperature



NOTE: As a cylindrical tube section is pushed outward at two locations near a breach, the elastic property of the tube material causes a flexure in the section, tending to open up more of the perimeter. Thus, a gap volume develops to greater extent between the expanding tube and a contained solid cylinder (i.e., a spent fuel pellet).

Figure 14. Gap Extension Due to Tube Section Flexure

6.7.1 Bounding Model for Unzipping Velocity v_2

Classical fracture mechanics primarily addresses problems of crack propagation initiation by setting semi-empirical failure criteria. These criteria are usually provided in terms of stress intensity factors; K_I , K_{II} , and K_{III} for the different modes of fracture initiation (Cherepanov 1979, p. 59). The K_I , K_{II} , and/or K_{III} stress intensity factors depend on the shape of the body (geometry), prescribed external loads and/or displacements imposed (boundary conditions), and length of crack(s). The threshold of stress intensity factor to initiate crack propagation corresponds to a threshold of attainable displacements and/or stresses in a local neighborhood of an existing crack or structural flaw. In many problems of fracture mechanics, a crack may continue to propagate once it has started, if the external force load is constant.

As noted above, in the present case of internal solid expansion presenting a displacement load on the cladding, the force is reduced as the crack expands. Hence, the crack extends only very slowly as the solid reaction continues to provide more volume expansion.

After crack initiation, the crack is assumed to extend or propagate at a quasi-steady rate (i.e., very small speed/acceleration changes) that is slow in comparison to the wave speeds of the cladding material. The rate or speed that the crack propagates axially along the spent fuel rod is evaluated from an analysis of local failure conditions that remain constant quantities if one were

to travel in moving reference frame at an arbitrary position of the elastic domain in front of the crack tip (Cherepanov 1979, pp. 200–203). Of these several proposed criteria for local failure; namely, plastic crack tip zone, crack tip radius, crack opening displacement, mean strain over a plastic zone, stress state limit, or “Cherepanov’s Generalized Criterion of Local Failure” (Cherepanov 1979, pp. 202–203), all have an equivalence or self-consistency amongst themselves in that a local metric condition at the crack tip must be attained before an existing crack or flaw begins to propagate. Since all of these criteria are self-consistent, a model of crack propagation speed to evaluate the cladding unzipping rate can be formulated from any one of them. To model slow, quasi-steady crack propagation, not only must the local metric condition at the crack tip be attained, but it also must be maintained at a constant value for the crack to continue to propagate at nearly constant speed. For cladding unzipping, the crack-opening displacement criterion is the one that leads to a useful and simple result. The result is simple in that the crack speed depends on readily accepted material parameters of the elastic shear modulus and the plastic yield stress, and on the imposed boundary condition for the opening rate along the crack process zone length. The crack process zone length, shown in Figure 19, is an axial length along which the phase change reaction (UO_2 to a Schoepite or Boltwoodite, see Section 4.1.5) is proceeding to completion. Solid expansion in the zone provides an opening force at the crack tip and a crack-tip stress field.

The equation describing the crack propagation velocity makes use of a coordinate system moving at the same velocity as the advancing crack tip. After a startup period the region behind the crack tip has a consistent shape moving steadily along the fuel rod. A coordinate system $\mathbf{y} = (y_1, y_2, y_3)$ is defined as being fixed in space. A coordinate system $\mathbf{x} = (x_1, x_2, x_3)$ is defined as moving with the crack tip velocity v_2 (see Figure 20). \mathbf{x} is a function of \mathbf{y} and time t :

$$\begin{aligned}x_1(t) &= y_1 \\x_2(t) &= y_2 + v_2 \cdot t \\x_3(t) &= y_3\end{aligned}\tag{Eq. 15}$$

The displacement $\mathbf{w}(\mathbf{y},t) = (w_1(\mathbf{y},t), w_2(\mathbf{y},t), w_3(\mathbf{y},t))$ of a point in the solid cladding tube is the difference between the material point’s location at time t and its location \mathbf{y} at the starting time zero.

Next the displacement $\mathbf{u} = (u_1, u_2, u_3)$ associated with a reference point \mathbf{x} moving with velocity v_2 in the \mathbf{y} coordinate system is

$$\mathbf{u}(\mathbf{x},t) = \mathbf{u}(\mathbf{x}(\mathbf{y},t),t)\tag{Eq. 16}$$

The steady state of the geometric shape near and trailing the crack tip implies that, for a point \mathbf{u} in this region,

$$\frac{d\mathbf{u}}{dt} = 0\tag{Eq. 17}$$

By a chain rule for derivatives it follows that:

$$\begin{aligned}
 0 &= \frac{d}{dt} u_3(\mathbf{x}, t) = \frac{\partial}{\partial t} u_3(\mathbf{x}, t) + \sum_i \frac{\partial}{\partial x_i} u_3(\mathbf{x}, t) \times \frac{\partial x_i}{\partial t} \\
 &= \frac{\partial}{\partial t} u_3(\mathbf{x}, t) + v_2 \frac{\partial}{\partial x_2} u_3(\mathbf{x}, t)
 \end{aligned} \tag{Eq. 18}$$

Thus, for this restricted coordinate system the axial crack velocity component v_2 is related to the u_3 crack opening rate and the spatial derivative of the u_3 crack opening with respect to the x_2 coordinate by:

$$v_2 = \frac{\frac{-\partial(u_3(x(t), t))}{\partial t}}{\frac{\partial(u_3(x(t), t))}{\partial x_2}} \tag{Eq. 19}$$

It remains to pick a convenient point \mathbf{u} where the two partial derivatives can be evaluated. The strategy in the following steps is to pick a \mathbf{u} where $\partial u_3 / \partial x_2$ can be evaluated and is relatively large compared to its value at other points, and then to find a value, which bounds the $\partial u_3 / \partial t$ of that \mathbf{u} .

The (32) second-order tensor term $\partial(u_3(x(t), t)) / \partial x_2$ is related to the (32) component of elastic strain, γ_{32} , in the elastic domain, i.e., everywhere except in the plastic zone very near the crack tip (Sokolnikoff 1956, pp. 20–25), by:

$$\gamma_{32} = \frac{1}{2} \left\{ \frac{\partial(u_3(x(t), t))}{\partial x_2} + \frac{\partial(u_2(x(t), t))}{\partial x_3} \right\} \tag{Eq. 20}$$

The region close to the crack tip on the Zircaloy tube can be approximated by a plane sheet of Zircaloy subject to a uniform tensile stress σ_{33} (generated by the spent fuel pellet expansion and the widening of the breach opening further back from the crack tip) and containing a crack. Then the crack is in the Mode I loading of fracture mechanics. In linear elastic fracture mechanics (LEFM), the stress field in the zone approaching the crack is (Kanninen and Popelar 1985, p. 145, Figure 5):

$$\begin{aligned}
 \sigma_{22} &= K_I (2\pi r)^{-0.5} \cos\left(\frac{\theta}{2}\right) \left(1 - \sin\left(\frac{\theta}{2}\right) \sin\left(\frac{3\theta}{2}\right)\right) \\
 \sigma_{33} &= K_I (2\pi r)^{-0.5} \cos\left(\frac{\theta}{2}\right) \left(1 + \sin\left(\frac{\theta}{2}\right) \sin\left(\frac{3\theta}{2}\right)\right) \\
 \sigma_{23} &= K_I (2\pi r)^{-0.5} \cos\left(\frac{\theta}{2}\right) \sin\left(\frac{\theta}{2}\right) \cos\left(\frac{3\theta}{2}\right)
 \end{aligned} \tag{Eq. 21}$$

where

r = the radial distance from the crack tip

θ = the angle from the x_2 direction, in the (x_2, x_3) plane

K_1 = the stress intensity factor, proportional to the large-scale uniform tensile stress σ_{33}

In the plane strain condition, there is also a σ_{11} component $\sigma_{11} = \nu(\sigma_{22} + \sigma_{33})$ where ν is Poisson's ratio. In the plane stress condition, $\sigma_{11} = 0$. The condition for the present crack geometry is expected to be intermediate, but closer to plane stress.

The associated displacement fields near the crack tip are (Kanninen and Popelar 1985):

$$\begin{aligned} u_2 &= (K_1/2\mu) (r/2\pi)^{0.5} \cos\left(\frac{\theta}{2}\right) (\kappa-1+2 \sin^2\left(\frac{\theta}{2}\right)) \\ u_3 &= (K_1/2\mu) (r/2\pi)^{0.5} \sin\left(\frac{\theta}{2}\right) (\kappa+1-2 \cos^2\left(\frac{\theta}{2}\right)) \end{aligned} \quad (\text{Eq. 22})$$

where

$\kappa = 3 - 4\nu$ in plane strain

$\kappa = \frac{3-\nu}{1+\nu}$ in plane stress

μ = the elastic shear modulus

ν = Poisson's ratio

The use of the LEFM approach is based on the assumption that the stress field is within the elastic range except in a small region near the crack tip, and that the inelasticity near the crack tip does not greatly change the elastic stress field from that given by the above equations.

The limit of the elastic stress values, i.e., the yield condition used, is the Von Mises yield condition. Kanninen and Popelar (1985, p. 124) gives this quantity in terms of principal stresses. In terms of stresses in the (x_1, x_2, x_3) coordinate system, Hellen (1984, p. 289) gives:

$$\left(\frac{1}{6}\right) [(\sigma_{11} - \sigma_{22})^2 + (\sigma_{22} - \sigma_{33})^2 + (\sigma_{33} - \sigma_{11})^2] + \sigma_{12}^2 + \sigma_{23}^2 + \sigma_{31}^2 = \frac{1}{3} \sigma_{\text{yield}}^2 \quad (\text{Eq. 23})$$

where

the left-hand side is the stress quantity to be compared to the limit value on the right-hand side

σ_{yield} = the yield stress in a uniaxial tension test

In the following evaluation, a suitable angle is chosen where the shear term contributes a large fraction of the total stress. Then $\partial u_3 / \partial x_2$ is evaluated at the location along the line at this angle where the stress just reaches the yield stress. The analysis is graphical and approximate. The approximation is sufficiently accurate as explained after Equation 27.

The angular dependence of the above stress-squared quantity, for a fixed value of the distance r , is given in Figure 15 for plane strain and in Figure 16 for plane stress. On the same figures the contribution from the σ_{23}^2 component is plotted. As r decreases along a fixed angle θ , the stress quantity approaches the yield condition where the quantity equals $\frac{1}{3} \sigma_{\text{yield}}^2$. It is seen that at about 110° , the σ_{23}^2 term is about 0.67 to 0.96 of the total stress quantity, for plane stress and plane strain respectively. At the yield point, the σ_{23}^2 term is about 0.67 to 0.96 of $\frac{1}{3} \sigma_{\text{yield}}^2$.

There, σ_{23} is about 0.8 to 0.98 of $\frac{\sigma_{\text{yield}}}{\sqrt{3}}$.

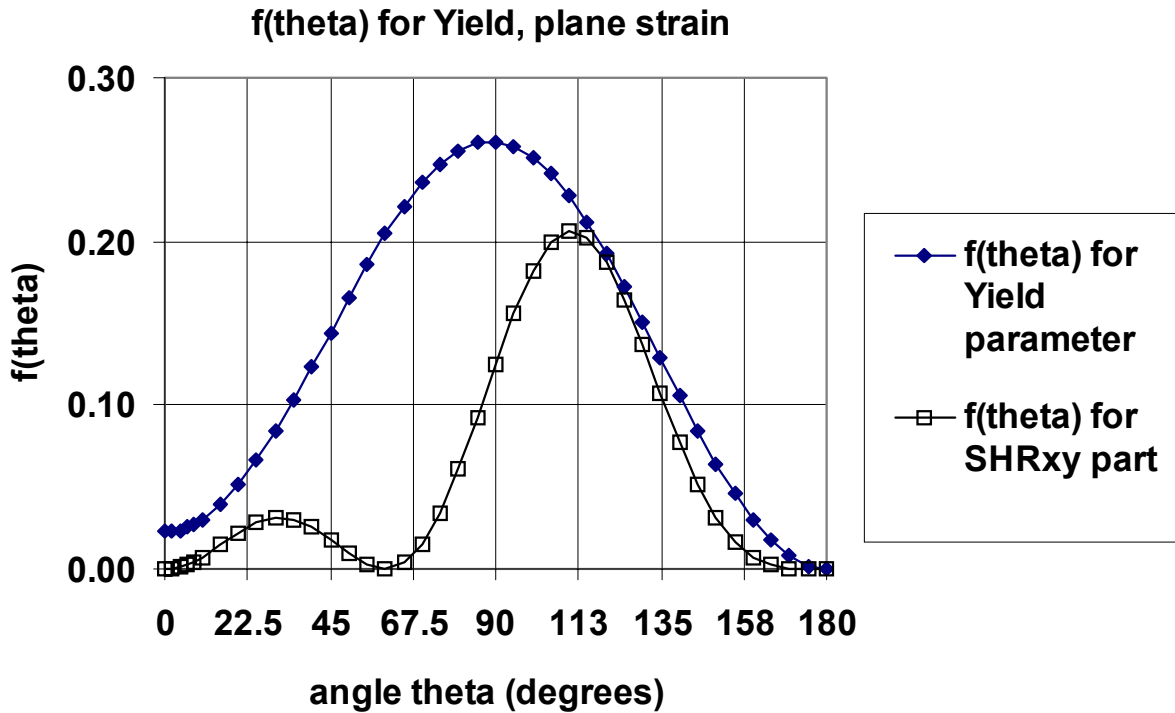


Figure 15. Angular Dependence of the Stress-Squared Quantity near the Crack Tip and in the Elastic Zone, for a Constant Radial Distance r from the Crack Tip, for Plane Strain

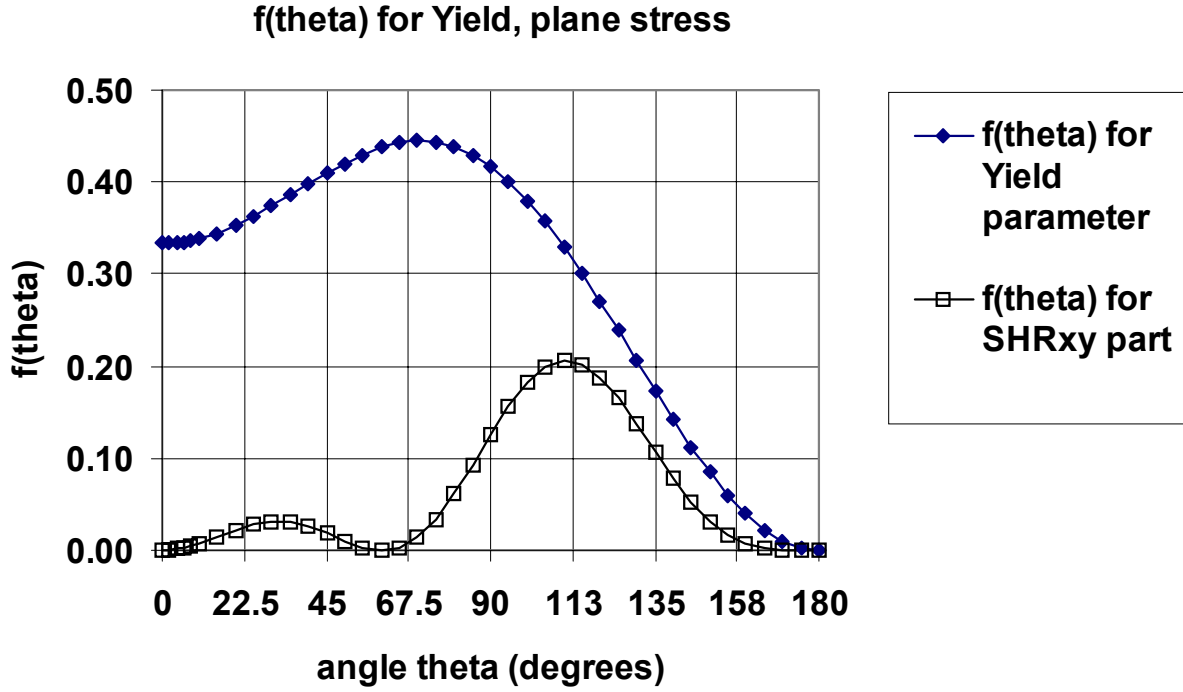


Figure 16. Angular Dependence of the Stress-Squared Quantity near the Crack Tip and in the Elastic Zone, for a Constant Distance r from the Crack Tip, for Plane Stress

The stress component is proportional to the strain component (Sokolnikoff 1956, p. 71):

$$\sigma_{32} = 2 \mu \gamma_{32} \quad (\text{Eq. 24})$$

where γ_{32} is given by Equation (20), and μ is the elastic shear modulus, which is related to Young's modulus E and the Poisson's ratio ν by (Sokolnikoff 1956, p. 71):

$$\mu = \frac{E}{2(\nu + 1)} \quad (\text{Eq. 25})$$

E and ν are given in Section 4.1.2.

At the same angle $\theta = 110^\circ$ examined above, the $\partial u_3 / \partial x_2$ term is about 3.7 to 3 times the total γ_{32} of Equation (20) for plane strain and plane stress respectively; see Figures 17 and 18.

Hence, at $\theta = 110^\circ$,

$$\begin{aligned} \frac{\partial u_3}{\partial x_2} &= (3.7 \text{ to } 3) \times \gamma_{32} \text{ (using Figures 17 and 18)} \\ &= (3.7 \text{ to } 3) \times (1 / 2\mu) \times \sigma_{32} \text{ (using Equation 24)} \end{aligned}$$

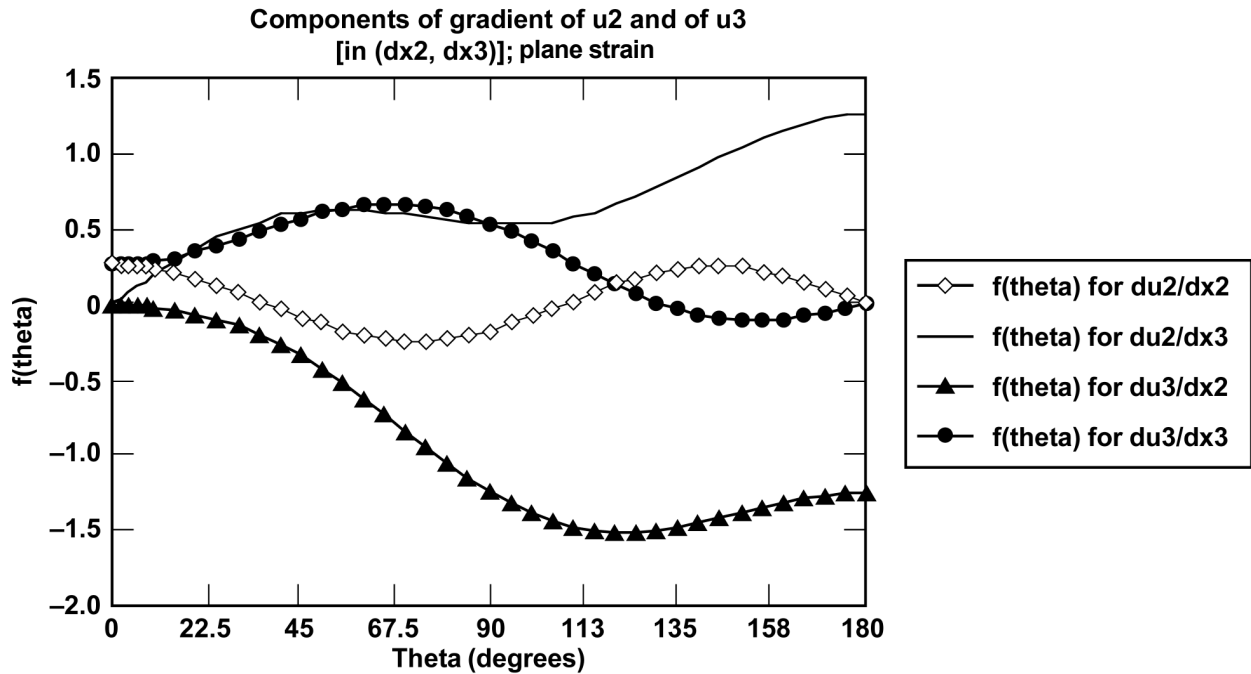
$$= (3.7 \text{ to } 3) \times (1/2\mu) \times (0.8 \text{ to } 0.98) \times \frac{\sigma_{yield}}{\sqrt{3}} \quad (\text{using Figures 15, 16 and Equation 23})$$

$$= (3.0 \text{ to } 2.9) \times (1/2\mu) \times \frac{\sigma_{yield}}{\sqrt{3}}$$

$$= (0.9 \text{ to } 0.8) \times (1/\mu) \times \sigma_{yield} \quad (\text{Eq. 26})$$

where the two numerical multiplier alternatives apply for plane stress and plane strain respectively. The multiplier is rounded to uniformly 1.0 for the model; then the approximate equation at the selected angle and distance from the crack tip is:

$$\frac{\partial u_3}{\partial x_2} = \frac{1}{\mu} \times \sigma_{yield} \quad (\text{Eq. 27})$$

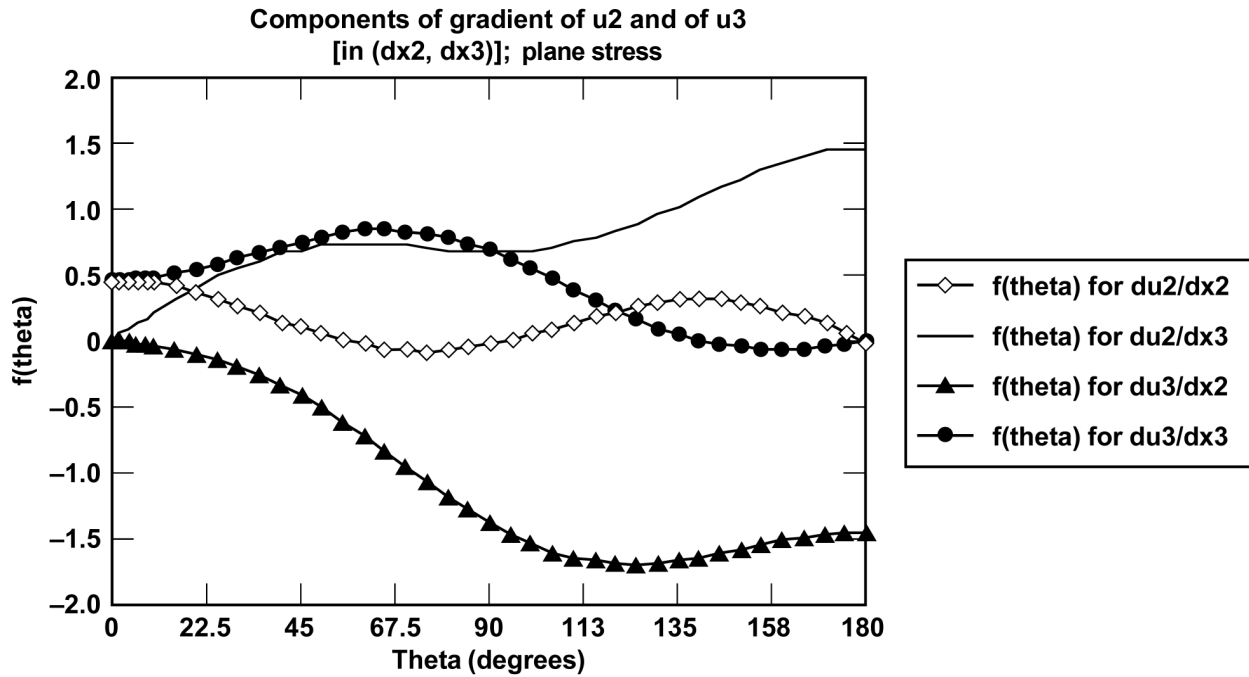


NOTE: The shear component of strain, γ_{32} , is one-half the sum of $\frac{\partial u_3}{\partial x_2}$ and $\frac{\partial u_2}{\partial x_3}$.

Figure 17. Angular Dependence, for a Constant Distance r from the Crack Tip and in the Elastic Zone, of the Partial Derivatives of the Displacement Components u_2 and u_3 , for Plane Strain

The stress-strain situation is closer to plane stress than plane strain; hence, the roundoff is close to a 10% error. Another aspect of the model is an overestimate (see evaluation location for $\frac{\partial(u_3(x(t),t))}{\partial t}$ below), so a difference of even up to 20% here is not major.

It remains to evaluate $\partial(u_3(\mathbf{x}(t),t))/\partial t$. This is not easily evaluated at the same point, so another point is selected, which can provide a value bounding the desired value at the first point. The point selected is well behind the crack tip, at a location where the two sides of the breach are moving apart at a rate under the influence of the reacting spent fuel pellet, not substantially constrained by the connected sides in front of the crack tip. Note that at a point \mathbf{x} in advance of the crack tip, $\partial u_3/\partial t$ is zero. $\partial u_3/\partial t$ is continuous in \mathbf{x} . At the point \mathbf{x} where $\partial u_3/\partial x_2$ is evaluated and $\partial u_3/\partial t$ is desired, $\partial u_3/\partial t$ has an intermediate value. Hence, using a point far back from the crack tip to evaluate $\partial u_3/\partial t$ gives a substantial overestimate.



NOTE: The shear component of strain, γ_{32} , is one-half the sum of $\frac{\partial u_3}{\partial x_2}$ plus $\frac{\partial u_2}{\partial x_3}$.

Figure 18. Angular Dependence, for a Constant Distance r from the Crack Tip and in the Elastic Zone, of the Partial Derivatives of the Displacement Components u_2 and u_3 , for Plane Stress

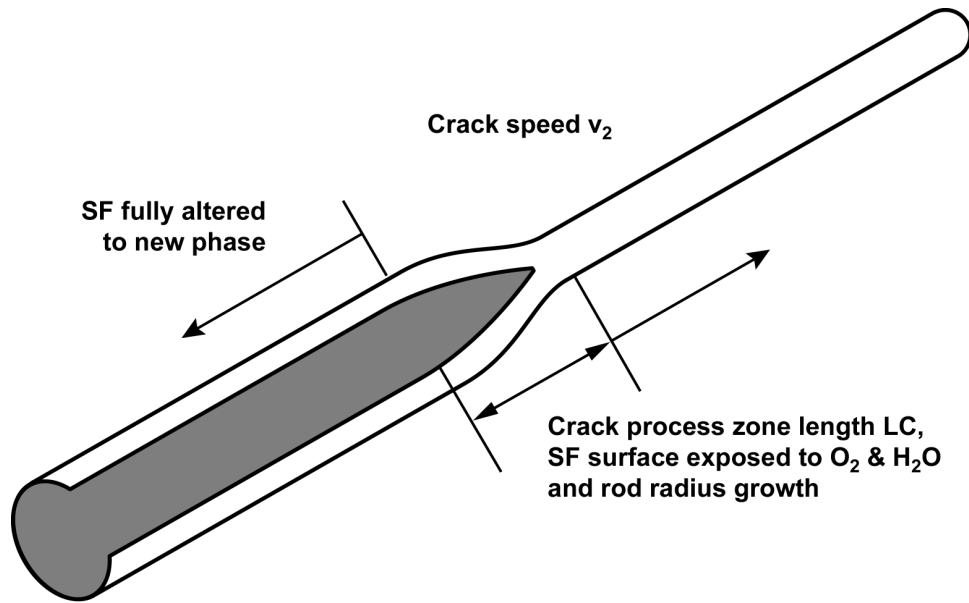
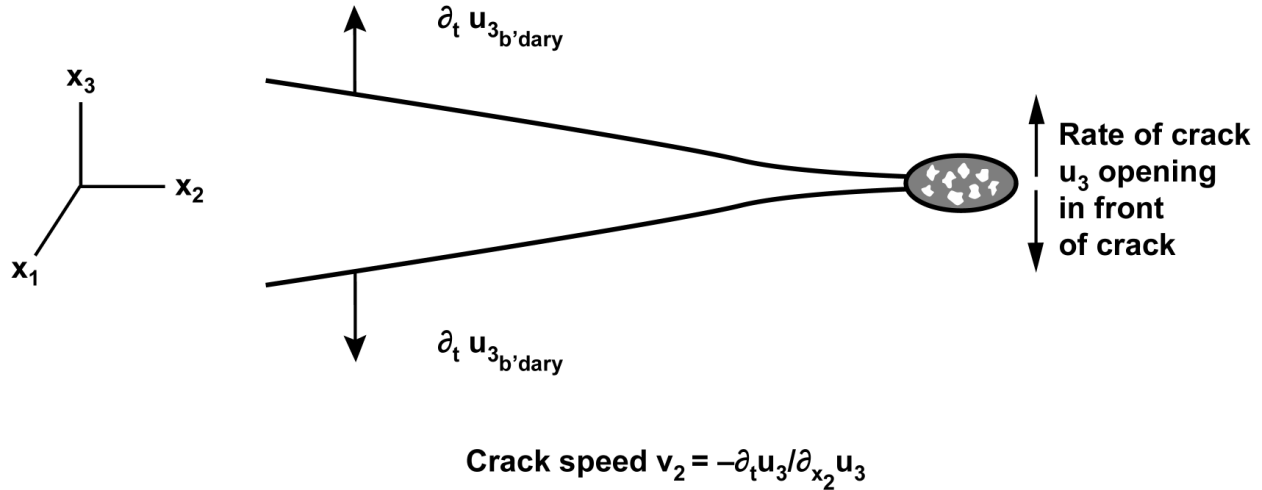


Figure 19. Spent Fuel Rod Showing the Crack Process Zone where the Crack Propagation is Driven by Alteration and Expansion of the Spent Fuel Solid



NOTE: (u_1, u_2, u_3) is a coordinate system anchored in the cladding rod solid. (x_1, x_2, x_3) is a Cartesian space coordinate system. As the interior solid spent fuel is exposed and reacted, its expansion causes the cladding crack to open, carrying the solid cladding with it. At the same time, the crack extends in the x_2 direction. A large-scale almost-steady-state pattern of stress and displacement is moving steadily in the x_2 direction.

Figure 20. A Close-Up of the Crack Process Zone and the Crack Tip

In the crack process zone, the spent fuel is altering at a surface rate S (see Section 4.1.7). At locations well back from the crack tip, it is assumed that (i) the full circumference of the spent

fuel pellet is exposed to further reaction. It is also assumed that (ii) the final shape of the spent fuel plus its solid reaction products is circular at any one axial distance, (iii) axial displacement of products is constrained so that the increase in volume must be provided from an increase in cross-sectional area, and further (iv) there is only a small depth of reaction progress into the fuel pellet, so that the net radius of pellet plus solid products is nearly linearly proportional to the depth of reaction progress.

The net solid surface is then expanding outward at a rate equal to $D \times S$ where D is the fractional increase in specific volume (Equation 12).

(For example, assuming dehydrated schoepite as the product, D is 0.82.)

To accommodate the expanding solid, the cladding circumference is expanding at a rate $2\pi \times D \times S$, and the opening of the breach is providing all of this expansion. Thus, at the breach the lateral component of the opening rate is $2\pi \times D \times S$ (see [Figure 14](#) and [Figure 21](#), which serve to illustrate an opening gap in a tube around a cylindrical cross-section). This formulation assumes a small to moderate opening angle, so that the straight-line opening distance is to an adequate approximation equal to the circumferential distance joining the two edges. Each of the two sides of the breach is then moving outward at a rate:

$$\frac{\partial u_3}{\partial t} = \pi D S. \quad (\text{Eq. 28})$$

Further along into the process zone, the separated edges of the breached cladding are actually moving with a rotation toward a vertical alignment, as well as moving outward, to accommodate the expansion of the reacting solid inside (see [Figure 13](#)). Nearer the crack tip, where the edge movement due to the expansion of the cladding circumference is primarily horizontal, but where the full circumference under the breach is exposed to reaction, is where the maximum of $\frac{\partial u_3}{\partial t}$, as given in Equation 28, is located. Thus, a point \mathbf{u} in the cladding in this region provides a $\frac{\partial u_3}{\partial t}$ value which is an upper bound on $\frac{\partial u_3}{\partial t}$ elsewhere. Thus, v_2 in Equation 19 is bounded by the evaluation:

$$\begin{aligned} v_2 &= \left\{ \frac{\mu}{\sigma_{yield}} \right\} \left\{ \frac{\partial(u_3(x(t), t))}{\partial t} \right\} \\ &= \left\{ \frac{\mu}{\sigma_{yield}} \right\} \pi D S \end{aligned} \quad (\text{Eq. 29})$$

The shape of the reaction surface, as the crack advances, is a cone, with its base at the crack tip, and getting closer to the centerline of the spent fuel for distances further back from the crack tip. Thus, the reaction front, on the cone surface, is at a small angle to the axial direction. Thus, the

reaction front is on the hypotenuse rather than on the long side of a right triangle. This angle leads to a correction factor to Equation 29 of $\sqrt{1 + \left(\frac{\sigma_{yield}}{\pi\mu D}\right)^2}$. With the parameter values used, this correction factor is at most a few per cent greater than one. Hence, it will be omitted in the evaluation of v_2 .

Example calculation:

The unzipping velocity is calculated using Equation (29) with Equation (25) and Equation (12). The inputs selected for the example calculations are:

Young's modulus E and Poisson's ratio ν : average values from Section 4.1.2:

$$E = 96.2 \text{ GPa}, \nu = 0.36.$$

Yield stress of Zircaloy: average value at 60°C, from Section 4.1.2: $\sigma_{yield} = 767 \text{ MPa}$.

Increase in specific volume, D of Equation (12) depends on specific volumes, Section 4.1.4, Table 2.

Spent fuel reaction rate S: approximate 10th and 90th percentiles from Section 4.1.7: $S = 0.024$ and $0.303 \text{ } \mu\text{m/yr}$.

With these equations and inputs, the unzipping velocity v_2 in $\mu\text{m/yr}$ is described by

$$v_2 = 145 \cdot D \cdot S \text{ and the } v_2 \text{ values for various values of } D \text{ and } S \text{ are given in Table 12.}$$

Table 12. Unzipping Velocity as a Function of Solid Product Type and Spent Fuel Alteration Rate

Product Solid	Fractional Increase in Specific Volume D	Alteration Rate S ($\mu\text{m/yr}$)	
		0.024	0.303
		Unzipping Velocity ($\mu\text{m/yr}$)	
Dehydrated schoepite	0.82	2.9	36.
Metaschoepite	1.62	5.6	71.
Na-boltwoodite	2.93	10.2	129.

Metaschoepite is the predominant reaction product, because the unzipping extends over a long time duration, when the temperature is declining well below 100°C (DOE 1998, vol. 3 p. 3-38 Fig. 3-25). Dehydrated schoepite is not preferred at temperatures much below 90°C. Na-boltwoodite is not formed in a major quantity because of the limited availability of silica in the groundwater; see Section 4.1.5 and Section 6.6 after Table 10.

The unzipping time duration is related to the velocity v_2 by:

$$t = \frac{L}{v_2} \quad (\text{Eq. 30})$$

where L = length of fueled rod to be unzipped. A lower-bound value of a half-length of a rod is $L = 1.6$ meters. This is a conservative value as it will predict shorter unzipping durations (Section 4.1.1). Continuing the example calculation, the corresponding time durations of unzipping, if no other processes create additional breaches during this time, are given in Table 13.

Table 13. Unzipping Time Duration as a Function of Solid Product Type and Spent Fuel Alteration Rate

Product Solid	Fractional Increase in Specific Volume D	Alteration Rate S ($\mu\text{m}/\text{yr}$)	
		0.024	0.303
		Unzipping Time (yr)	
Dehydrated schoepite	0.82	5.5×10^5	4.4×10^4
Metaschoepite	1.62	2.9×10^5	2.3×10^4
Na-boltwoodite	2.93	1.6×10^5	1.2×10^4

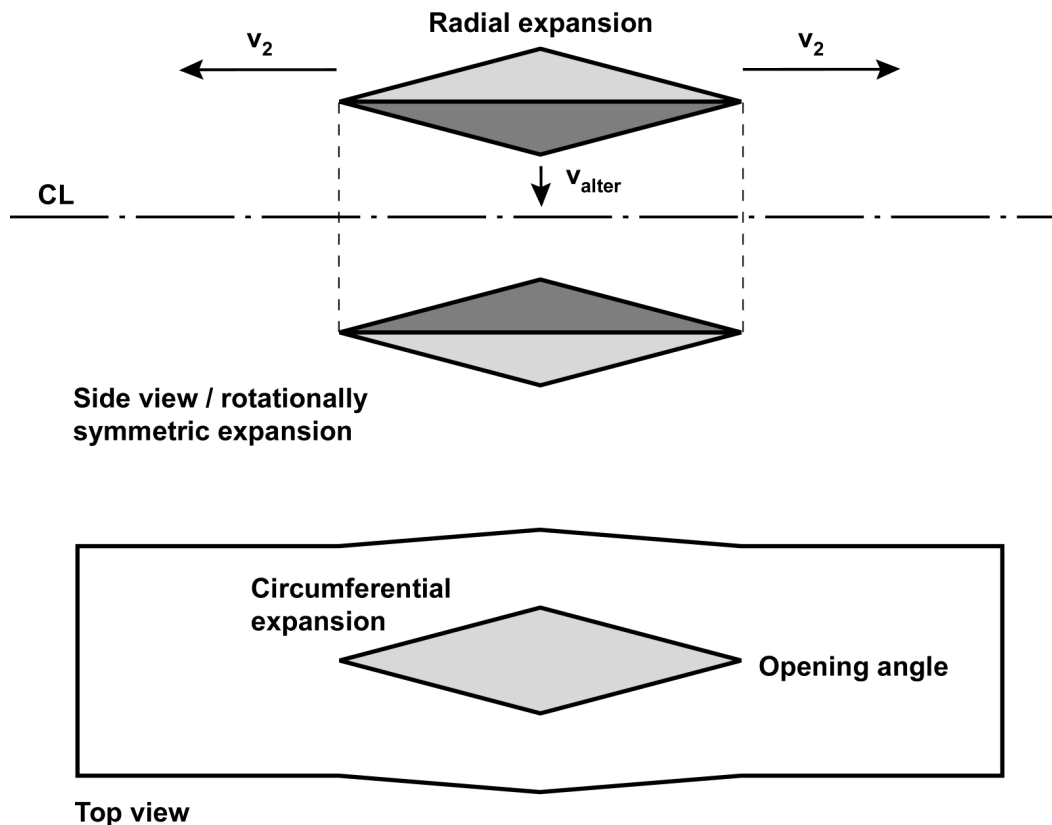
6.7.2 Alternate Method for Estimating v_2

A more realistic alternate approach to estimate the speed of crack-tip advance is to observe experimentally the result embodied in the shape of a breached fuel rod at a considerable time after the fuel inside the breached rod has started to be exposed to reaction. As noted, dry oxidation, with results as in Figure 13, is used as an analog for a wet unzipping process. The iterative process between the fuel reaction and the crack advance are reviewed in the next paragraph. The process leads to the concept, explained in following paragraphs, that the shape of the breached cladding tube in the breach zone is dependent on the shape of the reacted fuel cylinder (multiple pellets along the length), which is dependent on the rates of advance of the crack tip and the fuel solid reaction front.

As noted at the beginning of Section 6.7, the unzipping process is a type of feedback cycle, with fuel expansion, clad yielding at the crack tip, and more fuel exposed to reaction. At a distance of several cladding-tube radii back from the crack tip, as reaction products push out the cladding along the breach's edge, more of the circumference of the fuel pellets becomes exposed to the environment of moist air or water, and so can join the reaction. It is likely that at some point nearly the entire circumference becomes involved. Inner volume of the pellets cannot react early, because the cracks were filled during the earlier phase. As the crack tip advances, the already-exposed surfaces behind the crack tip continue to react from the outer surface inward. Thus, the region furthest away from the crack tip, which has been exposed for the longest time, has had time for more progress of reaction front into the solid pellet.

Therefore, the depth of the reaction front into the solid cylinder is greatest at the furthest from the crack tip. And it is proportionally deep for smaller distances back from the crack tip, at any time. Thus, the reaction front is, broadly speaking, a conical surface section in the length segment between the crack tip and the location of the original small breach. Because of the product expansion, the net solid occupied by the initial fuel plus its reaction product is approximately an expanding cylindrical section (see Figure 21). This cylindrical shape is an approximation good for small depths of reaction progress compared to the total radius. (For large depths of progress of the reaction front, the external shape to accommodate the volume is

not linearly proportional to the reaction distance. This refinement will be discussed separately below.)



NOTE: (Top) Rotational view about the axial Centerline of a spent fuel rod with a breach. The expanding solid products from spent fuel alteration cause a radial expansion of volume. The volume is thickest at the midpoint, because that location has been exposed to continuing alteration for the longest time. The altered volume is thinnest at the crack tip, because that location has just become exposed by the advancing crack tip. (The solid product volume just filling the initial fuel-cladding gap is not included in this picture.)

(Bottom) Circumferential expansion (as well as extension) of the crack opening, to accommodate the additional volume shown in (a). Near the crack tip, and in the entire crack for early times, the cladding surface is described by open circles of increasing radius as one moves from crack tip to mid-point. As time passes, the expansion of the interior solid will cause the cladding surface near the mid-point of the crack edge to turn upward as well; this is not included in the present model, as it may or may not affect the crack tip zone.

Figure 21. Rotational View about the Axial Centerline of a Spent Fuel Rod with a Breach and Circumferential Expansion of the Crack Opening

As the solid expands, the cladding wall must expand, and the expansion of the wall circumference is provided almost entirely by the gap; see Figures 13, 14, and 21. Thus, the gap expands as a function of the solid outer radius, which depends on distance from the advancing crack tip. For small expansions, a useful approximation is that the expansion is linearly proportional to the increase in solid's circumference. As a later step in this small-expansion approximation, the circumferential distance of the gap will be used as approximately equal to the chord distance, i.e., straight-line separation of the opposite sides of the gap. This linear approach

accords approximately with the visual evidence of Figure 13 where the gap width appears to be approximately linear with distance from the crack tip.

Data extracted from a photograph (reproduced as Figure 13) of a Zircaloy crack opening is used in the present alternate method. The first limiting statement for the method is the following. This photographic measurement technique is at present a very approximate, non-qualified method. If it looks promising, the method can be replicated on new samples where the requisite data are measured carefully.

A second consideration is the temperature value in the experimental data, 360°C, as compared to the temperature range of interest for wet unzipping, 18 to 100°C. The opening angle depends on the ductility of Zircaloy. Three measures of ductility in irradiated Zircaloy change by up to a factor of two between 360°C and the range 18 to 100°C. The uniform elongation in a tensile test is approximately constant (Figure 6). The total elongation in a tensile test is approximately constant in the range 18 to 100°C and approximately a factor of two higher at 360°C (Figure 7). The fracture toughness K_{IC} is approximately a factor of two smaller in the range 18 to 100°C than at 360°C (Figure 9). Hence, the opening angle as measured, or more specifically the tangent of the angle (see below), may be up to a factor of two smaller in the range 18 to 100°C than that measured in the 360°C experiment.

The photograph (Einziger and Strain 1986, Figure 3) of a Zircaloy crack opening caused by air oxidation of the contained UO_2 to U_3O_8 (via U_4O_9) shows an opening angle of approximately 13 degrees on either side of the crack center line. From the photo, measured 35 mm along each side, and 16 mm across, which covers two times the angle θ . Then $\sin \theta = 0.5 \cdot 16/35 = 0.229$, $\theta = 13.2^\circ$. The estimated measurement error is $\pm 10\%$. Possible error from rotation of the rod in the photo, at what appears to be an approximately 45° rotation, is $(-0\%, +41\%)$ since $1/\sin 45^\circ = 1.414$. Then $\tan \theta = 0.235$, for the experimental point at 360°C. In the temperature interval 18-100°C, when the ductility is about half as large, then $\tan \theta$ is half as large, i.e., $\tan \theta = 0.117$ and $\theta = 6.7^\circ$. (The numerator in $\tan \theta$ is the direction across the crack tip; in this direction there is the greatest tensile stress and the material is being strained.)

The shape of the triangle as seen at any one time follows from its development over time, i.e., the ratio of side lengths equals the ratio of velocities; i.e., the ratio depends on the crack advance velocity v_2 and the sideward velocity of the breach's edge, $(\partial u_3/\partial t)$, which depends on the rate of the spent fuel volume increase. That is, in equation form,

$$\tan \theta = \frac{\frac{\partial u_3}{\partial t}}{v_2} \quad (\text{Eq. 31})$$

When assuming (i) there is reaction proceeding on all of the circumferential surface, (ii) the final shape of the spent fuel plus its solid reaction products is circular at any one axial distance, (iii) axial displacement of products is constrained so that the increase in volume must be provided from an increase in cross-sectional area, and (iv) assuming further a small depth of reaction progress into the fuel pellet so that the net radius of pellet plus solid products is nearly linearly proportional to the depth of reaction progress, then

$$\frac{\partial u_3}{\partial t} = \pi D S \quad (\text{Eq. 28})$$

Equation 28 applies here for the same reason it applies in the bounding model.

Then from Equation 31,

$$\begin{aligned} v_2 &= \frac{\frac{\partial u_3}{\partial t}}{\tan \theta} \\ &= \left(\frac{\pi}{0.117} \right) D S \\ &= 26.9 D S \end{aligned} \quad (\text{Eq. 32})$$

for the opening angle of 6.7° expected in the interval 18–100°C as based on the one experimental point at 360°C.

The uncertainties in the proportionality constant 26.9 include the following. There is a measurement error of ±10%. There is an uncertainty of (–30%, +0%) due to photo rotational position since $1/1.414 = 0.71 = 1 - 0.29$, and –0.29 is rounded to –0.30. There is an adjustment for the ductility difference for the data point's temperature and the temperatures in application; this uncertainty is ±30%, or if no adjustment applies, then the constant given above is high by a factor of 2. There is no information on the measurement-to-measurement variability of the opening angle under given conditions; only one point from a possible distribution of measurements is available.

The proportionality of v_2 to $D \times S$ found in the example application of the bounding model earlier, $v_2 = 145 D S$, is larger than the proportionality found immediately above, $v_2 = 26.9 D S$, based on one adjusted experimental point, by a factor of 5.4. Based on the uncertainties of the parameters in both approaches, there is a symmetric uncertainty in this factor of about ±40%, and an asymmetric uncertainty whereby the factor could be larger by another multiplicative factor of between 1.4 and 2.8. By this comparison the experimental point gives at least some quantitative indication of the degree of difference between the bounding model and a realistic model or an experiment.

Example calculation:

The unzipping velocity is calculated using Equation 32 based on the experimental point. The inputs selected for the example calculations are the same as in the earlier example calculation:

Increase in specific volume, D of Equation (12) depends on specific volumes, Section 4.1.4, [Table 4](#).

Spent fuel reaction rate S : approximate 10th and 90th percentiles from Section 4.1.7: $S = 0.024$ and $0.303 \mu\text{m/yr}$.

With this equation and inputs, the unzipping velocity v_2 in $\mu\text{m/yr}$ is given in Table 14.

Table 14. Unzipping Velocity as a Function of Solid Product Type and Spent Fuel Alteration Rate

Product Solid	Fractional Increase in Specific Volume D	Alteration Rate S ($\mu\text{m/yr}$)	
		0.024	0.303
		Unzipping Velocity ($\mu\text{m/yr}$)	
Dehydrated schoepite	0.82	0.53	6.7
Metaschoepite	1.62	1.05	13.
Na-boltwoodite	2.93	1.9	24.

Metaschoepite is the most likely reaction product; see discussion after Table 12.

The unzipping time duration is related to the velocity v_2 by Equation 33:

$$t = \frac{L}{v_2} \quad (\text{Eq. 33})$$

where L = length of fueled rod to be unzipped. A lower-bound value of a half-length of a rod is $L = 1.6$ meters (Section 4.1.1). Continuing the example calculation, the corresponding time durations of unzipping, if no other processes create additional breaches during this time, are given in Table 15.

Table 15. Unzipping Time Duration as a Function of Solid Product Type and Spent Fuel Alteration Rate

Product Solid	Fractional Increase in Specific Volume D	Alteration Rate S ($\mu\text{m/yr}$)	
		0.024	0.303
		Unzipping Time (yr)	
Dehydrated schoepite	0.82	3.0×10^6	2.4×10^5
Metaschoepite	1.62	1.5×10^6	1.2×10^5
Na-boltwoodite	2.93	8.4×10^5	6.7×10^4

The uncertainty in the more-realistic, experiment-based model is expressed as the uncertainty in the coefficient of Equation 32. The uncertainty is not available from data, since there is only one data point. The uncertainty can however be bounded by bounding models. The bounding model of Section 6.7.1 provides an upper bound on the values of the coefficient. A lower bound is provided by the following lower-bound conceptual model.

As a lower-bound alternate model, if the cladding unzipping progress does not enhance the surface area of spent fuel available for reaction, then the reaction front moves on a reaction front across the fuel rod, with a surface area πR^2 , and a velocity $v_2 = 1\text{S}$. Alternately, if there is no unzipping from the initial breach, then the reaction front could move down the interior of the rod on the reaction front across the fuel rod, with surface area πR^2 , with a velocity considerably below 1S , because of limitation by the necessity to remove uranium solutes by diffusion and because of surface products blocking the reaction surface. The limit $v_2 = 1\text{S}$ is a lower bound on the variation of the experimentally-based unzipping velocity.

6.7.3 Summary of Unzipping Velocity Model

The realistic-value-oriented model of Section 6.7.2 gives $v_2 = 26.9 D S$. With the predominant product species, metaschoepite, $D=1.62$. Then this gives a best estimate $v_2 = 43.6 S$, or with rounding, $v_2 = 40 S$. This model is best-estimate in the process factors of spent fuel behavior and Zircaloy behavior. It is on the conservative side in assuming that some crystallization pressure will develop inside but near the open breach, to advance the crack tip. It is also on the conservative side in assuming that the full circumference of the fuel pellet surface under the breach zone is exposed to further reaction.

An upper bound on this factor of proportion between v_2 and S is given by the bounding model with metaschoepite as the reaction product. This value of D with Equation 29 and Table 12 give $v_2 = 235 S$, or with rounding, $v_2 = 240 S$.

A lower bound on this factor of proportion between v_2 and S is given by the lower-bounding model $v_2 = 1S$; see Section 6.7.2.

The forward rate of spent fuel surface alteration rate, S , is considered to be a value given by an external model as a function of its relevant parameters. This spent fuel alteration model has been updated in a separate AMR (CRWMS M&O 2000b), based on additional data. The spent fuel alteration model's result value is an input to the present model. The spent fuel alteration rate is usually evaluated in units of $\text{mg}/\text{m}^2 \text{ day}$. Conversion factors for conversion to the present units of cm/yr are given in Section 4.1.7. As noted in Sec 4.1.7, the values of S can vary by over an order of magnitude between the 10th and 90th percentiles of the distribution of S . Hence, the value from the separate model for S is to be used, rather than using an average value of S .

In this application of the spent fuel surface forward alteration rate, S , a factor of six for increase in surface area due to grain boundary penetration by the reaction should be included (Gray and Wilson 1995, p. 4.2). A factor of increase in surface area due to cracks in the spent fuel pellet or due to surface roughness should not be used. The model envisages that such cracks have been filled in by precipitates before the stage when unzipping proceeds and new cylindrical surface area of pellets is again exposed to reaction. A reaction front on an initially undulating or rough surface will reduce the peaks faster than the valleys because of the peaks' higher surface area, and hence, tend toward a smooth front. The reaction area of interest in the unzipping model is under the cladding but near the breach. The hypothesized confining pressure, which is needed to advance the crack tip, will also favor a uniform reaction front in this region.

6.7.4 Variations on Some Concepts in the Models

Fraction of Circumference Participating in Reaction—One assumption is that the full circumference of the spent fuel pellet is participating in reactions, and generating solid products, at least for axial locations at distances of one to three cladding-tube radii and more. An alternate possibility is that the fraction of the circumference participating in the reactions and expansion is smaller than one. Part of the circumference is on the opposite side, possibly still protected from exposure to water by the adhering cladding tube. The fraction of spent fuel circumference exposed and participating might be smaller than assumed, perhaps by a factor of about two. If it is assumed that the products still form a cylindrical final shape, then this factor of two would

give a factor of two reduction in the rate of spreading of the open gap. This reduction would apply in both models, the bounding model and the single-experiment-based alternate model. The factor of two in exposed circumference would thus, give a factor of two reduction in the crack velocity v_2 for a given surface rate of alteration S . The reduction in exposed surface is possible, but for the reasons discussed in the beginning of Section 6.7 (see [Figure 14](#)), it is not included in the models. Omission of this consideration from the models is on the conservative side.

Quadratic outer surface for fuel reaction product volume—Another consideration refining an assumption applies to the assumption of a small depth of reacted spent fuel in the region near (within about four cladding-tube radii) the crack tip. In fact the outer radius of the initial plus product solids increases in a way that is at first nearly linear, but for larger advance of reaction is not linear but involves a square root. The following develops the more detailed radius shape and examines how much difference it makes as a function of axial distance from the crack tip.

As the crack tip advances with velocity v_2 ($\mu\text{m}/\text{yr}$) and the reaction front under an exposed surface moves inward from the initial radius R_0 with a surface rate S ($\mu\text{m}/\text{yr}$), the radial depth of the reaction front, $R_0 - R_{\text{inner}}$, is linear with distance x from the crack tip. R_{inner} reaches zero at an axial distance $X_{\text{max}} = R_0 \times \frac{v_2}{S}$. (See [Figure 22](#).) The outer radius of the initial plus reacted solid is:

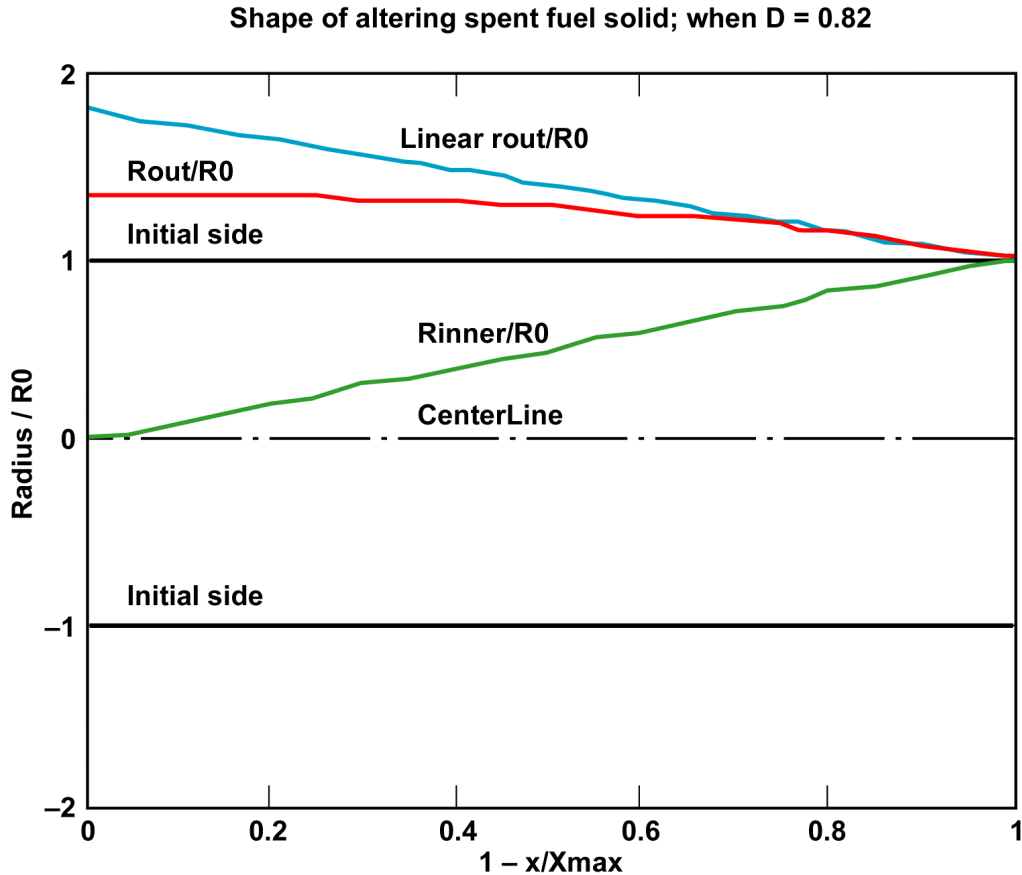
$$\frac{R_{\text{out}}}{R_0} = \sqrt{\left(1 + D - D\left(1 - \frac{x}{X_{\text{max}}}\right)^2\right)} \quad (\text{Eq. 34})$$

where

D = the fractional increase in specific volume for the product solid.

Thus, $\frac{R_{\text{out}}}{R_0}$ reaches a maximum value of $\sqrt{1+D}$ at X_{max} . Based on the slope near $x=0$, a linearized curve for R_{out}/R_0 reaches a maximum of $(1+D)$ at X_{max} . Thus, the increase in radius is less than linear. The ratio of the actual increase to the linearized increase is shown in [Figure 23](#).

As noted at the beginning of Section 6.7, the important axial region for crack expansion is the region from about one to four tube radii behind the crack tip, as based on [Figure 13](#). At lower temperatures, where the crack opening angle may be about a factor of two lower, the important region might extend from two to eight tube radii based on the opening width of the gap, or might still be up to four tube radii, based on the larger-scale structural distribution of force and the distance from the crack tip. For the present discussion, an interval from two to eight tube radii and its center location at five tube radii will be used. If the reacted solid cone is less expansive at greater distances from the crack tip, that is irrelevant because of the relatively larger value of (radius/distance) closer in.



NOTE: Assuming no axial displacement and assuming rotational symmetry of the solid is preserved.

Figure 22. Linearized and More Exact Outer Radius of Initial Solid plus Solid Product as a Function of Distance x from the Advancing Crack Tip

For a fixed axial distance, the largest deviation from the linear approximation of R_{out}/R_0 occurs when v_2/S is smallest, because then X_{max}/R_0 is smallest. For the example calculations earlier, this applies for the case within the alternate experiment-based model where dehydrated schoepite is the product. In that case, $X_{max}/R_0 = v_2/S = 22$. An axial distance x of five tube radii gives $x/X_{max} = 5/22 = 0.23$. At this distance, the actual increase in radius is 0.82 times the linearized increase in radius. Since in the models above the crack velocity v_2 is proportional to this increase in radius, then the linear model gives a v_2 , which is high by 22% compared to the more detailed square-root model.

For the product metaschoepite ($D = 1.62$), in the alternate model $X_{max}/R_0 = v_2/S = 44$. An axial distance x of five tube radii gives $x/X_{max} = 5/44 = 0.11$. At this distance, the actual increase in radius is 0.88 times the linearized increase in radius. Since in the models above the crack velocity v_2 is proportional to this increase in radius, then the linear model gives a v_2 , which is high by 14%.

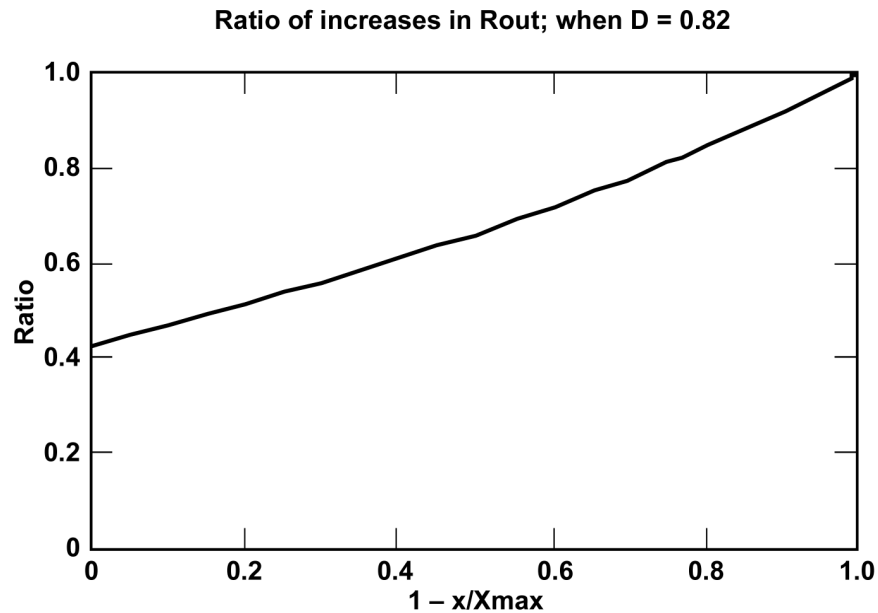


Figure 23. Ratio of Increases in the Outer Radius as a Function of Distance from the Advancing Crack Tip for the More Exact and the Linearized Models of the Outer Radius

For the bounding model, the ratio of v_2/S is a factor of 5.4 larger than the ratios given above for the experiment-based model. The deviations of the linear model from the square-root model are then only one-fifth as great as the 22% and 14% deviations just described for the experiment-based model.

Thus, in the cases examined the difference due to the more detailed square-root model of the radius is less than 25%. For more extreme values of other parameters, for example based on alternate interpretations of the photo angle and/or the ductility adjustment for temperature, the difference due to the radius model could be larger, but still less than a factor of two difference. Because the difference is modest, the use of this more detailed but more complex model of the outer radius is not recommended.

Omission of this consideration from the models is on the conservative side.

6.7.5 Degree of Confidence in the Model

The model of unzipping velocity is the principal output of the model development, intended for use in abstracted form as part of a system model of cladding degradation and consequent exposure of the contained spent fuel.

The best-estimate model is based partly on an experiment at higher temperature and partly on the conservative assumption that the water-based reaction and precipitation can cause clad unzipping. On the assumption that unzipping will occur, the approach used to relate the experiment at higher temperature to the rate of unzipping in the below-boiling range, using inelastic properties of the Zircaloy, is reasonable but has an undetermined uncertainty because of the small experimental data base. This uncertainty is bounded, however, using the upper and lower bounding models.

The upper bounding model of unzipping velocity, given the assumption that precipitation will drive unzipping, is based on well-known material properties and well-established concepts. It is based on elastic and yield stress properties of the Zircaloy, on reaction properties of the spent fuel, on kinematics of a steady-state crack extension, and on a conservative simplified geometry of the reaction/precipitation zone. The model does not use the inelastic properties of the Zircaloy. One quite conservative element in the model development is the selection of a location on the Zircaloy cladding tube for the evaluation of the lateral crack-opening motion $\partial u_3/\partial t$ for comparison to $\partial u_3/\partial x_2$ at a point near the crack tip (see Sec. 6.7.1). This conservative element should more than counterbalance the relatively small material-property uncertainties and round-off uncertainties in the model development. Conceptually the model uses elastic properties and does not use inelastic properties of Zircaloy; this feature is conservative.

The best-estimate model provides support for the bounding model, since the best-estimate value of unzipping velocity is a factor of six lower than that in the bounding model. The best-estimate model is based to an extent on different concepts, e.g., crack opening angle related to inelastic properties of the material. Two independent models provide more confidence than one model alone.

Experiments in progress for the YMP (see [Attachment I](#)), using fragmented spent fuel inside a cladding section, may provide partial validation of the model.

6.8 EXPOSED SPENT FUEL AREA AS A FUNCTION OF TIME

A crack unzipping at velocity v_2 exposes the outer surface of the additional spent fuel to alteration. The length of the initial breach is $2L_0$. The length of the breach on one side of the center of the breach is L_0 plus the time integral of the unzipping rate. The unzipping rate may depend on time, primarily through the dependence of the spent fuel alteration rate on the local environment. Both sides of the extending breach are treated the same, except that each side may have a different stopping length.

The initial breach size (Section 4.1.4) is taken to be the same as the average cladding thickness (Section 4.1.1) or 0.070 cm. The active half-length L_{total} has a median value of 72 inches or 180 cm. This is the median value from the fueled length in [Table 1](#) and is appropriate for application to the exposed spent fuel area as a function of time.

The amount of spent fuel geometric surface being reacted at any time, on one side of the breach, is a segment of a cone of a base with radius of the unreacted core of the spent fuel pellet at the start of breach extension (initial radius adjusted for reaction during the period when the fuel-cladding gap was present), and a cone height equal to v_2/S times that radius, where S is the spent fuel forward reaction rate. The base of the cone is progressing at the rate just mentioned, v_2 (see Section 6.7). The rest of the cone is following at the same speed. When the length unzipped is greater than the full cone height, then the full cone shape of reacting surface is present. Behind the apex of the cone, fully reacted spent fuel is to be found. When the unzipped length reaches the full length, the remaining cone shape keeps moving into the end at the same speed v_2 . The cone aspect stays the same, even if v_2 varies with time, because progress both of unzipping and of reaction front depend on the spent fuel reaction rate.

Figure 24 shows how unzipping allows the reaction to occur at further lengths as the unzipping progresses, and how the reaction progresses toward the center of the pellets after it is possible from the outside. The zone between “breach center” and “ L_{total} ” is the actual spent fuel rod section. The zones before and after that are virtual zones used for following the movement of the conical shape.

In parameters and equations:

L_0 is the initial breach length

Unzipped progress is $L_1(t) = \text{integral of } v_2(t) \, dt$

Total section length (on one side) is $L(t) = L_0 + L_1(t)$

Total length available is L_{total} (fueled length on one side of the breach center)

R_1 is the radius of unreacted spent fuel at the time when the fuel-cladding gap is closed, from Section 6.6. (Recall that this radius could in actuality be closer to the initial pellet radius, but a choice was made in Section 6.6 to include as much reaction as possible in the first time phase.) Thus, $R_1^2 = R_f^2(1 - R_{\text{Altered}})$ where R_f is the initial fuel radius and R_{Altered} is a value selected from the distribution specified in Section 6.6.

Cone full height in principle is

$$H = R_1 \left(\frac{v_2}{S} \right) / \sqrt{1 + \left(\frac{S}{v_2} \right)^2}$$

Here the small-angle adjustment to v_2 is included so that the cone area will be correct.

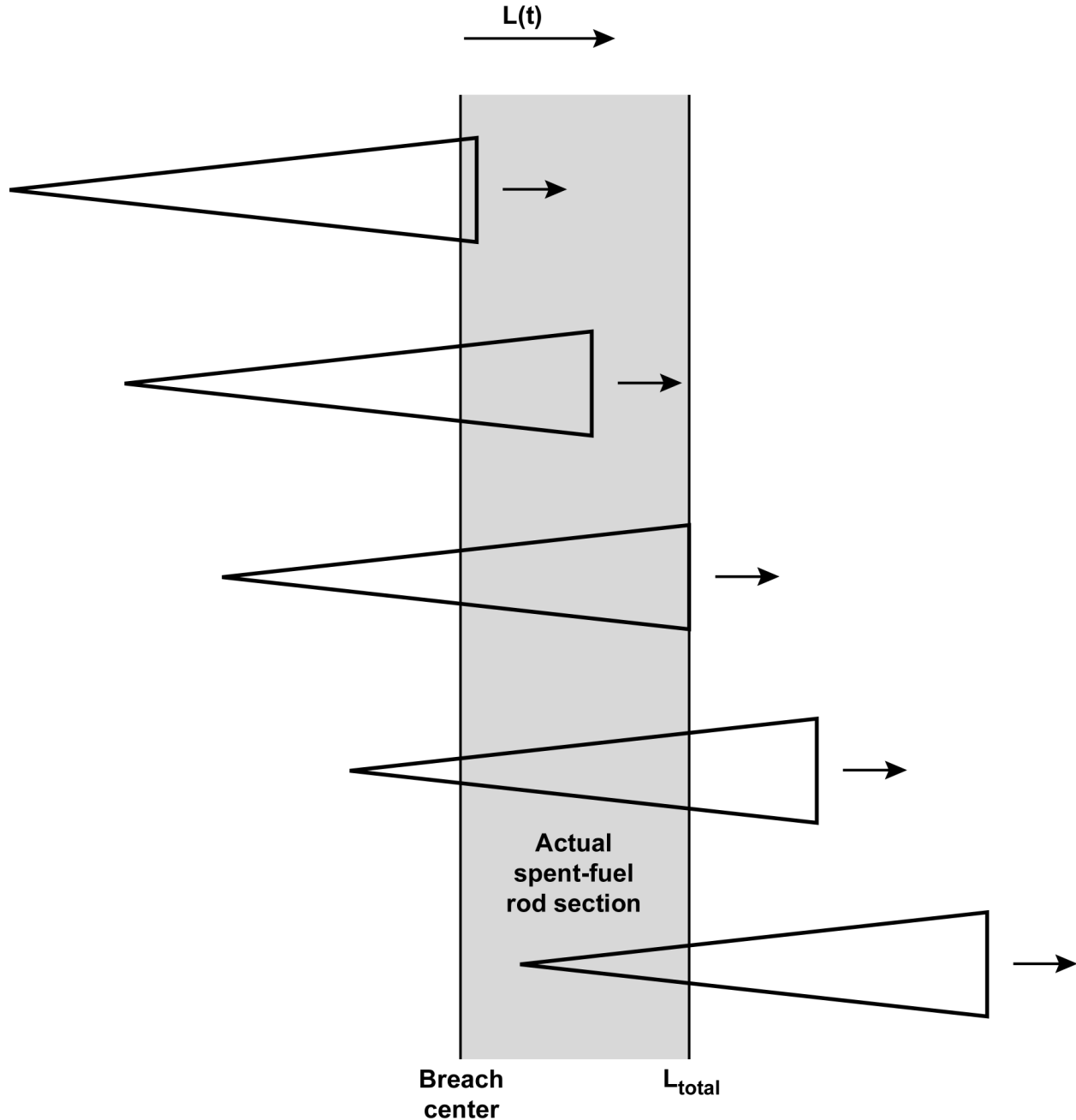


Figure 24. Location of Active Spent Fuel Reaction Surface as a Function of Unzipping Length, which is a Function of Time.

In the example calculation of Section 6.7, v_2/S came to 145D. For a product of dehydrated schoepite or metaschoepite, $D = 0.82$ or 1.62 respectively. Then, this example gives $H/R_1 = v_2/S = 119$ or 235 respectively. Further, typical values are initial radius $R_f = 0.48$ cm (Section 4.1.1) and ratio $R_{Altered} = 0.04$. Then, $R_1 = 0.47$ cm, and the example gives $H = 56$ cm or 110 cm respectively. The time for the cone development to grow to the full cone is H/L_{total} times the full

unzipping time, which was shown in Table 13 to be a long time. The numerical example values are intended just to give an indication of the possible size of the effects.

The radii of the upper and lower bounding surfaces of the (sometimes truncated) cone are evaluated, first for time segments when $L(t) \leq L_{\text{total}}$ and when $L(t) > L_{\text{total}}$. The radii for the combined total time period are evaluated in one algorithm.

First, when $L(t) \leq L_{\text{total}}$:

At time t , the truncated cone has a base of radius $R_B = R_1$. The cone has an upper surface with a radius of:

$$R_T(t) = \max\left(R_1 \times \frac{(H - L(t))}{H}, 0\right)$$

That is, when $L(t) > H$ there is a full cone, and $R_T = 0$.

Next, when $L(t) > L_{\text{total}}$, the base radius R_B starts shrinking. The base of the (truncated or untruncated) cone is of radius:

$$R_B(t) = \max\left(R_1 \times \frac{H - (L(t) - L_{\text{total}})}{H}, 0\right)$$

The trailing end of the cone has a radius $R_T(t)$, calculated as above.

For the combined total time period,

$$R_B(t) = \max\left(R_1 \times \frac{H - \max(0, (L(t) - L_{\text{total}}))}{H}, 0\right) \quad (\text{Eq. 35})$$

$$R_T(t) = \max\left(R_1 \times \frac{H - L(t)}{H}, 0\right). \quad (\text{Eq. 36})$$

The curved surface area of a full cone of height H and base radius R_1 is $\pi R_1 \sqrt{H^2 + R_1^2}$. Then the area of the truncated cone, i.e., the fuel reaction area, is

$$A(t) = \pi (R_B(t)^2 - R_T(t)^2) \frac{V_2}{S} \quad (\text{Eq. 37})$$

ending when $R_B(t)$ reaches zero.

The maximum plateau value, attained while a full cone is developed, is:

$$A_{\max}(t) = \pi \frac{V_2}{S} R_1^2 \quad (\text{Eq. 38})$$

A simpler and relatively conservative approach to the area $A(t)$ is to ramp up to the plateau at a linear ramp:

$$A_{\text{ramp}}(t) = 2 \pi R_1 L(t) \quad (\text{Eq. 39})$$

until it reaches the plateau value, then maintain the plateau value until all the spent fuel has reacted. The linearized ramp takes half as long to reach the plateau value, or $(0.5 H/L_{\text{total}})$ times the full unzipping time, as compared to the cone ramp (which depends on the square of the changing radius R_T in Equation 37).

6.9 MODEL VALIDATION

Wet unzipping, and even its initiation, are so slow that this process has not yet been observed. Therefore, data are not available to validate the model. The alternative approach of reviewing model calibration parameters for reasonableness will be used instead.

The model described in this report treats four aspects of unzipping: the quantity of fuel that reacts before unzipping begins, the time necessary for that reaction (the gap-filling period), the unzipping velocity, and the reacting spent fuel surface area during unzipping. The current level of validation for each of these aspects is described in the following subsections.

6.9.1 Quantity of Fuel Reacted Before Unzipping Begins and Gap-Filling Time

Calculation of the fuel mass reacted is based on the principle of conservation of matter. Spent fuel reacts with water and oxygen to produce reaction products that are larger than the spent fuel consumed in producing those products. Because of the simple basis of the model, the only parameters that affect the results are the initial void volume and the molar volumes of the reactants and products. The void volume is calculated from fuel design parameters, so this parameter is well known. The molar volumes are TBV, but they are based on straightforward crystallographic measurements. Uncertainties in molar volumes are estimated to be less than 10%, so the effect of the TBV information is not expected to be significant. Therefore the parameters are all reasonable and predictions of the fuel mass reacted may be used in performance assessment without additional validation.

Calculation of the time necessary to fill the fuel-cladding gap builds on the calculation of the fuel mass reacted. In qualitative terms, the volume expansion mentioned above and the reaction rate can be combined to yield a rate of expansion, and the time to fill the gap can be calculated from the gap width and the rate of expansion. The reaction rate is subject to substantial uncertainty. As a result of the uncertainty, it is recommended in Section 7 that the time should be neglected in total system performance assessments. Since this approach is clearly bounding, it may be used in performance assessment without additional validation.

6.9.2 Unzipping Velocity

Three approaches to modeling the unzipping velocity were considered: upper bound, realistic, and lower bound. The results of these models are briefly summarized in Section 6.7.3.

In all three approaches, the unzipping velocity is proportional to the spent fuel reaction rate, which was studied in a separate AMR (CRWMS M&O 2000b). The spent fuel reaction rate has substantial uncertainty, and this uncertainty must be treated as part of total system performance assessment. This AMR avoids the question of uncertainty in the spent fuel reaction rate by expressing the unzipping velocity as a multiple of that rate.

The variations in the results between the three different models show that there is substantial uncertainty in the unzipping velocity. To handle this uncertainty Section 7 recommends that total system performance assessments should use of a distribution of velocities. [Attachment I](#) describes ongoing work to provide additional validation.

Upper bound—In the upper bound approach, fracture mechanics and mechanical properties of Zircaloy were used to predict the unzipping velocity. The parameters that affect unzipping velocity are the ratio of the shear strength and shear modulus of Zircaloy, the molar volumes of the reactant and product (UO_2 and metaschoepite, respectively), and the spent fuel reaction rate.

The ratio of the shear strength and shear modulus of Zircaloy is subject to some uncertainty, notably because of changes in strength as a result of irradiation. However, shear strength is proportional to yield strength, and inspection of [Figure 3](#) shows that yield strengths for irradiated cladding are bunched at the top of the figure. From [Figure 3](#), it might be estimated that, for a given temperature, yield strengths have an uncertainty of 10% or less. The shear modulus is also proportional to Young's modulus. Section 4.1.2.1 discusses variability in Young's modulus and gives an uncertainty of about 10%. Some of these data are TBV, but the general agreement among various sources suggests that the effect of the TBV data is small.

Uncertainties in molar volumes are discussed in Section 6.9.1. These uncertainties must be added to those in the ratio of the shear strength to the shear modulus. However, it should be noted that model uses a bounding approach in that no credit is taken for plasticity of the Zircaloy. As a result, the upper bound approach is expected to provide an upper bound on the unzipping velocity, regardless of the uncertainties in the parameters.

Realistic—In the realistic approach, the parameters that affect the unzipping velocity are the split angle, the molar volumes of the reactant and product (UO_2 and metaschoepite, respectively), and the spent fuel reaction rate.

The split angle is estimated from a photograph of a fuel rod undergoing dry unzipping at high temperature, with a correction for decreasing ductility at decreasing temperature. Uncertainty in the split angle was estimated at 10% in Section 6.7.2. The correction for decreasing ductility is rough and qualitative; it might be uncertain by a factor of two. This is a substantial amount of uncertainty, but, since the results for the realistic approach fall between those for the upper bound and lower bound approaches, the use of a distribution in total system performance assessment will also show a large uncertainty.

Lower bound—In the lower bound approach, the unzipping velocity is equal to the spent fuel reaction rate. The spent fuel reaction rate is discussed above. No other parameters affect the unzipping rate in this approach.

6.9.3 Reacting Spent Fuel Surface Area

Three methods have been described for calculation of the exposed spent fuel area: direct calculation of the cone area, a ramp-and-plateau approximation, and treating all fuel behind the tip of the breach as reacted. Each of these requires separate consideration.

With direct calculation of the cone area, the area is calculated by simple geometry from the cone apex angle. The cone apex angle, in turn, results from the previous calculation of unzipping velocity. Therefore, uncertainties in unzipping velocity will be directly reflected in uncertainties in the exposed spent fuel area. Specifically, uncertainties in v_2/S will affect the cone area as indicated by Equation 35. As is discussed in Section 6.7.1, there is substantial uncertainty in v_2/S . If the method of direct calculation of the cone area is used, total system performance assessments must consider this uncertainty and its correlation with unzipping speed. Further validation of the model must be deferred to the total system performance assessment.

As regards model validation, the ramp-and-plateau approximation is very similar to the method of direct calculation of the cone area. The only difference is that, during the period when the cone area is changing, the area is approximated by a linear ramp that bounds the actual cone area. Since these two methods are so similar, the discussion of uncertainties and validation in the previous paragraph apply here as well.

If all fuel behind the tip of the breach is treated as reacted, the question of exposed spent fuel area is effectively sidestepped. If this method is used, the total system performance assessment would not calculate the exposed surface area; instead, it would go directly from the length of the breach to the fraction of fuel reacted. Since the exposed surface area would not be considered, there are no parameters that affect the exposed surface area. This approach gives an upper bound on the fraction of fuel reacted. Since this approach is bounding, it may be used in performance assessment without additional validation.

7. CONCLUSIONS

A model has been developed for wet unzipping of commercial spent nuclear fuel. The scope of the model begins at a time when there is a small breach in the cladding tube of a spent fuel rod, and there is liquid water or water vapor present, and the temperature is below 100°C. The model describes four aspects of unzipping: the quantity of fuel that reacts before unzipping begins, the time necessary for that reaction (the gap-filling period), the unzipping velocity, and the reacting spent fuel surface area during unzipping. Specific recommendations for treating each of these aspects are given below.

The models and associated parameter distributions discussed below are to be used as nominal case models. Some assumptions and parameter distributions are made on a best-estimate basis, with quantitative estimates of the uncertainty distributions. Some assumptions are conservative in order to bound uncertainties. Therefore, the models are more likely to overestimate what might actually occur.

This document may be affected by technical product input information that requires confirmation. Any changes to the document that may occur as a result of completing the confirmation activities will be reflected in subsequent revisions. The status of the input information quality may be confirmed by review of the Document Input Reference System database.

Quantity of Fuel Reacted during the First Time Period—Unzipping will not begin immediately after a breached fuel rod is exposed to moisture. Instead, the fuel-cladding gap and existing cracks will fill with solid reaction products. Up to a few percent of the spent fuel matrix mass may be reacted during this period. For the extent of the first time period while the gap is filling with reaction products, the total fraction of the spent fuel matrix solid that is altered by reaction is given by Equation 13:

$$R_{\text{Altered}} = (1/D) R_{\text{Void}}$$

where

R_{Void} = a bound on the void volume within the spent fuel rod's active length; the recommended value is $0.045 \pm 10\%$ (dimensionless) for a representative range of ten fuel rod designs; and

D = the fractional increase in specific volume in going from UO_2 to its solid reaction product. Values of D for the possible reaction products, and corresponding values of R_{Altered} , are given in [Table 10](#).

Metaschoepite is likely to be the most frequent reaction product during the first time phase. Dehydrated schoepite is likely to be the second most frequent product. Na-boltwoodite is likely to be infrequent because it requires silica, which is limited in the groundwater. The recommended distribution of the values of the fraction of the spent fuel matrix solid that is altered by reaction during this period is a triangular distribution extending between the values of 0.028 and 0.055 (dimensionless fractions), with maximum probability density at the value 0.028, and decreasing linearly to zero probability density at the upper end of the range, 0.055.

Predictions of the quantity of fuel reacted are affected by the molar volume of metaschoepite, which is TBV. The uncertainty in this molar volume and its effect on the quantity of fuel reacted are discussed in Section 6.9.1.

Time Duration of the Gap-Filling Period—The time for this period is given by Equation 14. It depends on the gap size, and inversely on the spent fuel reaction rate and the fractional increase in specific volume for the solid reaction product. The times for possible values of the parameters range from extremely short up to several thousand years. These times are relatively short on overall repository process time scales, so it is recommended that they be neglected for total system performance assessment, i.e., in association with the quantity of radionuclides released during this period, and in the starting time for the unzipping process.

Unzipping Velocity—As noted in the introduction to this section, an existing breach may possibly be extended or unzipped in the rod's axial direction by the reaction products.

Three approaches to modeling the unzipping velocity were considered: upper bound, realistic, and lower bound. To account for uncertainties in unzipping behavior, it is recommended that the results for all three approaches be used for total system performance assessment, that is, the results should be used to specify the maximum, mode, and minimum for a distribution of unzipping rates.

An upper bound model for the unzipping velocity v_2 is developed in Section 6.7 and the result is given by the Equation 29

$$v_2 = \pi \{ \mu / \sigma_{\text{yield}} \} D S$$

where

- μ = the elastic shear modulus of the irradiated Zircaloy tube material
- σ_{yield} = the 0.2% uniaxial yield stress of the irradiated Zircaloy tube material
- D = the fractional increase in specific volume for the solid reaction product
- S = the spent fuel surface forward alteration rate.

The equations in this section apply if the same units are used for v_2 and S .

For repository temperatures during the long period while the unzipping process advances, the value of D for metaschoepite should be used; see discussion in Section 6.7.1 after [Table 12](#). Then the bounding model for the unzipping velocity is

$$v_2 = 240 S$$

An alternate, more realistic, model of the unzipping velocity was developed, based on one experimental point of dry oxidation-driven unzipping at 360°C. This alternate model gives an unzipping velocity of

$$v_2 = 40 S$$

for environments within the temperature range of 18-100°C. The uncertainty in this more realistic model is not available from direct data but is bounded by the upper bounding model $v_2 = 240 \text{ S}$ presented above, and a lower bounding model of (Section 6.7.2)

$$v_2 = 1 \text{ S}$$

The forward rate of spent fuel surface alteration rate, S , is considered to be a value given by an external model as a function of its relevant parameters. This spent fuel alteration model is documented in a separate AMR (CRWMS M&O 2000b), based on additional data. The spent fuel alteration model's result value should be used as an input to the present model. The spent fuel alteration rate is usually evaluated in units of $\text{mg/m}^2\cdot\text{day}$. Before being used with the equations in this section, the alteration rate should be converted into velocity units (e.g., $\mu\text{m/yr}$), following the treatment in Section 4.1.7. As noted in Section 4.1.7, the values of S can vary by over an order of magnitude between the 10th and 90th percentiles of the distribution of S . Hence, the value from the separate model for S is to be used, rather than using an average value of S .

In this application of the spent fuel surface forward alteration rate, S , a factor of six for increase in surface area due to grain boundary penetration by the reaction should be included; see Section 6.7.3. A factor of increase in surface area due to cracks in the spent fuel pellet or due to surface roughness should not be used; see Section 6.7.3.

Predictions of the unzipping velocity are affected by Young's modulus for Zircaloy, which is TBV. The uncertainty in Young's modulus and its effect on the unzipping velocity are discussed in Section 6.9.2.

Reacting Spent Fuel Surface Area as a Function of Time—A model for reacting surface area was developed, plus two simplified versions of this model. Using a more simplified version will increase the predicted release rate but decrease the computational effort. Therefore, total system performance assessments should use the simplest version that provides acceptable results.

The reacting spent fuel surface area is found behind the advancing breach extension location. It is assumed that the fuel cylindrical outer surface under the breach zone is exposed to further reaction, and that an axial position becomes exposed to reaction when the crack tip advances to that axial extent. Within this model framework, the surface of the reaction front at any given time is the curved surface of a truncated cone extending in the axial direction, one cone for each of the two directions from the initial crack location. The simple cone shape holds true, within the logic of this model, even if the spent fuel alteration rate varies significantly over time, as a function of its environmental parameters. Equations for the reacting spent fuel surface area as a function of time are given in Equations 35 to 37 of Section 6.8.

A simplified function of area versus time is recommended, because the cone aspect ratio, height/radius, is very large for the likely parameter ranges in the repository application. The simplified function is a linear ramp and then a plateau value. Equations are given in Equations 38 and 39 of Section 6.8. This ramp-and-plateau set of equations for the area is slightly more conservative than the cone-area equation, which gives the same plateau value.

An even more simplified and more conservative approach is to assume that the spent fuel is reacted once the unzipping breach has reached the axial location of that spent fuel. Under this conservative approach the partial delay of the slowly advancing reaction front behind the crack tip is not used.

8. INPUTS AND REFERENCES

8.1 DOCUMENTS CITED

ASM International 1967. "Zircaloy-2, Nuclear Reactor Alloy, Filing Code:Zr-3 Zirconium Alloy." *Alloy Digest*, (July), . Materials Park, Ohio: ASM International. TIC: 239929.

Burns, P.C. 1998. "The Structure of Boltwoodite and Implications of Solid Solution Toward Sodium Boltwoodite." *The Canadian Mineralogist*, 36, 1069-1075. Ottawa, Ontario, Canada: Mineralogical Association of Canada. TIC: 246038.

Chen, F.; Ewing R. C.; and Clark S. B. 1999. "The Gibbs Free Energies and Enthalpies of Formation of U6+ Phases: An Empirical Method of Prediction." *American Mineralogist*, 84, (4), 650-664. Washington, D.C.: American Mineralogist. TIC: 245800.

Cherepanov, G.P. 1979. *Mechanics of Brittle Fracture*. 200-203. New York, New York: McGraw-Hill. On Order Library Tracking Number-L1417

Correns, C.W. 1949. "Growth and Dissolution of Crystals Under Linear Pressure." *Discussions of the Faraday Society, Crystal Growth*, 5, 267-271. London, England: Gurney and Jackson. TIC: 245680.

CRWMS M&O 1999a. *Classification of the MGR Uncanistered Spent Nuclear Fuel Disposal Container System*. ANL-UDC-SE-000001 REV 00. Las Vegas, Nevada: CRWMS M&O. ACC: MOL.19990928.0216.

CRWMS M&O 1999b. *1101213FM3 Waste Form Analyses & Models - PMR*. Activity Evaluation, December 14, 1999. Las Vegas, Nevada: CRWMS M&O. ACC: MOL.19991217.0048.

CRWMS M&O 2000a. *Waste Package Materials Department Analysis and Modeling Reports Supporting the Waste Form PMR*. TDP-EBS-MD-000005 REV 01. Las Vegas, Nevada: CRWMS M&O. ACC: MOL.20000202.0173.

CRWMS M&O 2000b. *CSNF Waste Form Degradation: Summary Abstraction*. ANL-EBS-MD-000015 REV 00. Las Vegas, Nevada: CRWMS M&O. ACC: MOL.20000121.0161.

Cunnane, J. 2000. Clad Degradation-Wet Unzipping: Release Rates from Breached Cladding and Potential Unzipping Velocity. Scientific Notebook 1563. ACC: MOL.20000301.1129.

DOE (U.S. Department of Energy) 1998. *Total System Performance Assessment*. Volume 3 of *Viability Assessment of a Repository at Yucca Mountain*. DOE/RW-0508. Washington, D.C.: U.S. Department of Energy, Office of Civilian Radioactive Waste Management. ACC: MOL.19981007.0030.

DOE (U.S. Department of Energy) 2000. *Quality Assurance Requirements and Description*. DOE/RW-0333P, Rev. 9. Washington, D.C.: U.S. Department of Energy, Office of Civilian Radioactive Waste Management. ACC: MOL.19991028.0012.

Einziger, R.E. and Strain, R.V. 1986. "Behavior of Breached Pressurized Water Reactor Spent-Fuel Rods in an Air Atmosphere Between 250 and 360°C." *Nuclear Technology*, 75, (1), 82-95. Hinsdale, Illinois: American Nuclear Society. TIC: 238325.

Finch, R. 1997. Argonne National Laboratory, Chemical Technology Division Logbook. Scientific Notebook 1171. ACC: MOL.19981109.0144.

Finch, R.J.; Buck, E.C.; Finn, P.A.; and Bates, J.K. 1999. "Oxidative Corrosion of Spent UO₂ Fuel in Vapor and Dripping Groundwater at 90°C." *Scientific Basis for Nuclear Waste Management XXII, Symposium held November 30-December 4, 1998, Boston, Massachusetts, U.S.A.* Wronkiewicz, D.J. and Lee, J.H., eds. 556, 431-438. Warrendale, Pennsylvania: Materials Research Society. TIC: 246426.

Finch, R.J.; Hawthorne, F.C.; and Ewing, R.C. 1998. "Structural Relations Among Schoepite, Metaschoepite, and Dehydrated Schoepite." *Canadian Mineralogist*, 36, 831-845. Ontario, Canada: Mineralogical Association of Canada. TIC: 246161.

Finch, R.J.; Miller, M.L.; and Ewing, R.C. 1992. "Weathering of Natural Uranyl Oxide Hydrates: Schoepite Polytypes and Dehydration Effects." *Radiochimica Acta*, 58/59, 433-443. München, Germany: R. Oldenbourg Verlag. TIC: 238032.

Glasstone, S. and Sesonske, A. 1981. *Nuclear Reactor Engineering*. Third Edition. Malabar, Florida: Krieger Publishing Company. TIC: 239377.

Gray, W.J. and Wilson, C.N. 1995. *Spent Fuel Dissolution Studies, FY 1991-1994*. PNL-10540. Richland, Washington: Pacific Northwest Laboratory. ACC: MOL.19980625.0338.

Grenthe, I.; Fuger, J.; Konings, R.J.M.; Lemire, R.J.; Muller, A.B.; Nguyen-Trung, C.; and Wanner, H. 1992. *Chemical Thermodynamics of Uranium*. Volume 1 of *Chemical Thermodynamics*. Wanner, H. and Forest, I., eds. Amsterdam, The Netherlands: North-Holland Publishing Company. TIC: 224074.

Hellen, T.K. 1984. "Methods for Computing Contour Integrals." *Post-Yield Fracture Mechanics*. Latzko, D.G.H.; Turner, C.E.; Landes, J.D.; McCabe, D.E. and Hellen, T.K., eds. 289-292. New York, New York: Elsevier Applied Science Publishers. TIC: 247018.

Huang, F.H. 1995. *Fracture Properties of Irradiated Alloys*. 418 p. Richland, Washington: Avante Press. TIC: 224548.

Kanninen, M.F. and Popelar, C.H. 1985. *Advanced Fracture Mechanics*. Pages 122-125, and 138-146. New York, New York: Oxford University Press. TIC: 247002.

Lide, D.R., ed. 1995. *CRC Handbook of Chemistry and Physics*. 76th Edition. Boca Raton, Florida: CRC Press. TIC: 216194.

Lowry, L.M.; Markworth, A.J.; Perrin, J.S.; and Landow, M.P. 1981. *Evaluating Strength and Ductility of Irradiated Zircaloy, Task 5. Experimental Data Final Report*. NUREG/CR-1729, Volume 1. Washington, D.C.: U.S. Nuclear Regulatory Commission. TIC: 238074.

McEachern, R.J. and Taylor, P. 1997. *A Review of the Oxidation of Uranium Dioxide at Temperatures Below 400°C*. AECL-11335. Pinawa, Manitoba, Canada: Atomic Energy of Canada Limited. TIC: 232575.

Pettersson, K.; Vesterlund, G.; and Andersson, T. 1979. "Effect of Irradiation on the Strength, Ductility, and Defect Sensitivity of Fully Recrystallized Zircaloy Tube." *Zirconium in the Nuclear Industry, Proceedings of the Fourth International Conference*. ASTM STP 681, 155-173. Philadelphia, Pennsylvania: American Society for Testing and Materials. On Order Library Tracking Number-L1174

Ping, X. and Beaudoin, J.J. 1992. "Mechanism of Sulphate Expansion, I. Thermodynamic Principle of Crystallization Pressure." *Cement and Concrete Research*, 22, (4), 631-640. Elmsford, New York: Pergamon Press. TIC: 245678.

Shoesmith, D.W. 1999. *Fuel Corrosion Processes Under Waste Disposal Conditions*. AECL-12034. Pinawa, Manitoba, Canada: Whiteshell Laboratories. TIC: 246006.

Sokolnikoff, I.S. 1956. *Mathematical Theory of Elasticity*. 2nd edition. New York, New York: McGraw-Hill. TIC: 240386.

Stout, R.B. 1998. *Unsaturated Dissolution Tests of Spent Fuel and UO₂*. Activity Plan D-20-43 REV 01. Livermore, California: Lawrence Livermore National Laboratory. ACC: MOL.19980803.0086.

Stout, R.B. and Leider, H.R. 1998. *Waste Form Characteristics Report, Revision 1*. UCRL-ID-108314, Version 1.3. Livermore, California: Lawrence Livermore National Laboratory. ACC: MOL.19981214.0043.

Sunder, S. and Miller, N.H. 1996. "Oxidation of CANDU Uranium Oxide Fuel by Air in Gamma Radiation at 150 degrees C." *Journal of Nuclear Materials*, 231, 121-131. Amsterdam, The Netherlands: Elsevier Science. TIC: 246429.

Taylor, P.; Lemire, R.J.; and Wood, D.D. 1993. "The Influence of Moisture on Air Oxidation of UO₂: Calculations and Observations." *Nuclear Technology*, 104, 164-170. Hinsdale, Illinois: American Nuclear Society. TIC: 246460.

Walker, T.J. and Kass, J.N. 1974. *Variation of Zircaloy Fracture Toughness in Irradiation*. Zirconium in Nuclear Applications, A Symposium, 21-24 August 1973, Portland, Oregon. ASTM Special Technical Publication 551, 328-354. Philadelphia, Pennsylvania: American Society for Testing and Materials. TIC: 247106.

Webster, R.T. 1990. "Zirconium and Hafnium." Volume 2 of *Metals Handbook*. 10th Edition. Pages 661-669. Materials Park, Ohio: ASM International. TIC: 241059.

Wilson, C.N. 1985. *Results from NNWSI Series 1 Spent Fuel Leach Tests*. HEDL-TME-84-30. Richland, Washington: Hanford Engineering Development Laboratory. TIC: 210347.

Wilson, C.N. 1990. *Results from NNWSI Series 3 Spent Fuel Dissolution Tests*. PNL-7170. Richland, Washington: Pacific Northwest Laboratory. ACC: NNA.19900329.0142.

8.2 CODES, STANDARDS, REGULATIONS, AND PROCEDURES

AP-3.10Q, Rev. 2, ICN 0. *Analyses and Models*. Washington, D.C.: U.S. Department of Energy, Office of Civilian Radioactive Waste Management. ACC: MOL.20000217.0246

AP-SI.1Q, Rev. 2, ICN 4. *Software Management*. Washington, D.C.: U.S. Department of Energy, Office of Civilian Radioactive Waste Management. ACC: MOL.20000223.0508.

ASTM B 811-90. 1991. *Standard Specification for Wrought Zirconium Alloy Seamless Tubes for Nuclear Reactor Fuel Cladding*. Philadelphia, Pennsylvania: American Society for Testing and Materials. TIC: 239780.

QAP-2-0, Rev. 5, ICN 1. *Conduct of Activities*. Las Vegas, Nevada: CRWMS M&O. ACC: MOL.19991109.0221.

QAP-2-3, Rev. 10. *Classification of Permanent Items*. Las Vegas, Nevada: CRWMS M&O. ACC: MOL.19990316.0006.

8.3 SOURCE DATA

LL990908751021.088. Clad Degradation Wet Unzipping: Release Rates from Breached Cladding and Potential Unzipping Velocity. Submittal date: 09/23/1999.

ATTACHMENT I

SUMMARY OF ONGOING TESTS ON FUEL IN CLADDING UNDER VAPOR AND DRIP CONDITIONS

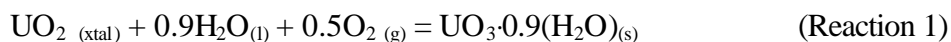
ATTACHMENT I, PART A
SUMMARY OF THE CLAD FUEL VAPOR TESTS

CLAD FUEL VAPOR TESTS

During the post-containment period, which is 300-1000+ years after repository closure, the spent fuel could be exposed to water condensation potentially causing the cladding to unzip due to expansive forces from the formation of secondary alteration products. Tests with spent nuclear fuels are being performed at Argonne National Laboratory for the YMP to simulate conditions that may cause cladding failure and to monitor the release of radionuclides from the spent fuel in which cladding has been compromised. The information obtained from these tests can be used to determine the average reaction rate of the fuel and the average transport rate of reaction products and groundwater components from the spent fuel rod under controlled experimental conditions. Other information needed is the importance of an increase in spent fuel volume as a factor in cladding failure, the mode of radionuclide release as the fuel corrodes, and the difference in reaction of different fuels under simulated repository conditions.

The tests described below were designed to evaluate the importance of different parameters in defining the bounds of the radionuclide source term in an unsaturated repository. Three types of complementary tests are described in order to obtain the information necessary to determine the reaction rate of the spent fuel matrix, the transport rate of the different radionuclides, and other information required to support development of a spent fuel release model.

The chemical reaction relevant to this system is



See main report Section 4.1.5. This reaction is the oxidative dissolution of crystalline uranium dioxide to form dehydrated schoepite.

The following calculation is meant to provide a qualitative estimate of the extent of fuel reaction required for cladding failure to occur by the above reaction. The calculation assumes that the corrosion products are confined and that the forces are limited to producing circumferential strain. Porosity is not considered and ideal packing is assumed. The calculation also assumes that the amount of reactants is not limited. After some alteration of the fuel and precipitation of the secondary solid product, the volume is increased (see Section 4.1.5). A circumferential increase of 2% is taken as an approximate measure of a threshold for cladding failure (see Sec. 6.4). This corresponds to a volume increase of 4% in a cylinder with a fixed height. This in turn corresponds to ~5% of the fuel altered by reaction 1. For finely divided spent fuel with large surface area, and based on the rate of spent fuel corrosion in unsaturated tests on fuel fragments, these test results indicate that measurable strain should be observable in long-term laboratory experiments. Although the formation of alteration phases is thermodynamically favored and results in formation of alteration products with a larger specific volume than the fuel there may not be a kinetically suitable mechanism for the reaction to proceed if the volume expansion shuts off the water supply. The purpose of this task is to investigate these mechanisms.

EXPERIMENTAL

The Clad Fuel Vapor Tests are designed to react clad spent fuel with water vapor. The tests are performed at 175°C to accelerate the oxidative dissolution so that mechanisms that can potentially lead to cladding failure or prevent cladding failure can be observed in a reasonable time frame. The test samples are summarized in [Table I-A1](#).

Table I-A1. Samples Used in Clad Fuel Vapor Tests

Specimen Identification	Fuel Type	Clad Segment Mass (g)	Initial Clad Segment and Swagelok Fittings Mass (g)
SFV-1	ATM-103	67.95	140.40
SFV-2	ATM-103	80.52	152.87
SFV-3	ATM-103	77.54	149.89
SFV-4	ATM-103	80.31	152.65

The following items broadly summarize the Clad Fuel Vapor Tests after a year of operation:

- Samples are nominally 3.5 in. clad fuel segments of ATM-103.
- Samples are capped at each end with Ti Swagelok caps to confine the fuel and reaction products.
- Each end cap and the cladding of each sample have been given 2-mm perforations to facilitate the reaction with water vapor.
- A 2-mm perforation has been made in the fuel cladding to facilitate the reaction with water vapor.
- Capped samples are sealed in 316 SS vessels with a quantity of water sufficient water to produce an environment of 100% relative humidity.
- Tests are performed at 175°C in 100% relative humidity.
- Tests have been interrupted at nominal test durations of 30, 60, 150, 210, and 300 days for visual examination, weighing, and diametrical measurements.
- Tests have been ongoing since mid-1998.

A scaled schematic diagram of the capped spent fuel sample and the reaction pressure vessel is given in [Figure A1](#).

INITIAL RESULTS

The following items summarize qualitative observations on the Clad Fuel Vapor Tests to date:

- Visual examination of samples reacted for 300 days show evidence for the formation of secondary alteration products, probably dehydrated schoepite.
- Diametrical measurements indicate no evidence of strain of the cladding.
- There is evidence of a mass gain in each of the reacted samples.

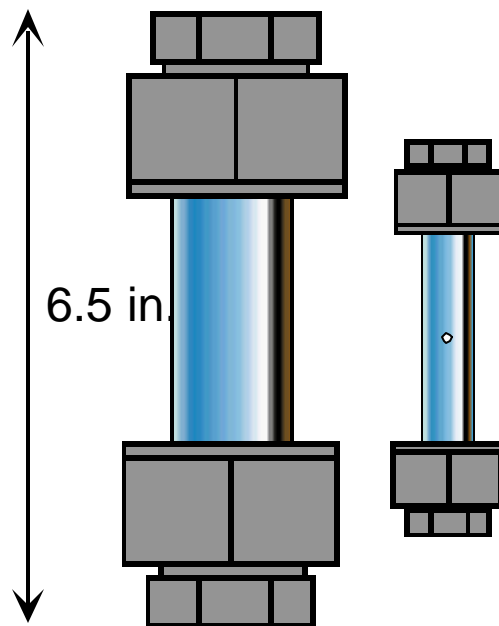


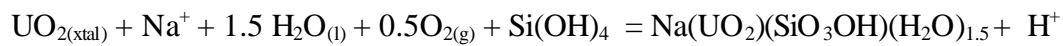
Figure A1. The Capped Spent Fuel Sample and the Reaction Pressure Vessel

ATTACHMENT I, PART B
CLAD FUEL DRIP TESTS

CLAD FUEL DRIP TESTS

A second suite of tests examines the reaction of clad irradiated UO_2 in cladding with periodic injection of Si-rich simulated groundwater at 90°C to investigate the effect of cladding on the dissolution and radionuclide release mechanisms of fuel under hydrologically unsaturated conditions. The tests are being performed at Argonne National Laboratory for the YMP. These tests are designed to explore the experimental factors of fuel segment length, fuel burnup, and reactor type fuel. The tests should elucidate the effect that secondary alteration phases have on the fuel segments hydraulic conductivity and whether the formation of these phases can cause the cladding to unzip.

The chemical reaction relevant to this system is:



See main report Section 4.1.5. This reaction is the oxidative dissolution of crystalline uranium dioxide in the presence of sodium and silica to form sodium boltwoodite. The Gibbs free energy is -124.7 kJ/mol indicating a thermodynamically favorable reaction. As discussed under the vapor tests, reaction can increase the solid volume and possibly cause strain and breach of the cladding.

EXPERIMENTAL

Five tests are being performed on segments from three commercial spent nuclear fuels (see [Table I-B1](#)). Three tests with a nominal 30-GWd/MTU burnup, Zircaloy-4-clad UO_2 PWR fuel, ATM-103, are being run on segments measuring nominally 1.5, 2.5, and 3.5 inches in length. One test is being run on a 1.5-inch segment of a nominal 45-GWd/MTU burnup, Zircaloy-4-clad UO_2 PWR fuel, ATM-106. One test is being run on a nominal 3-inch segment of a nominal 60-GWd/MTU burnup, Zircaloy-2-clad $\text{UO}_2/\text{Gd}_2\text{O}_3$ BWR fuel, ATM-109C. The simulated groundwater EJ-13 is injected onto the fuel segments at a rate of 0.75 mL/3.5 d. Tests are configured so that EJ-13 is injected onto the top of each segment, where it percolates axially through the length of the segment; then it is collected. The test temperature is 90°C .

[Table I-B1. Samples used in clad fuel vapor tests](#)

Specimen Identification	Fuel Type	Clad Segment Length (in.)
S3J2-2	ATM-103	1.461
S3J2-3	ATM-103	2.626
S3J2-4	ATM-103	3.6850
S6J2-2	ATM-106	1.442
S9J2-3	ATM-109C	3.190

The test vessel and drip system is composed of five subsystems: water injection, test vessel, oven, instrumentation and control, and data acquisition. The water injection system (see [Figure](#)

B1) consists of a water supply, pump, 6-way valve, pressure relief valves, overflow reservoir, standpipes or accumulators, and associated tubing and fittings. The water supply is a 250-ml Nalgene bottle, which holds EJ-13 water to be injected. A positive displacement-metering pump is used to pump 0.75 ml of water per injection. A 6-way valve directs the water through to the selected test vessel. The outlet of each leg of the valve is connected to a union cross, which in turn connects to a 0-50 psi pressure transducer; an adjustable pressure relief valve set for 10 psi; a 10-ml standpipe or hydraulic accumulator to minimize the hydraulic pressure increase during water injection; and a SST tube that connects to the test vessel.

The test vessel is made by swaging a modified reducer to each end of the fuel segment. The reducer is milled to receive a stainless steel (SS) frit and is swaged to the fuel using a SS sleeve to make up the difference in diameter between the fuel cladding and the stock fitting. The bottom of the fuel segment is connected to another reducer that is modified with a welded 1/16" piece of SS tubing that provides a vent path through a solenoid controlled valve to ambient pressure. This reducer also brings the diameter up to 1 1/4" to accept a collection vessel made from SS tubing capped and welded at the bottom.

The fuel sample and the associated collection vessel are placed in an oven to maintain the desired test temperature. Two type K thermocouples are mounted in the oven for temperature control, over temperature protection, and data logging. Each test vessel has an associated pressure transducer. Output signals from the transducers and thermocouples are connected to a computer based data acquisition system.

The following items broadly summarize the Clad Fuel Drip Tests after five months of operation:

- Tests are performed at 90°C.
- Simulated groundwater EJ-13 is injected into tests at a rate of 0.75 mL/ 3.5 d with a displacement pump at a low hydraulic pressure.
- Each fuel segment is capped with a Swagelok compression fitting modified with a 100 µm stainless steel frit.
- The pressure at the point of injection is quantitatively monitored in real time. This pressure, however, is not National Institute of Standards and Technology (NIST) traceable.
- Solution is collected in a 316 SS vessel. Tests were sampled after 4 months.
- Tests have been ongoing since March 1999.

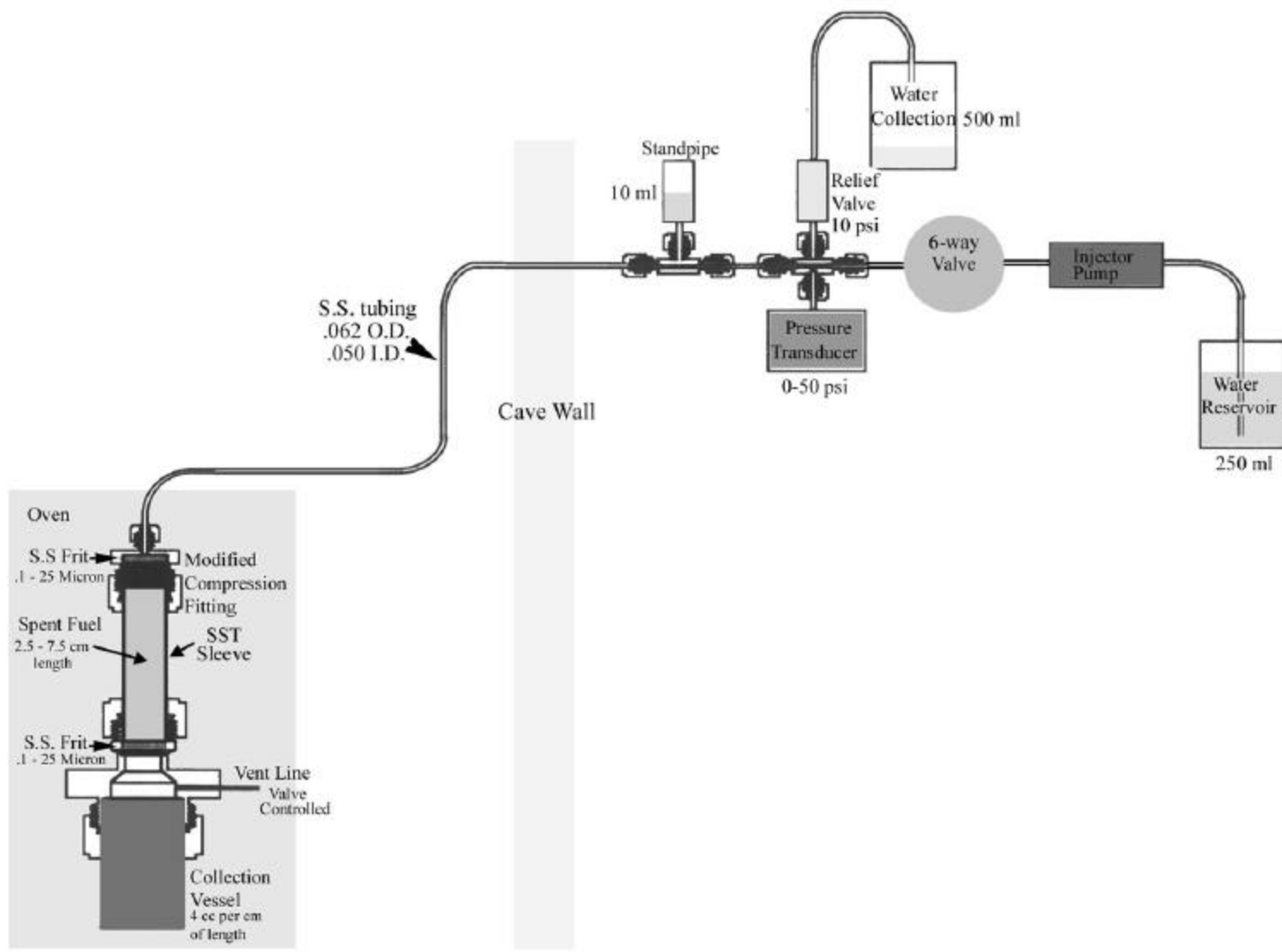


Figure B1. Schematic of Apparatus for Clad Fuel Drip Tests

INITIAL RESULTS

The following items summarize qualitative observations on the Clad Fuel Drip Tests to date:

- EJ-13 simulated groundwater readily flows through all samples.
- The magnitude of the pressure increase at time of injection is proportional to the length of the fuel sample.
- The rate of decrease of the pressure after injection is inversely proportional to the fuel segment length.
- Diametrical measurements indicate no evidence of strain of the cladding.
- Essentially all of the EJ-13 water injected was quantitatively recovered.
- The hydraulic conductivity of the 4-inch segment of ATM-103 (specimen S3J2-4) was observed to decrease after 3 months of reaction.

ATTACHMENT II

DESCRIPTION OF EXCEL WORKBOOKS

ATTACHMENT II

DESCRIPTION OF EXCEL WORKBOOKS

Attachment III contains six Excel workbooks supporting graphs, tables, or numbers in this AMR. Although the workbooks mention various data sources, the body of the report should be referred to for the full literature reference citations, and for equations from the report which are used in the spreadsheets.

The six workbooks and their functions are:

`CrackTipStresses7.xls` (1 sheet): Evaluation of Equations 20 through 23 of the report, to make [Figures 15-18](#) and to find the relative contributions of various stress and strain components to summed quantities. Used in Section 6.7.

`RodAndCladDims9.xls` (3 sheets): Design dimensions in Section 4.1.1 and used later.

`ShapeOfFuelSolid4.xls` (2 sheets): Used to make [Figures 22, 23](#) on an alternate-concept issue at the end of Section 6.7.

`U_DissolRate_Distrib2.xls` (1 sheet): Data on spent fuel dissolution, from Stout and Leider (1998), for extracting distribution parameters and making a plot. Used in Section 4.1.7.

`ZircEandNuPson&Glas9.xls` (2 sheets): Data from Glasstone and Sesonske (1981) for slopes vs. temperature, and data from Pettersson et al. (1979) on Young's modulus for irradiated Zircaloy. Used in Section 4.1.2.

`ZircYieldAndStrain2.xls` (19 sheets): Data from Huang (1995, Table 9.1) and Lowry et al. (1981, Tables 16-24), and plots from the data. Used in Section 4.1.2.

Note that many of the small tables in the body of the AMR show the results of hand calculations with a specified equation, just multiplying or dividing a few numbers.

To verify that the formulas in the workbooks work properly, the results in some cells were checked by hand calculations. The hand calculations agreed with the workbook results. The ranges of cells that were checked are listed in [Table II-1](#). The cells listed there are representative; for example, if “=1 - A18”, worked correctly, it was deemed unnecessary to check “=1 - A19”, “=1 - A20”, etc. For simple assignments (copying values from one cell to another) and simple calls to built-in functions (e.g., =AVERAGE(D5:D7)), checking of the calculations was considered to be unnecessary. Additional verification checks were done by comparisons carried out graphically; see below in this attachment.

More detail on the workbooks, their sheets, and their application in the report follow.

Table II-1. Workbook cells selected for verification.

Excel Cell Reference
'[CrackTipStresses7.xls]CrackTipStresses'!\$D\$13:\$D\$48
'[RodAndCladDims9.xls]RodDimsInclClad'!\$A\$8
'[RodAndCladDims9.xls]Gap Area Ratio'!\$A\$9
'[RodAndCladDims9.xls]Gap Area Ratio'!\$E\$10:\$E\$23
'[RodAndCladDims9.xls]Gap Area Ratio'!\$E\$39
'[RodAndCladDims9.xls]Gap Area Ratio'!\$E\$54:\$E\$65
'[RodAndCladDims9.xls]TimeToFillGap'!\$D\$4
'[RodAndCladDims9.xls]TimeToFillGap'!\$D\$8
'[ShapeOfFuelSolid4.xls]Dehydr.Schoepite'!\$H\$9
'[ShapeOfFuelSolid4.xls]Dehydr.Schoepite'!\$H\$11
'[ShapeOfFuelSolid4.xls]Dehydr.Schoepite'!\$B\$29:\$E\$29
'[ShapeOfFuelSolid4.xls]Dehydr.Schoepite'!\$I\$29:\$J\$29
'[U_DissolRate_Distrib2.xls]U_DissolRate'!\$I\$6
'[U_DissolRate_Distrib2.xls]U_DissolRate'!\$M\$7
'[U_DissolRate_Distrib2.xls]U_DissolRate'!\$C\$20
'[U_DissolRate_Distrib2.xls]U_DissolRate'!\$I\$20
'[U_DissolRate_Distrib2.xls]U_DissolRate'!\$M\$20
'[ZircEandNuPson&Glas9.xls]E irradi, Pettersson'!\$D\$85
'[ZircEandNuPson&Glas9.xls]Glasstone E,nu'!\$C\$11
'[ZircEandNuPson&Glas9.xls]Glasstone E,nu'!\$G\$17
'[ZircYieldAndStrain2.xls]Lowry&H_YldStress'!\$E\$92
'[ZircYieldAndStrain2.xls]Lowry&H_YldStress'!\$E\$98:\$E\$99

Workbook CrackTipStresses7

Sheet CrackTipStresses- This sheet calculates values, versus angle, for the relative radial dependence of components of stress, strain, and of the yield-stress threshold quantity, using Equations 20 through 23 of the report.

The calculated values are used to make [Figures 15, 16, 17, 18](#) of the report and to determine approximately the relative contributions of different components at the single angle 110 degrees.

The calculation is verified by graphically comparing the angular variation of the shear strain as calculated by two methods. In the first method, the shear stress is calculated in making [Figures 15 and 16](#), and the shear strain is directly proportional to the shear stress (Equation 24). In the second method, the partial derivatives of displacement u are calculated in making [Figures 17 and 18](#), and the shear strain is related to these derivatives by Equation 20. A plot of the angular distribution of shear strain by these two methods is shown in [Figure II-1](#) for the case of plane

stress. The results of the two methods agree exactly. Results of the two methods for the case of plane strain agree with each other exactly as well.

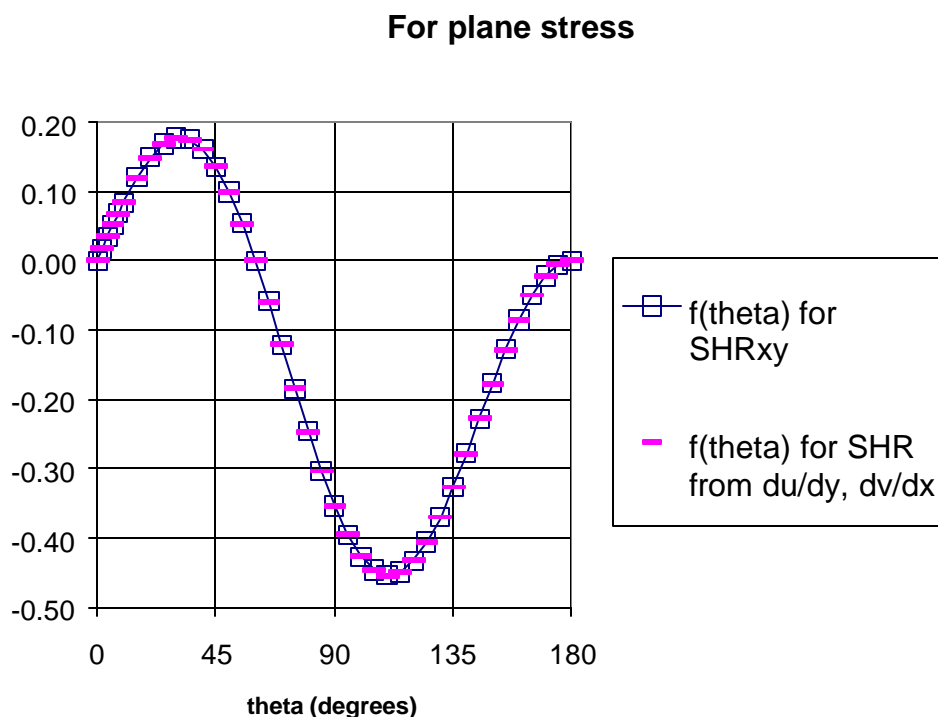


Figure II-1. Excerpt from sheet *CrackTipStresses*. Plot of the angular dependence of the shear strain calculated by two different methods, for the plane stress case.

Workbook **RodAndCladDims9**

Sheet RodDimsInclClad—Data taken from Stout and Leider (1998, Section 2.1.2), from specific tables as noted in the spreadsheet table. This data is just sufficient to make [Table 1](#) of the report.

Sheet RodAndClad_DimsMore—Contains two additional data elements from the noted WFCR tables (these additional data are not actually used). Calculates further parameters: (1) Gap Area/Fuel Area, and (2) Clad I.R./Clad Thickness. These are recalculated in the next sheet and so are not used from this sheet.

Sheet Gap Area Ratio—Calculates further parameters for each of the fuel designs: (1) Gap Area/Fuel Area, used in Section 6.6, [Table 9](#); (2) Clad Thickness/Clad I.R.; (3) Clad Thickness/Clad I.D., used in Section 6.5, following Equation 10; and (4) (Clad mid-radius × Thickness)/Thickness-squared, used in Section 6.4, following Equation 8. Also calculates average values of some parameters.

Sheet TimeToFillGap—Takes average diametral gap (inches) from preceding sheet "Gap Area Ratio", calculates average radial gap (micrometers) = G (Section 6.6, used in Equation 14). Calculates values for Section 6.6 [Table 11](#), using Equation 14.

NOTE: [Tables 10 and 12 to 15](#) show the results of hand calculations using a single equation each.

Workbook ShapeOfFuelSolid4

Sheet Dehydr.Schoepite—This sheet calculates arrays, using Equation 34 of the Report, and input values from the report for $v_2/(S \cdot D)$ (which ratio is independent of S and D , see report), D for dehydrated schoepite, and a nominal $R_0=1$, to produce [Figures 22 and 23](#) of the Report.

Sheet Metaschoepite—This sheet calculates arrays similarly, except using D for metaschoepite. This is done to be able to compare the shapes produced by the plots, for dehydrated schoepite versus metaschoepite. Only the graphs from the first sheet, for dehydrated schoepite, are used in the report.

Workbook U_DissolRate_Distrib2

Sheet, U_DissolRate—Has the experimental data set on spent-fuel dissolution rates, for burnups of 30 MW-days/MTU and above, taken from Stout and Leider (1998, Tables 2.1.3.5-4 and 2.1.3.5-4a). Converts units, sorts by dissolution-rate values, and makes a plot with a logarithmic scale; this is [Figure 12](#).

Workbook ZircEandNuPson&Glas9

Sheet E irradi, Pettersson—Reproduces [Tables 2 and 3](#) from Pettersson et al. (1979). Calculates mean, variance, standard deviation of the set of data at 1%-per-hour strain rate, and variance and standard deviation of the calculated mean (stated in report text, Section 4.1.2.2). To be used in a plot in the next worksheet.

Sheet Glasstone E,nu—Reproduces selected data from Table A.6 of Glasstone and Sesonske (1991). A subset of this literature table (using columns for Young's modulus and Poisson's ratio) is reproduced in the report as [Table 2](#). This table data, together with the mean and the standard deviation of the mean of Pettersson's 1%/hour strain rate data (sheet **E irradi, Pettersson**), are used to make [Figure 8](#).

Workbook ZircYieldAndStrain2.xls

Sheet Mat.Beh.—Reproduces part of a table from Huang (1995, Table 9.1, the part on p. 158). Note that one line of data is omitted because of an apparent internal inconsistency, i.e., yield stress is less than ultimate stress. Possibly a typographical data-entry error in the book; that data line has just been omitted.

Sheet Tensile Test Results—Reproduces part of a table from Huang (1995, Table 9.1, the part on p. 157).

Data values in the spreadsheet were visually compared to the original paper sheets from the references. In the ten tables as keyed in, only three numbers were found with data entry errors; these were corrected, and a border was placed on the spreadsheet cell as a visual pointer to the corrected data. An example showing two of the corrections is shown in [Table II-2](#). Input data were further checked by a detailed plot; see `Sheet HuangTensileDetail` below.

Table II-2. Excerpt from `sheet Tensile Test Results`. The numerical cells above with a black border are ones where an input data error has been corrected.

Huang Table 9.1 part 1
(Page 157)

Tube	T	Fluence	str-yld	str-ult	Red. in area	e-uniform	e-total
2954	32	0.0	431.6	587.4	35.9	7.6	17.9
2954	177	0.0	331.6	446.7	39.7	5.9	12.8
2954	288	0.0	318.5	368.1	38.3	3.5	9.6
2954	32	0.7	716.3	735.6	24.1	2.2	6.9
2954	32	5.6	810.7	890.7	27.7	3.2	6.9
2954	177	5.6	716.3	758.3	16.3	2.4	4.9
2954	288	5.6	637.0	681.1	22.9	2.5	5.8
2954H	32	5.6	868.6	934.8	23.2	3.5	8.9
2954H	177	5.6	736.3	770.1	21.2	2.3	6.1
2954H	288	5.6	650.1	672.9	23.6	2.3	5.6
2755	32	0.0	526.7	649.4	40.1	7.8	18.6
2755	288	0.0	341.3	402.6	49.6	3.6	11.0
2755	32	2.2	818.3	836.2	29.5	1.5	6.4
2755	177	2.2	688.0	690.8	31.1	0.6	5.6
2755	288	2.2	590.1	590.1	32.4	0.3	4.4
2755	32	4.9	823.8	876.9	23.3	2.9	7.1
2755	177	4.9	724.6	738.3	27.1	2.2	5.3
2755	288	4.9	630.1	637.7	30.9	1.6	4.8

Sheet Huang Tensile Tests—This sheet combines the data from the first two sheets; sorted first into zero fluence and non-zero fluence, then by temperature. It also contains some plots not used in the report.

Sheet Huang Tensile Tests2—Reproduces Huang’s data (1995, Table 9.1) at a strain rate of 0.005/min. Thus the values for specimen #2954H (one at each of three temperatures) are not included here. This data set is used to form the average values at each temperature for unirradiated and irradiated Zircaloy specimens, for later use. [Figure 1](#) and [Figure 2](#) are made in this sheet.

Sheet HuangTensileDetail—Graphical examination of some details in the Huang data set (1995, Table 9.1), e.g., the slopes for different samples. Used for input data checking, but not used in the report. The data placement in the graph (Figure II-2) is checked visually for consistency. The main consistency is that the slopes are fairly consistent for values at each temperature taken from the same sample of material at a given neutron fluence. Each sample can show a consistent variation from the other samples.

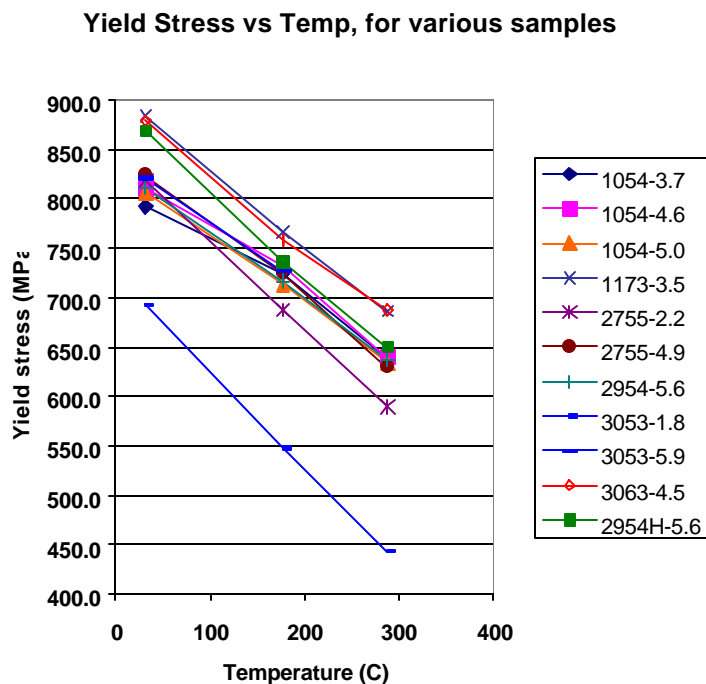


Figure II-2. Excerpt from sheet HuangTensileDetail. Graph of yield stress as a function of temperature, for individual samples tested at several temperatures (Huang 1995).

Sheet Unirradiated Sandvik—Reproduces Table 16 from Lowry et al. (1981).

Sheet Unirradiated Ocone—Reproduces Table 17 from Lowry et al. (1981).

Sheet Irradiated HBR 0.025—Reproduces Table 18 from Lowry et al. (1981).

Sheet Irradiated HBR 371—Reproduces Table 19 from Lowry et al. (1981).

Sheet Irradiated HBR 482—Reproduces Table 20 from Lowry et al. (1981).

Sheet Irradiated Ocone I .025—Reproduces Table 21 from Lowry et al. (1981).

Sheet Irradiated Ocone I 371—Reproduces Table 22 from Lowry et al. (1981).

Sheet Irradiated Ocone I 2 cycle—Reproduces Table 23 from Lowry et al. (1981).

Sheet Irradiated Ocone 1 3 cycle—Reproduces Table 24 from Lowry et al. (1981).

Sheet LowryFourIrradSets—Uses data of preceding sheets from Tables 18, 21, 23, 24 of Lowry et al. (1981). Some plots from that data; not used in report.

Sheet Lowry&H_YldStress—Uses data of preceding sheets from Tables 18, 21, 23, 24 (irradiated), 16, 17 (unirradiated) of Lowry et al. (1981), plus averages from sheet Huang Tensile Tests2. This data is used to make Figure 3.

This sheet also makes several plots which are blow-ups of part of Figure 3's range. These plots are used as an aid in Section 4.1.2.5, "Yield stress correlation", as described in the text. These plots are not presented in the report, since Figure 3 shows the same data. Interpolations calculated in this sheet and used in Sections 4.1.2.5-4.1.2.6 are verified by a plot; see Figure II-3.

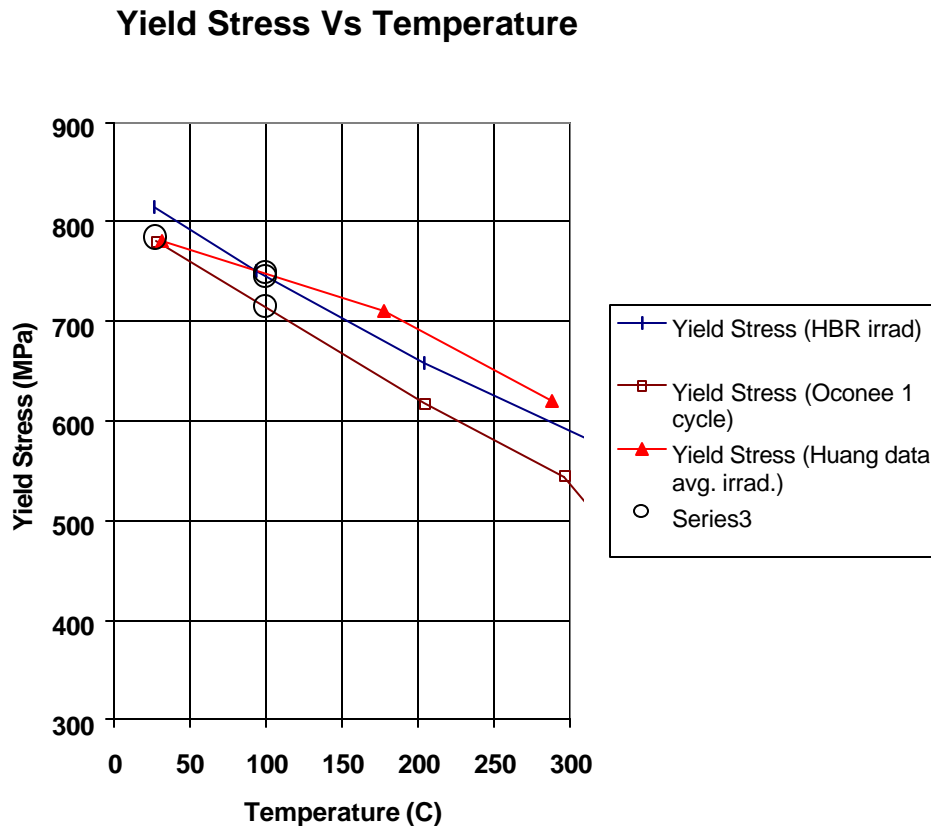


Figure II-3. Excerpt from sheet Lowry&H_YldStress. Curves from Lowry and from Huang data containing data below 200°C, for irradiated Zircaloy. The larger circles are values interpolated on one or another of the individual curves shown.

Sheet Lowry&H_UnifStrain—Uses data of preceding sheets from Tables 18, 21, 23, 24 (irradiated) of Lowry et al. (1981), plus averages from sheet Huang Tensile Tests2. This data is used to make Figure 6.

Sheet Lowry&H_TotalStrain—Uses data of preceding sheets from Tables 18, 21, 23, 24 (irradiated) of Lowry et al. (1981), and plus averages from sheet Huang Tensile Tests2. This data is used to make [Figure 7](#).

Sheet LowryVsStrainRate—Using data copied from preceding sheets from Tables 17, 19, (Table 20 copied but not used in plots), 22, 23, 24 of Lowry et al. (1981); and Huang data (1995, Table 9.1) for specimen #2954 samples at two strain rates and three temperatures (Huang data plot not used in report). The Lowry data are used to make [Figures 4 and 5](#).

NOTE: [Table 3](#) shows data elements copied from Lowry's report (Lowry et al. 1981) at pages noted. [Table 3](#) is not from a spreadsheet.